Applied Computational Electromagnetics Society

Journal

November 2012 Vol. 27 No. 11

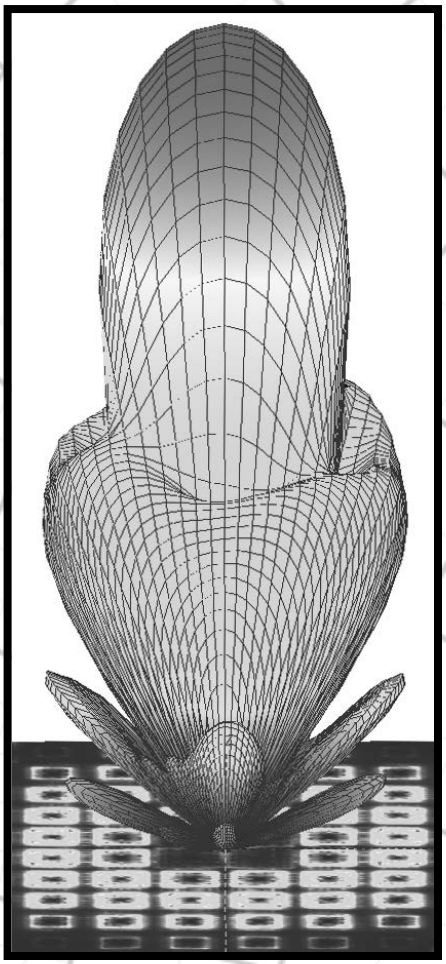

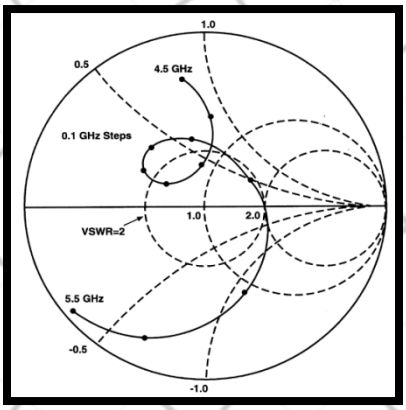

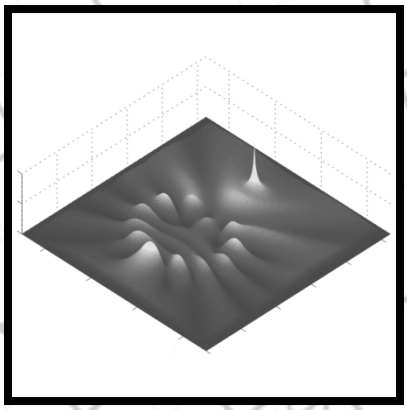

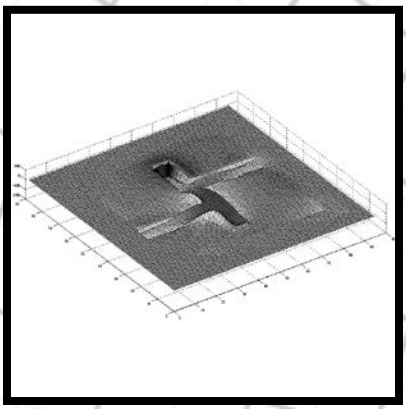

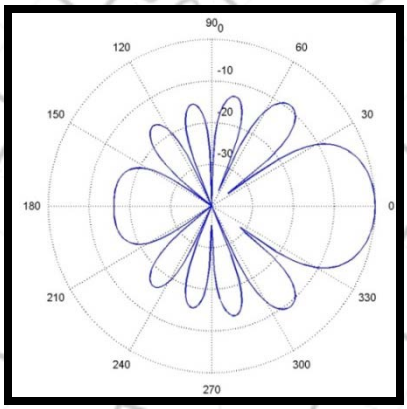

ISSN 1054-4887

GENERAL PURPOSE AND SCOPE: The Applied Computational Electromagnetics Society ***(ACES)*** Journal hereinafter known as the ***ACES Journal*** is devoted to the exchange of information in computational electromagnetics, to the advancement of the state-of-the art, and the promotion of related technical activities. The primary objective of the information exchange is to inform the scientific community on the developments of new computational electromagnetics tools and their use in electrical engineering, physics, or related areas. The technical activities promoted by this publication include code validation, performance analysis, and input/output standardization; code or technique optimization and error minimization; innovations in solution technique or in data input/output; identification of new applications for electromagnetics modeling codes and techniques; integration of computational electromagnetics techniques with new computer architectures; and correlation of computational parameters with physical mechanisms.

SUBMISSIONS: The ***ACES Journal*** welcomes original, previously unpublished papers, relating to applied computational electromagnetics. Typical papers will represent the computational electromagnetics aspects of research in electrical engineering, physics, or related disciplines. However, papers which represent research in applied computational electromagnetics itself are equally acceptable.

Manuscripts are to be submitted through the upload system of ***ACES*** web site http://aces.ee.olemiss.edu See "Information for Authors" on inside of back cover and at ***ACES*** web site. For additional information contact the Editor-in-Chief:

Dr. Atef Elsherbeni
Department of Electrical Engineering
The University of Mississippi
University, MS 386377 USA
Phone: 662-915-5382
Email: atef@olemiss.edu

SUBSCRIPTIONS: All members of the Applied Computational Electromagnetics Society are entitled to access and download the ***ACES Journal*** any published journal article available at http://aces.ee.olemiss.edu. Printed issues of the ***ACES Journal*** are delivered to institutional members. Each author of published papers receives a printed issue of the ***ACES Journal*** in which the paper is published.

Back issues, when available, are $50 each. Subscription to ***ACES*** is through the web site. Orders for back issues of the ***ACES Journal*** and change of address requests should be sent directly to ***ACES*** office at:

Department of Electrical Engineering
The University of Mississippi
University, MS 386377 USA
Phone: 662-915-7231
Email: aglisson@olemiss.edu

Allow four weeks advance notice for change of address. Claims for missing issues will not be honored because of insufficient notice, or address change, or loss in the mail unless the ***ACES*** office is notified within 60 days for USA and Canadian subscribers, or 90 days for subscribers in other countries, from the last day of the month of publication. For information regarding reprints of individual papers or other materials, see "Information for Authors".

LIABILITY. Neither ***ACES***, nor the ***ACES Journal*** editors, are responsible for any consequence of misinformation or claims, express or implied, in any published material in an ***ACES Journal*** issue. This also applies to advertising, for which only camera-ready copies are accepted. Authors are responsible for information contained in their papers. If any material submitted for publication includes material which has already been published elsewhere, it is the author's responsibility to obtain written permission to reproduce such material.

APPLIED COMPUTATIONAL ELECTROMAGNETICS SOCIETY JOURNAL

November 2012
Vol. 27 No. 11
ISSN 1054-4887

The ACES Journal is abstracted in INSPEC, in Engineering Index, DTIC, Science Citation Index Expanded, the Research Alert, and to Current Contents/Engineering, Computing & Technology.

The illustrations on the front cover have been obtained from the research groups at the Department of Electrical Engineering, The University of Mississippi.

NOVEMBER 2012 REVIEWERS

Ahmed Abdelrahman
Marco Arjona
Kabir Ashraf
Hany Atallah
Mohamed Bakr
Ru-shan Chen
Ozgur Ergul
Josefa Gomez
He Huang
Nathan Ida
Haider Khaleel
Mengmeng Li
Guangdong Pan
Andrew Peterson
Colan Ryan
Behrooz Rezaeealam
Binay Sarkar
Nikolaos Tsitsas
Yasuhiro Tsunemitsu
Xiaobo Wang
Xiaoling Yang
Ozan Yurduseven
Yujuan Zhao
Shouzheng Zhu

THE APPLIED COMPUTATIONAL ELECTROMAGNETICS SOCIETY

JOURNAL

Vol. 27 No. 11 November 2012

TABLE OF CONTENTS

Analytical and FEM Based Calculation of Electromagnetic Forces Exerted on Cylindrical Coils due to their own Current

Abbas Shiri[1] and Davood Esmaeil Moghadam[2]

[1]Department of Electrical Engineering
Hadishahr Branch, Islamic Azad University, Hadishahr, Iran
abbas_shiri@iust.ac.ir

[2] Department of Electrical Engineering
High Voltage Institute, Technical University of Dresden, Dresden, 01072, Germany
moghadam@ieeh.et.tu-dresden.de

Abstract ─ Different parts of the cylindrical coils are exposed to electromagnetic forces due to electric current flowing through it. These forces can deform the coil in axial and radial directions in abnormal operating conditions. So, in design process of cylindrical coils in many magnetic devices, mechanical stresses exerted on different parts of these kinds of coils should be determined. In this paper, analytical expressions for the forces in axial direction are derived in order to calculate the forces exerted on different parts of the cylindrical coils. In order to evaluate the precision of the method, the finite element method (FEM) is used and the results obtained by FEM are compared with the results of the analytical equations. Results obtained by finite element analysis confirm the analytical method. Due to inherent difficulties in calculation of the forces in radial direction, distribution of the latter on the coil body is calculated by FEM. The results show that the outer turns of the coil in two axial ends are exposed to the largest axial tension, while radial stresses are largest in the middle parts of the coil. In this paper, the calculations focus on the cylindrical coils; however, the method can be used for the calculation of the magnetic force distribution on different parts of spiral coils, disc coils and any type of air-cored coils with different sizes.

Index Terms ─ Analytical method, cylindrical coil, electromagnetic force distribution, FEM.

I. INTRODUCTION

Due to the extensive application of cylindrical coils in industry such as linear tubular motors, magnetic launchers and casting industries [1-3], determining the distribution of the mechanical stresses on different parts of the former is necessary. The calculation of the magnetic force distribution on current-carrying coils is closely related to the calculation of the magnetic force between them. To calculate the force between these coils, a variety of methods have been proposed in literature. There are some empirical equations and tables to calculate the force between coils with different shapes [4]. Also, the variation of the mutual inductance between two coils is used to calculate the force between them. In the latter method, first the mutual inductance between two coils is calculated and then it is used to calculate the force [5-7]. There are many articles which discuss the calculation of the magnetic forces between magnetic coils. In references [8-10], magnetic force between spiral coils is calculated using a new and effective method. In other research, magnetic forces between cylindrical coils are calculated [11, 12]. In this paper, using the method developed in [10], the axial magnetic force distribution on different parts of the cylindrical coils is calculated. The results are validated using finite element method (FEM). Also, FEM is employed to calculate the distribution of the radial forces on the cylindrical coils.

Submitted On: Dec. 31, 2011
Accepted On: Sept. 16, 2012

II. MAGNETIC FORCE BETWEEN TWO CONCENTRIC CIRCULAR ELEMENTS

Suppose a system of two current carrying rings as shown in Fig. 1. To calculate the force between them, the concept of vector magnetic potential is employed. The vector magnetic potential of ring 1 in any point P on ring 2 is equal to [13]:

$$\vec{A} = \frac{\mu_0 I_1}{4\pi} \oint_{C_1} \frac{d\vec{l}'}{R_1}, \tag{1}$$

where μ_0 is the vacuum permeability, I_1 is the current of ring 1, C_1 is the length of ring 1 and R_1 is the distance between the differential component of the source $d\vec{l}'$ at point p′ and the field point p (Fig. 2).

By obtaining the vector magnetic potential, the flux density is calculated using the following equation [13]:

$$\vec{B} = \vec{\nabla} \times \vec{A}. \tag{2}$$

To calculate the force of ring 1 exerted on ring 2, the following equation is employed [13]:

$$\vec{F}_{21} = I_2 \oint_{C_2} d\vec{l}_2 \times \vec{B}, \tag{3}$$

where I_2 is the current of ring 2. Using equations (1) and (2) in equation (3) and doing some mathematical calculations, the following equation for the force is obtained:

$$\vec{F}_{21} = \vec{a}_z \left(\frac{\mu_0 I_1 I_2 zk}{2\sqrt{ab}(1-k^2)}\right)[(1-k^2)K(k) - (1-(1/2)k^2)E(k)]. \tag{4}$$

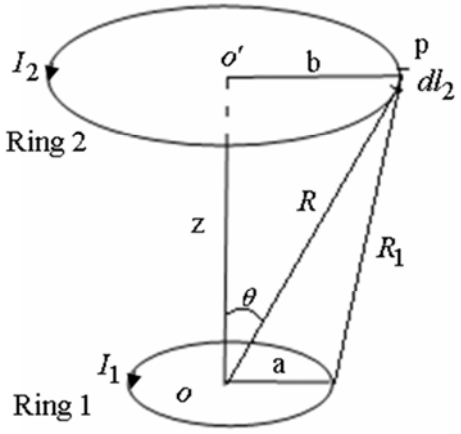

Fig. 1. Two current carrying concentric rings in z distance of each other.

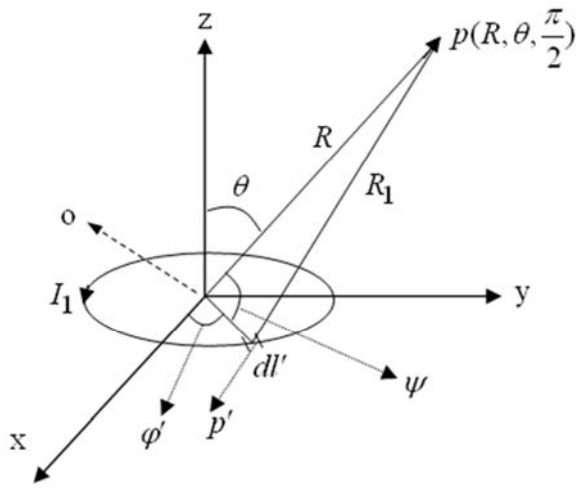

Fig. 2. Determination of the vector potential of a current carrying ring with radius a in any given point p.

In the aforementioned equation, a and b are radii of rings 1 and 2, respectively, z is axial distance of the two rings and k ($0 < k < 1$) is a constant coefficient and is equal to:

$$k = \sqrt{\frac{4ab}{(a+b)^2 + z^2}}, \tag{5}$$

and *K(k)* and *E(k)* are first and second order elliptic integrals respectively, which are defined as:

$$K(k) = \int_0^{\frac{\pi}{2}} \frac{d\theta}{(1-k^2 \sin^2\theta)^{1/2}}. \tag{6}$$

$$E(k) = \int_0^{\frac{\pi}{2}} (1-k^2 \sin^2\theta)^{1/2}\, d\theta. \tag{7}$$

III. CALCULATION OF AXIAL DISTRIBUTION OF THE FORCE

In order to calculate the mechanical stresses exerted on different parts of the coil resulting from its current, the mesh-matrix method is employed. Consider *a* coil with the turn number of *N* shown in Fig. 3, where r_0 is the inner radius, *b* is the radial thickness and *a* is the height of the coil. As seen in this figure, the cross-section of the coil is divided into several segments. Here, the coil is divided into $n_r \times n_a$ cells. To calculate the distribution of the force on the different parts of the coil, the force between different filaments (in Fig. 3, each filament is specified with two cells in

both sides) of the coil is calculated and then added together.

The force between filaments j and l is calculated using equation (4) as follows:

$$f_{jl} = \bar{a}_z\left(\frac{\mu_0 i^2 z_{jl} k'}{2\sqrt{r_j r_l}(1-k'^2)}\right)[(1-k'^2)K(k') - (1-(1/2)k'^2)E(k')]. \quad (8)$$

In the above equation, r_j and r_l are the radii of the filaments j and l, respectively, and z_{jl} is the center to center distance of the two filaments. The current of each filament is supposed to be concentrated on its center, and the current density of the entire coil is supposed to be uniform, and i which can be calculated using the following equation, is the current of each filament in the coil:

$$i = \frac{NI}{n_r \times n_a}. \quad (9)$$

In the above equation, I is the current of the coil. Parameter k' in equation (8) is a constant and is equal to:

$$k' = \sqrt{\frac{4 r_j r_l}{(r_j + r_l)^2 + z_{jl}^2}}. \quad (10)$$

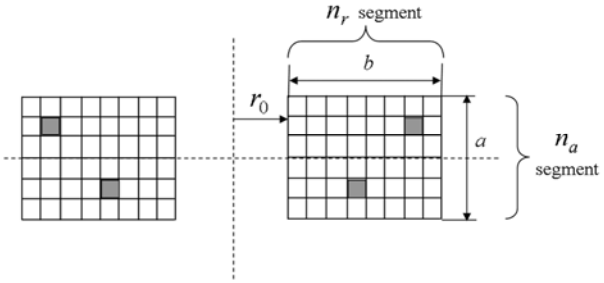

Fig. 3. Division of the coil into different meshes to calculate the force distribution.

IV. RESULTS

A. Analytical results

As mentioned before, the force between two filaments can be calculated using equation (8). In order to calculate the force exerted on specific part of the coil, one can use the effect of all filaments on that part and sum them up. The characteristics of the coil used for calculations are shown in Table 1. The cross-section of the coil has been divided into 71×35 segments, and the current of the coil is supposed to be 12 Amperes. Axially net magnetic force exerted on different parts of the coil is calculated. The force distribution on the outer part (turns located in outer part) of the coil in axial direction is illustrated in Fig. 4a. As seen in this figure, the magnitude of the force is symmetrical in respect to axial axis of the coil in such a way that there is no stress on the middle part of the coil. This is so because, the forces from both sides exerted on the middle part of the coil are equal in magnitude and opposite in direction and so cancel each other out. Figure 4b shows the distribution of the axial force on radial direction. According to this figure, moving across radial direction, the axial force exerted on related parts increases and after reaching a maximum value, it starts to decrease at the outer parts. In order to compare the force distribution on all parts of the coil body, the force profile among the axial and radial dimensions of the coil is illustrated in Fig. 5. It is clear from this figure that the outer parts of the coil at two axial axis ends are the most critical portions, because they are exposed to the largest tension. For instance, a force of about 0.6 N is exerted on the outer parts of the coil located at about 9.5cm in axial axis while the current following the coil is 12 amperes. The current can increase in fault conditions and give rise to deformation of the outer parts of the coil at two axial axis ends.

Table 1: Characteristics of the coil used in calculations

Number of Turns	Inner radius, r_0 (cm)	Radial thickness, b (cm)	Height, a (cm)
2450	5	6	12

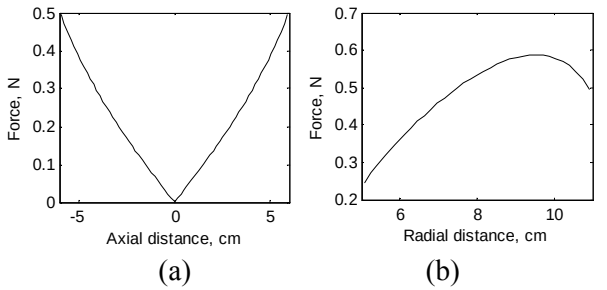

(a) (b)

Fig. 4. (a) Axial force distribution on the outer part of the coil in axial direction. (b) Axial force distribution on lower part of the coil in radial direction.

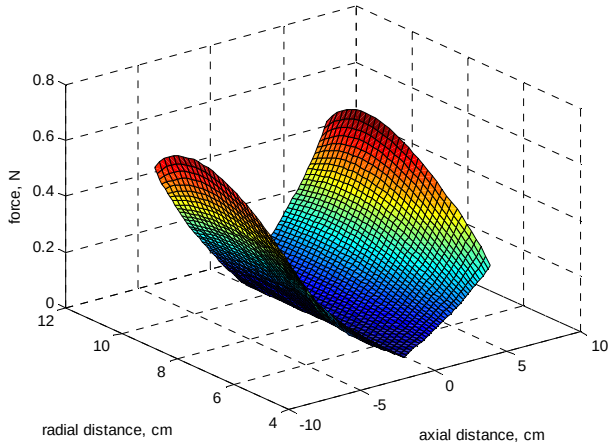

Fig. 5. The force distribution on all parts of the coil body.

B. FEM results

In order to evaluate the precision of the analytical method, in this section, a cylindrical coil is simulated using 2-D finite element method (FEM). The distribution of the flux density produced by the coil is illustrated in Fig. 6. Axial magnetic forces exerted on different parts of the coil due to current flowing through it, as well as radial forces are calculated using FEM. It should be mentioned that due to structure of the coil and inherent difficulties in calculations, only magnetic forces in axial direction is calculated using analytical method. Figure 7 illustrates the axial magnetic force distribution on different parts of the coil. It is clear from this figure that the force exerted on the outer parts of the axial end is the largest in comparison with other parts. In Fig. 7, half of the coil (lower half) is illustrated in order to clearly show the distribution of the force. Starting from the center of the coil, the axial force increases until it reaches the maximum value in axial end of the coil. In radial direction the axial forces increases and then reaches a maximum point and then decreases. So, the results of the Fig. 7 are in good agreement with those presented in Figs. 4 and 5.

The magnetic force is exerted on the coil body in radial and axial directions. In order to calculate the total force on different parts of the coil, the forces in two directions are summed up. Total force distribution on the coil body is illustrated in Fig. 8. As it is seen in this figure, the central parts of the coil are exposed to the largest force. This phenomenon is because of the exertion of the radial forces in these parts. It has been shown before that the axial force exerted on the middle parts of the coil from other parts cancel each other out; however, the radial forces exerted on the middle parts, arising from different parts of the coil are added to each other. Therefore, the middle parts experience largest radial force. Although the radial forces want to decompose the coil, their net effect on different parts is zero. For further clarity a part of the coil in Fig. 8 is magnified in Fig. 9.

The calculation of the distribution of the axial force on different parts of coil has been done using analytical method. The results are compared with FEM results. The coil has 1065 turns which is composed of 15 layers, each layer having 71 turns. The results are given in Table 2. Other specifications of the coil are given in Table 3. In Table 2, axial force distribution on the outer part of the coil in axial direction and on the lower part of the coil in radial direction is presented. In this table, distribution of the axial force is obtained by two methods in both axial and radial directions. As it is seen, the results obtained by FEM are in good accordance with analytical results confirming the proposed method. For better comparison, the results are plotted in Figs. 10 and 11. As the virtual work method gives accurate results in force calculations [14, 15], in this paper, the forces in FEM results are calculated by the former.

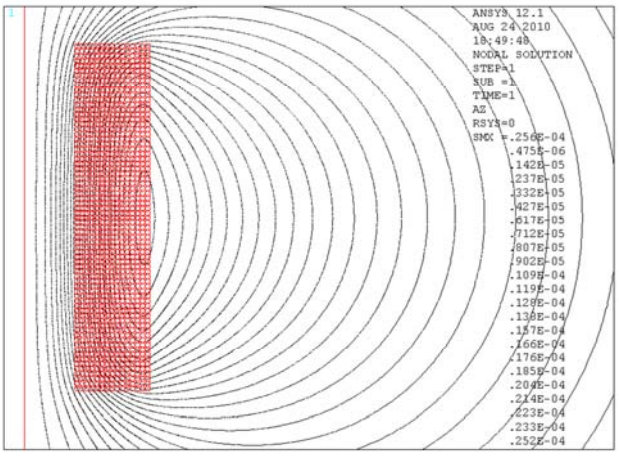

Fig. 6. Flux density distribution for the cylindrical coil.

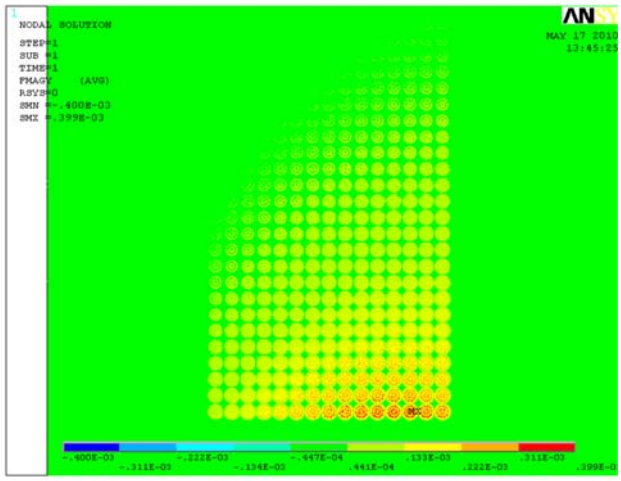

Fig. 7. Axial force distribution on different parts of the cylindrical coil.

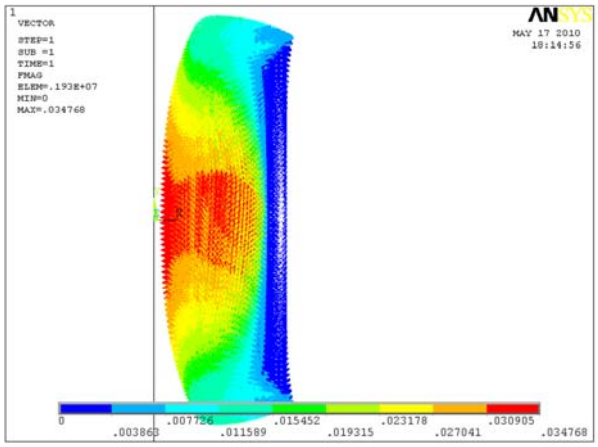

Fig. 8. Total force distribution on the coil's body.

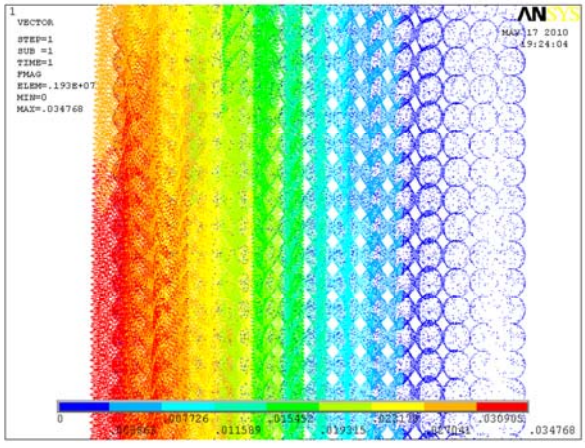

Fig. 9. A part of the coil in Fig. 8.

Table 2: comparison of the axial force distribution on coil's body by analytical method and FEM

	Distance(cm)	Force(N)	
		Analytical	FEM
radial direction	5.08	0.4904	0.5066
	5.40	0.5888	0.5911
	5.56	0.6265	0.6114
	5.88	0.6863	0.6837
	6.04	0.7090	0.7142
	6.52	0.7471	0.7511
	6.68	0.7484	0.7518
	7.00	0.7280	0.7306
	7.16	0.7019	0.6917
	7.32	0.6587	0.6500
axial direction	5.60	0.6587	0.6820
	5.12	0.5382	0.5380
	4.16	0.3730	0.3773
	3.36	0.2724	0.2574
	2.56	0.1923	0.1848
	1.92	0.1379	0.1450
	0.80	0.0548	0.0570
	0.16	0.0109	0.0121
	0	0	0
	-0.48	0.0327	0.0316
	-1.76	0.1252	0.1231
	-2.56	0.1923	0.1976
	-3.52	0.2906	0.3297
	-4.16	0.3730	0.3806
	-4.64	0.4479	0.4318
	-5.28	0.5732	0.6028
	-5.60	0.6587	0.6724

Table 3: Characteristics of the coil used in calculations of the analytical method and FEM

Number of Turns	1065
Inner radius, r_0 (cm)	5
Radial thickness, b (cm)	2.4
Height, a (cm)	11.36
Current of the coil (A)	20
Diameter of the wire used (mm)	1.6

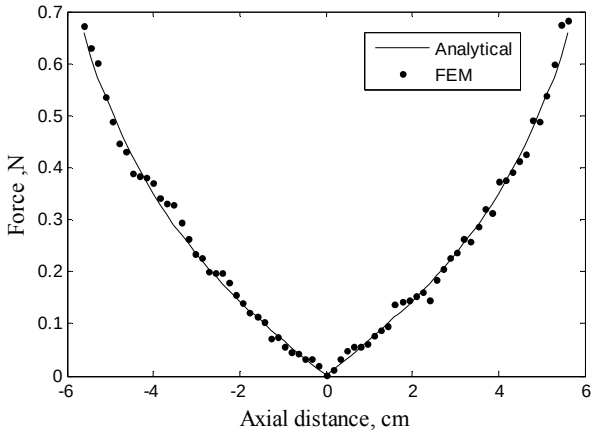

Fig. 10. Axial force distribution on the outer part of the coil in axial direction.

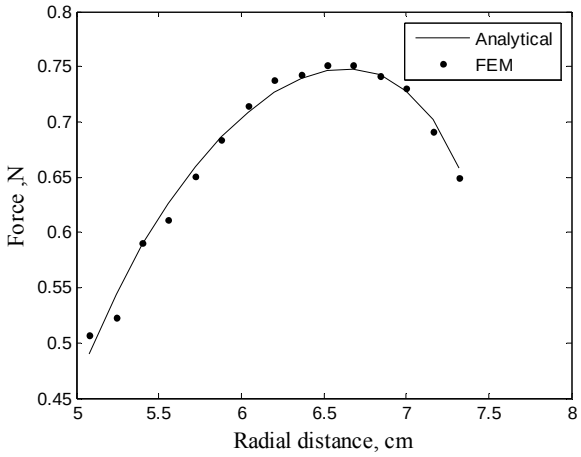

Fig. 11. Axial force distribution on lower part of the coil in radial direction.

V. CONCLUSION

In this paper, the axial and radial electromagnetic force distribution on cylindrical coil's body is calculated. Exact analytical equations are used to calculate the axial forces. According to the results obtained by MATLAB coding, the maximum axial stress is exerted on the outer parts of the coil at two axial axis ends. Thus, it is necessary to sufficiently support those parts of the coil in any application. On the other hand, considering the fact that the forces from both sides exerted on the middle parts of the coil cancel each other out, these parts of the coil are exposed to low tension. In order to verify the results of the analytical method, finite element method is employed. The results are confirmed the accuracy of the analytical method. Calculation of the forces in radial direction is also carried out by FEM. The results show that radial stresses are largest in the middle parts of the coil.

REFERENCES

[1] K. Fujisaki, "Magnetohydrodynamic Stability in Pulse Electromagnetic Casting", *IEEE Trans. Ind. Appl.*, vol. 39, no. 5, pp. 1442-1447, 2003.

[2] A. Meriched, M. Feliachi, and H. Mohellebi, "Electromagnetic Forming of Thin Metal Sheets", *IEEE Trans. Magn.*, vol. 36, no. 4, pp. 1808-1811, 2000.

[3] T. G. Engel, D. Surls, and W. C. Nunnally, "Prediction and Verification of Electromagnetic Forces in Helical Coil Launchers", *IEEE Trans. Magn.*, vol. 39, no. 1, pp. 112-115, 2003.

[4] F. W. Grover, *Inductance Calculations, Working Formulas and Tables*, Dover Publications, New York, 1962.

[5] S. Babic, C. Akyel, and. S. J Salon, "New Procedures for Calculating the Mutual Inductance of the System: Filamentary Circular Coil-Massive Circular Solenoid", *IEEE Trans. Magn.*, vol. 39, no. 3, pp. 1131-1134, 2003.

[6] K. B. Kim, E. Levi, Z. Zabar, and L. Birenbaum, "Mutual Inductance of Noncoaxial Circular Coils with Constant Current Density", *IEEE Trans. Magn.*, vol. 33, no. 5, pp. 4303-4309, 1997.

[7] C. Akyel, S. Babic, and S. Kinicic, "New and Fast Procedures for Calculating the Mutual Inductance of Coaxial Circular Coils (Circular Coil - Disk Coil)", *IEEE Trans. Magn.*, vol. 38, no. 5, pp. 2367-2369, 2002.

[8] A. Shiri, *Calculation of Magnetic Forces Between Current Carrying Coils in Two Plates*, M.Sc. Thesis, Iran University of Science &Technology, September 2006 (in Persian).

[9] A. Shiri and A. Shoulaie, "Calculation of Magnetic Forces Between Spiral Coils Using Mesh Approach", *24th International Power System Conference*, Tehran, Iran, November 2009 (in Persian).

[10] A. Shiri and A. Shoulaie, "A New Methodology for Magnetic Force Calculations Between Planar Spiral Coils", *Progress in Electromagnetics Research*, PIER 95, pp. 39-57, 2009.

[11] A. Shiri and A. Shoulaie, "New Results in Calculation of Magnetic Forces Between Cylindrical Coils", *23nd International Power System Conference*, Tehran, Iran, November 2008 (in Persian).

[12] A. Shiri, M. R. A. Pahlavani, and A. Shoulaie, "A New and Fast Procedure for Calculation of the Magnetic Forces Between Cylindrical Coils", *International Review of Electrical Engineering*, vol. 4, no. 5, pp. 1053-1060, 2009.

[13] D. K. Cheng, *Field and Wave Electromagnetics*, Second Edition, Prentice Hall, 1989.
[14] J. Mizia, K. Adamiak, A. R Eastham, and G. E. Dowson, "Finite Element Force Calculation: Comparison of Methods for Electric Machines", *IEEE Trans. Magn.*, vol. 24, no. 1, pp. 447-450, 1988.
[15] L. H. De Medeiros, G. Reyne, and G. Meunier, "Comparison of Global Force Calculations on Permanent Magnets", *IEEE Trans Magn.*, vol. 34, no. 5, pp. 3560-3563, 1998.

Abbas Shiri was born in Hashtrood, Iran in 1980. He received the B.Sc. degree from Tabriz University and M.Sc. degree from Iran University of Science and Technology (IUST) both in Electrical Engineering in 2004 and 2006, respectively. He is currently working toward Ph.D. degree in Electrical Engineering at IUST.

His areas of research interests include linear electric machines, electromagnetic systems and actuators, electrical machine design and modeling.

Davoud Esmaeil Moghadam was born in Tehran, Iran in 1981. He received the B.Sc. and M.Sc. degrees both in Electrical Engineering in 2004 and 2008, respectively, and is currently working toward Ph.D. degree in Electrical Engineering at Technical University of Dresden (TU Dresden), Germany.

His areas of research interests include electrical machine design and modeling, electromagnetic systems and actuators and electrical insulation for rotating machines.

Accelerated and Robust Computation of Time Domain Floquet Wave-Based Periodic Green's Functions for TD Integral Equations Applications

M. Saviz[1] and R. Faraji-Dana[2]

[1]School of Electrical and Computer Engineering
University of Tehran, Tehran, Iran
msaviz@ut.ac.ir

[2]Center of Excellence on Applied Electromagnetic Systems,
University of Tehran, Tehran, Iran
reza@ut.ac.ir

Abstract **–** A novel approach has been introduced to remedy the computational complexities of the recently introduced time domain periodic Green's functions in the 1D and 2D periodic case. Specifically, it has been shown that for a certain class of temporal basis functions, the computational cost of convolutions with temporal basis functions, which results in the band-limited GFs needed by most time domain integral equations solvers, can be considerably reduced, as compared to conventional methods that are currently in practice. It is also well known that the computational complexity of the Floquet-wave based Green's functions increases when the point of observation approaches a source. Robust forms have been obtained for both 1D and 2D periodic TDGFs for any source-observation distance, which are then further improved for high-efficiency numerical implementation.

Index Terms **–** Time Domain Integral equations, Green's Function, Periodic Structures, Efficient Algorithms.

I. INTRODUCTION

Periodic structures serve as useful models for many real-world problems including antenna arrays and Frequency-selective surfaces and promisingly fast formulations in this area have been recently reported [1-4]. Infinitely extended periodic arrays of sources are amenable to more elegant, and sometimes more convenient mathematical descriptions than those which are finite. In the area of integral equation techniques, and also with many other numerical methods, the "periodic" Green's function refers to the inclusion of the effects of all elements of an array at the observation point (located in the unit cell) in a unified Green's function. This reduces the numerical domain of the original periodic problem to the unit cell of the periodic array. The most straight-forward approach to compute such Green's functions (GF) is to directly sum up the contributions from all elements whose received amplitude at the unit cell is considered to be significant. This direct summation approach (DS) to obtaining such GFs is not computationally efficient, as the resulting series converges rather slowly. In the frequency domain (FD), extensive efforts have been devoted to the problem of finding fast and computationally efficient expressions of the periodic Green's functions and rather efficient implementations do exist. A good review of these can be found in [5]. Such periodic GFs can also be applied in solving finite arrays[6].

Submitted On: May 24, 2012
Accepted On: Aug. 22, 2012

In time domain (TD), analysis of periodic structures has been attempted in recent years [7], based on the TD equivalents of FD Floquet-wave Green's functions developed in [8-11], and further expanded in [12]. Although representations of periodic GFs based on TD-Floquet-wave series (FW) give a more natural approach to a periodic problem, and their corresponding expressions for TDGFs can provide for faster evaluation of impulsive Green's functions, their final implementation in time domain integral equations (TDIE) requires extra convolutions with temporal basis functions (TBFs) and requires special considerations near a source point. These issues greatly affect their speed and efficiency, and consequently, their practical application to TDIE. To the best knowledge of the authors, these aspects have not yet been comprehensively addressed. This paper reports findings related to these important, practical issues.

To have the material needed for further steps, it is necessary to briefly review the Floquet-based Green's functions in section II. Section III introduces the fast convolution technique for periodic time domain GFs with a well-known class of temporal basis functions. Section IV discusses the numerical difficulties encountered when evaluating 1D periodic Floquet-wave GFs close to a source-point, and introduces a novel method to mitigate these effects based on source extraction for the 1D periodic case. We then verify the proposed method through a numerical example. Section V investigates source-proximity improvements for the 2D periodic case, proposes several ways to accelerate the computation of the TDGFs, and verifies the results by numerical examples. Section VI summarizes the contributions of this paper.

II. Preliminaries

Consider a 1D-periodic, infinite, sequentially-excited array of point sources lying along the x-axis, as in Fig. 1.

Considering the surrounding environment of the elements to be free space, and the sequential inter-element delay to be proportional to inter-element spacing X through a factor $\eta = \cos\theta_x$, the sum of potentials contributed by all elements at an observation point (x,y,z) is

$$\tilde{G}(\vec{r},\omega) = \sum_{m=-\infty}^{\infty} \frac{e^{-jmkX\eta} e^{-jkR_m}}{4\pi R_m}, \quad (1)$$

$$G(\vec{r},t) = \sum_{m=-\infty}^{\infty} \frac{\delta\left(t - \frac{R_m}{c} - \frac{m\eta X}{c}\right)}{4\pi R_m}, \quad (2)$$

where $R_m = \sqrt{(x-mX)^2 + \rho^2}$ and $\rho = \sqrt{y^2+z^2}$, and $k = \omega/c$. It has been assumed, in accordance with previous work [8], that the sources are impulsively excited.

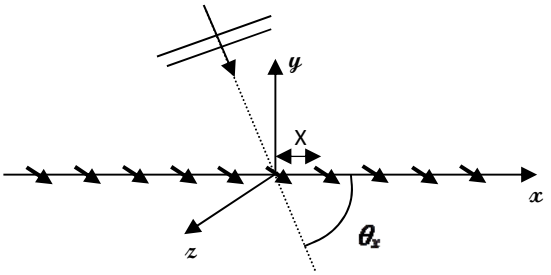

Fig. 1. Linear periodic array of dipole point sources. The plane wave shows one possible way of exciting this array by an inter-element delay of $\eta X = X\cos\theta_x$.

As the denominators in (1) and (2) might suggest, these series converge slowly. Moreover, in many problems, the three dimensional spatial domain of evaluation in (1,2) makes a pre-storage and interpolation approach to their fast evaluation rather expensive and impractical. For this reason, alternative expressions or approximations for these functions are sought. To elaborate the approach in [8], consider the discrete line array of point sources. In frequency domain, one can describe this periodic source structure by (3);

$$\tilde{J}(\omega) = \sum_{m=-\infty}^{\infty} \delta(x' - mX) e^{-jkm\eta X}, \quad (3)$$

which can describe any of the spatial orientations. we can use the Poisson's summation formula $\sum_{m=-\infty}^{\infty} \delta(x'-mX) = X^{-1} \sum_{q=-\infty}^{\infty} \exp(-j2\pi q x'/X)$ to obtain an alternative expression for the sources as:

$$\tilde{J}(\omega) = \sum_{m=-\infty}^{\infty} \delta(x'-mX) e^{-jk\eta x'} = \frac{1}{X} \sum_{q=-\infty}^{\infty} e^{-jk_{xq}x'}, \quad (4a)$$

in which

$$k_{xq}(k) = k\eta + \alpha_q;\ \ \alpha_q = \frac{2\pi q}{X},\ \ q = 0, \pm 1, \pm 2, \ldots \quad (4b)$$

Equation (4) expresses the discrete array of point sources as an infinite summation over smooth linear sources. Correspondingly, the Green's function can be stated in terms of the Green's functions for linear sources; which gives (in frequency domain) [8]

$$\tilde{G}^{FW}(\vec{r}, \omega) = \sum_{q=-\infty}^{\infty} \frac{e^{-jk_{xq}x}}{4jX} H_0^{(2)}(k_{\rho q}\rho), \quad (5)$$

in which $k_{\rho q}(k) = \sqrt{k^2 - k_{xq}{}^2}$. Each of the summands in (5) comprises a Floquet mode. Note that these modes are evanescent away from the linear axis whenever $|k| < |k_{xq}|$, under which the argument of the Hankel function becomes imaginary ($\mathrm{Im}[k_{\rho q}] \le 0$ is assumed, in order to satisfy the radiation condition as $\rho \to +\infty$). The second and fifth FD Floquet-waves are depicted in Fig. 2 for an example with $x = y = 0.25m, z = 0$ in an array with $X = 1m$ and $\eta = 0$. The important cut-off property of these modes before a certain frequency can be readily observed. This implies that for a certain frequency, the summation of a limited number of modes can reconstruct the GF with sufficient accuracy. This is verified in Fig. 3, where the summation of Floquet modes of $|q| \le 2$ has been shown to suffice for an entire frequency region nearly up to the cut-off frequency of the next higher mode.

It can be anticipated that by performing an inverse Fourier transform of the GF in (5), the desirable convergence properties of (5) will carry over to the time domain. Doing so, one arrives at the time domain Floquet modes, with the current modes given by (6) and the corresponding TD Green's functions in (7).

$$J(t) = \frac{1}{X} \sum_{q=-\infty}^{\infty} e^{-j\alpha_q x'} \delta\left(t - \frac{\eta x'}{c}\right). \quad (6)$$

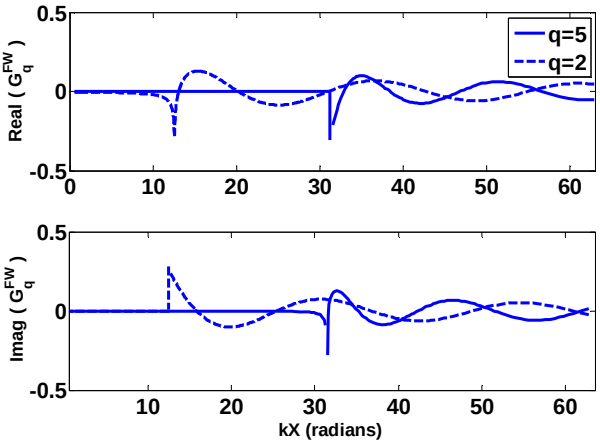

Fig. 2. The 2'nd and 5'th FD Floquet waves observed at $x = y = 0.25m, z = 0$ for an array with $X = 1m$ and $\eta = 0$. The infinity-spikes observed are inherent to periodic Green's functions.

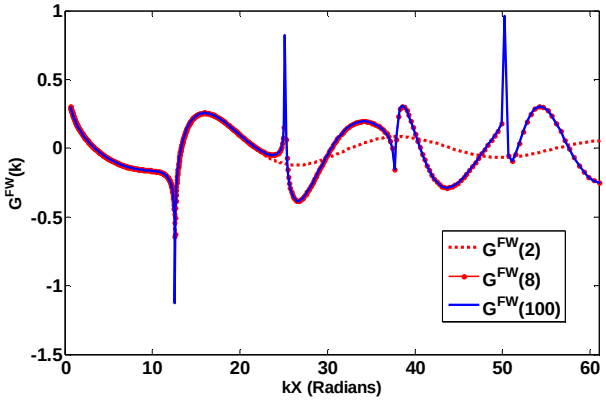

Fig. 3. Comparison between the Floquet GF (5) up to a certain mode number (given in parentheses) and actual (direct summation, equation (1) with 100 terms) observed at $x = y = 0.25m, z = 0$ for an array with $X = 1m$ and $\eta = 0$. Only the real part is shown. The imaginary part shows similar behaviour.

Each TD Floquet current can be interpreted as a traveling impulse excitation along the x-axis, with an x-dependent harmonic amplitude. The resulting TD Green's function can be shown to be, in its most computationally efficient representation [8]:

$$G^{FW}(\vec{r},t) = G_{+}^{FW}(\vec{r},t) + G_{-}^{FW}(\vec{r},t) = \sum_{q=0}^{Q} \varepsilon_q \frac{\cos(\alpha_q x'_{+}(t)) + \cos(\alpha_q x'_{-}(t))}{2\pi X\sqrt{\tau^2 - \tau_0^2}} U(\tau - \tau_0), \quad (7a)$$

where $\varepsilon_q = 1/2$ for $q=0$ and $\varepsilon_q = 1$ otherwise. $U(\tau)$ is the Heaviside function, $\tau = t - \eta x/c$ and

$$x'_{\pm}(t) = x - \frac{c}{1-\eta^2}\left(\eta\tau \pm \sqrt{\tau^2 - \tau_0^2}\right), \quad (7b)$$

$$\tau_0 = \sqrt{1-\eta^2}\,\frac{\rho}{c} = t_0 - \eta\frac{x}{c}. \quad (7c)$$

The physical interpretation of (7) is fairly simple: the instantaneous signal received at the observation point $\vec{r}$ at a certain time t has been contributed by impulsive current excitations at two points $x'_{\pm}$ on the axis; whose sequential excitation and propagation delays have been appropriate for reception at $\vec{r}$ at the time t. These points are time-dependent and are displaced farther away with time.

Of computational significance is the fact that t_0 is independent of q; the mode number. Consequently received signals from all modes begin at the same time t_0 which is, however, dependent on the observation point. Several TD Floquet-wave modes are shown in Fig. 4. It is seen that all modes begin with a sharp variation at t_0 but can be described by different late-time oscillation frequencies (obtained for large t in 7) of

$$\omega_{\pm}^{FWq} = 2\pi\left(\frac{q}{T_X}\right)\left(\frac{1}{1\pm\eta}\right), \quad (8)$$

where we denote the characteristic time scale of the periodic lattice by $T_X = X/c$.

Because the TD Green's function in (2) has been obtained assuming impulsive excitation of point sources, for most numerical applications of Floquet-modes, these have to be convolved with certain TBFs (temporal basis functions or pulse shapes) in order to limit their bandwidth to that appropriate for TDIE simulations (i.e. the band-limited TDGF). The number of Floquet modes required can be estimated by those that have their cut-off below the effective bandwidth of the TBF. Based on the discussion following (5) and approximating the TBF bandwidth by $\Delta\omega = 2\pi/T$, where T is the solver time step, the number of modes that contribute as propagating in the desired bandwidth can be derived as:

$$q < Q = \frac{T_X}{T}\max\left[(1-\eta),(1+\eta)\right]. \quad (9)$$

The number of modes for the case of normal incidence is $Q = T_X/T$. In many problems a choice of $T = 0.1T_X$ can be reasonable for TDIE solutions.

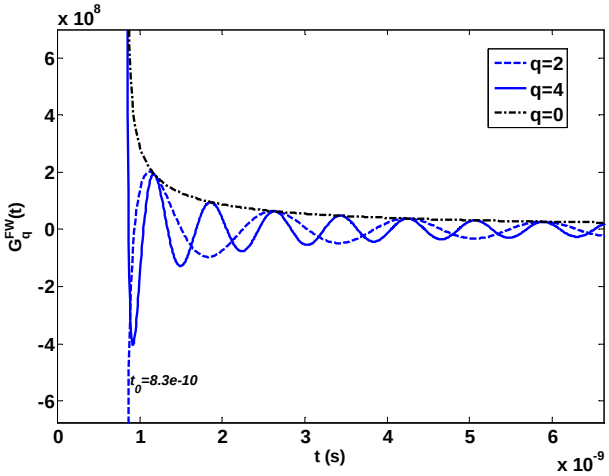

Fig. 4. Time domain Floquet modes from equation (6), for an array with X=1m and $\eta = 0$.

It can be verified from the number of terms needed to produce agreement with the actual GF in Fig. 5a, that the TD Green's function in (7) has indeed inherited the desirable convergence properties of their FD counterpart (5). Here a QB-spline basis function with $T = T_X$ has been used as the temporal basis functions, for which mode indices as low as $Q = 1$ should be sufficient according to (9). Other parameters in Fig. 5a are similar to the previous FD example.

In spite of the efficient number of required modes, the necessary convolutions $G_q^{FW}(t) * g(t)$ usually have to be performed numerically at a temporal discretization of about $\Delta t < 0.1\min\left[T, 2\pi/Max(\omega_{FW})\right]$. This is typically more than an order of magnitude smaller than the time step T in a typical TDIE solver (e.g. based on the marching-on-in-time method) which needs the TDGF to be obtained at integer multiples of T only. This makes the convolution time-consuming. Indeed, for short simulation times T_{sim}, the higher

resolution in time that is required to perform the convolution with accuracy, increases the total computational cost of the Floquet-based approach beyond that of direct summation of element Green's functions at integer multiples of T(see Fig. 9). We shall assume from now on that Δt is chosen so that T is an integer multiple of Δt .

It is usual in TDIE solvers such as MoT to use temporal basis functions which have a temporal support of one to several T. The ratio $N_b = T/\Delta t$ will be useful in later discussions.

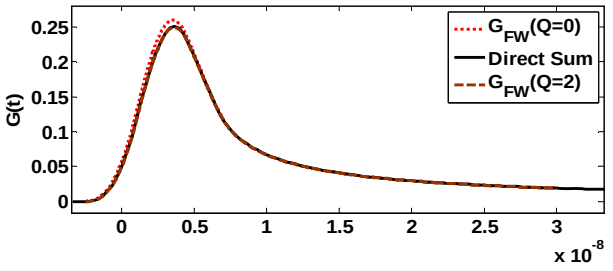

(a)

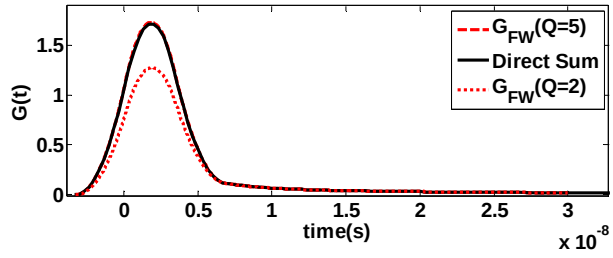

(b)

Fig. 5. Band-limited Time domain Green's functions obtained by direct summation (equation 2) and Floquet-waves (11) for a. $x = y = 0.25m, z = 0$ and for b. $x = y = 0.025m, z = 0$.

It is also well known when using the TDGFs of (7) that a higher number of modes are needed when the point of observation approaches a source point (e.g. the origin in (2)). This can be seen in Fig. 5b where the point of observation has been moved to $x = y = 0.025m, z = 0$ for the same array of the previous example. The reason for this can be traced back to the FD Floquet GFs in (5). At low values of ρ , the evanescent tails of the Hankel functions become more and more pronounced below their cut-off frequencies, and at $\rho = 0$ a smooth, constant value can be contributed by these modes in the bandwidth of interest. Consequently the number of higher order Floquet modes required to reproduce the TDGF grows enormously as $\rho \to 0$, and a computation using Floquet series would be far from efficient. This does not come as a surprise, as it is generally known that modal expansions of GFs perform best for far-fields and direct summations perform best for near-fields. This problem affects the accuracy of self-patch terms in the MoT coefficients matrix, and can trigger instabilities in the TDIE solution.

As the 2D periodic problem has the same essential features observed in the above discussion of the 1D periodic case, we do not present an introduction for them here. We refer the interested reader to [9,10] for a detailed discussion. After considering an accelerated method of convolution in section 3, section 4 and 5 provide modifications of expressions like (7) to overcome the accuracy problem while maintaining computational efficiency, for the 1D and 2D periodic problems respectively. To facilitate the following discussion, many of the related symbols and parameters have been defined and described in Table 1, with their typical values. Other symbols will be defined when they are first used in the text.

Table 1: Symbols that are repeatedly used throughout the paper.

Symbol	Description	Typical Value
T	Solver *time step*. The time support of the temporal basis function (TBF) can be one to several (denoted n_{TBF}) *time steps.*	For min. excitation wavelength of $O(X)$, $T \sim 0.1(X/c_0)$.
T_{sim}	The time limit up to which (starting at t=0) the TDGF has to be computed for a certain TD problem.	
N_{sim}	The length of the computer vector of time samples, for which the GF has to be computed. $N_{sim} = \lceil T_{sim} / T \rceil$.	> 100
Δt	Because of the numerical convolution of the Floquet-modes with the TBF, the floquet modes have to be computed at a higher resolution $\Delta t < T$.	$\Delta t \sim 0.1T$, usually chosen so that T is an integer multiple of Δt .
N_b	$N_b = \lceil T / \Delta t \rceil$, also the length of the MA filter in section 3.	*10-50*

III. Efficient computation of convolutions with TD Green's functions

Stable TDIE formulations have been reported using the B-spline family of temporal basis functions and marching in time (MoT) solvers[13,14]. B-spline pulses are piecewise-polynomial functions and provide compact support in time, which ensures the sparsity of MoT matrices at later time steps. A B-spline pulse of order m can be built through the following desirable property[15]:

$$b_0(t) = rect(\frac{t}{T})$$
$$b_m(t) = \frac{1}{T} b_0(t) * b_{m-1}(t), \quad m \in \mathbb{N} = \{1,2,...\}. \tag{10}$$

The *zero'th order* B-spline is the simple rectangular pulse of width *T*. The first order can be obtained by convolving the rectangular pulse function by itself and dividing by *T*, which gives the rather common roof-top, or triangular basis function. Convolving once more with the rectangular pulse function results in the second order or Quadratic B-spline (QB-spline) function which has been used in the time domain integral equations developed in[13,15]. As noted in [13] the time derivative of the QB-spline basis functions are continuous, which makes them suitable for EFIE formulations, where time derivatives of the basis functions appear. We note that to construct the TBFs, the QB-spline and higher B-splines are used with positive time shifts so that the TBF equals zero for $t < -T$. This is important for a causal TDIE solver such as MoT.

The property in (8) can be used to efficiently compute the convolution with B-splines. To elaborate, consider the convolution of a QB-spline basis $b_2(t)$ with $G(\vec{r},t)$ of (7). We shall denote the band-limited TDGFs by $S_m(t)$, where m shows the order of the basis function used. Consider rewriting the convolution as:

$$S_2(t) = G(t) * b_2(t) = \frac{1}{T^2} G(t) * \left[b_0(t) * b_0(t) * b_0(t) \right]$$
$$= \frac{1}{T^2} \left[G(t) * b_0(t) \right] * b_0(t) * b_0(t) \tag{11}$$

We shall first concentrate on convolving $b_0(t)$ namely:

$$S_0(t) = G(t) * b_0(t) = \int_{-\infty}^{\infty} G(\tau) b_0(t-\tau) d\tau. \tag{12}$$

Computer implementation of (12) requires discretization in time. Assuming a sampling interval of Δt we will denote the discrete waveform of the signal $S(t)$ by $S[n] = S(n\Delta t)$, and the computer vectors which can only have positive integers as indices will be denoted by the bold caharacter **S**(j). Every vector starts with the first nonzero sample of the corresponding signal. Thus **G**(1) corresponds to $G(t_0)$ and **b**(1) corresponds to $b_0(-T/2)$. Keeping these in mind, we shall only use the computer vectors in the following to facilitate the discussion. The convolution is:

$$\mathbf{S}_0(i) = \sum_j \mathbf{G}(j) \mathbf{b}_0(i-j+1). \tag{13}$$

There are only $N_b = T/\Delta t$ nonzero samples in $\mathbf{b_0}$. The constant, unity amplitude of $\mathbf{b_0}$ in this range allows to avoid the multiplication step in the process of convolution. Computing the convolution therefore reduces to finding the sum of N_b elements of **G** at each step *i*. This provides for a "Moving Average" (MA) Interpretation of the convolution in (13). This procedure would cost half that of direct convolution, because it avoids one multiplication for every summation in (13). Nevertheless, the procedure can be done still much faster. It is known, mostly among the image-processing community, that two-dimensional moving averages can be computed with high efficiency "Box-filtering" Techniques [16]. We show the one-dimensional application of the idea to the problem in hand. Suppose the moving average has been computed for the first N_b samples of the signal G. The moving average window then slides one sample to the right to compute the next N_b -sum. However, It suffices at this step to subtract one of the previous samples (i.e. the earliest), and add one new sample (Fig. 6) to the output of the previous step. This involves only two operations per step instead of N_b in a conventional MA.

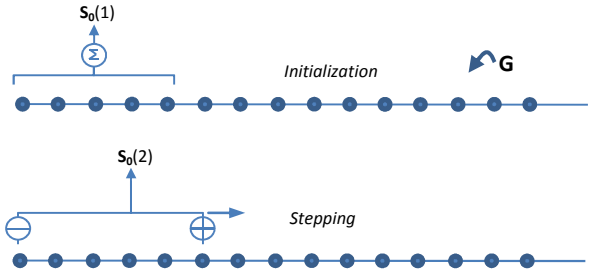

Fig. 6. The convolution with b_0 as a moving average with higher efficiency.

From a programing point of view, in the MA method of Fig. 6, **G** has to be padded with $N_b - 1$ zeros at its beginning. In this way the first element of $\mathbf{S_0}$ will correspond to $S_0(t_0 - T/2)$, and through the convolution in (12), $S_0(t)$ is indeed known to be nonzero only after $t = t_0 - T/2$. Considering N_G to be the number of elements in **G,** The whole process has a computational complexity of $2N_G$ only.

An efficient sample algorithm for one iteration is shown below (all time samples are computed simultaneously by vectorized programming).

1. Compute the difference for all time samples with the ones shifted by N_b samples:

```
PGF(Nb+1:end)= PGF(Nb+1:end)-PGF(1:end-Nb)
```

2. Compute the cumulative summation:

```
PGF=cumsum(PGF),
```

where `cumsum` stands for cumulative summation, i.e. a vector that has the same length as the input whose elements are obtained by cumulatively adding the input elements, with its first element being equal to the first of the input. In order to compute the desired convolution with $b_2(t)$, the same process has to be iterated three times according to (11) and the final result multiplied by a constant $\Delta t^3 T^{-2}$. The whole computational complexity of this method is then only $7N_G$. The first element of $\mathbf{S_2}$ obtained after three iterations corresponds to $S_2(t_0 - 3T/2)$, which is indeed the starting time for $S_2(t)$. We shall note that for a shifted QB-spline basis function [13,15] which starts at $t = -T$, the above procedure remains the same, and the first element of $\mathbf{S_2}$ obtained after three iterations is simply assigned to $S_2(t_0 - T)$. Furthermore, the first time-deriviative of the TDGF can be obtained by simply omitting the final cumulative sum.

IV. COMPUTATION OF THE TD GREEN'S FUNCTION CLOSE TO A SOURCE: 1D PERIODICITY

A. Formulation

Although the procedure described above can provide for efficient computation of TDGF, at observation points close to a source, the number of Floquet modes that have to be considered for an accurate reconstruction of the TDGF increases beyond those that are considered as propagating in the TBF bandwidth. The problem has been already discussed in section 2. It would be of advantage to find a robust procedure for the evaluation of the TDGF, which overcomes the source-proximity problem and can still benefit from the fast computational techniques of the previous section.

We see from Fig. 5 that the discrepancy is an early-time phenomenon. At these times the TDGF values can be attributed to the signal received from the nearby sources. Because in a TDIE we only have observation points in the unit interval of the periodic array, i.e. $x \in (0, X)$, we can extract the two near-by sources on both sides of the unit interval and add their contribution separately. Using (2) as our starting point, we have:

$$\begin{aligned} S_{1D}(\vec{r},t) = &\sum_{n=-\infty}^{-1} \frac{g\left(t - \frac{R_n}{c} + \frac{\eta X}{c}\right)}{4\pi R_{-1}} \\ &+ \frac{g\left(t - \frac{R_0}{c}\right)}{4\pi R_0} + \frac{g\left(t - \frac{R_1}{c} - \frac{\eta X}{c}\right)}{4\pi R_1} \\ &+ \sum_{n=2}^{+\infty} \frac{g\left(t - \frac{R_n}{c} - \frac{2\eta X}{c}\right)}{4\pi R_2}. \end{aligned} \tag{14}$$

For the rest of the array, we then use the Floquet modes of two semi-infinite linear periodic arrays. Details of deriving these modes are given in [9]. A semi-infinite linear array lying over $[0, +\infty)$ has the truncated GF G^T given in (13):

$$\begin{aligned} G^T(\vec{r},t) = &\frac{\delta\left(t - \frac{R_0}{c}\right)}{8\pi R_0} \\ &+ G_-^{FW} U\left(x'_+(t)\right) \\ &+ G_+^{FW} U\left(x'_-(t)\right), \end{aligned} \tag{15}$$

Where G_+^{FW}, G_-^{FW} come from the TDGF of the infinite array as in (7), corresponding to terms with x'_+, x'_- respectively. The first term in (15) is the spatial TDGF of the single element at the truncated end, divided by two. We rewrite this for the two series in (14) and simplify to arrive at (16), which is written in its most computationally compact form:

$$\begin{aligned} S_{1D}(\vec{r},t) = &\frac{g\left(t - \frac{R_0}{c}\right)}{4\pi R_0} + \frac{g\left(t - \frac{R_1}{c} - \frac{\eta X}{c}\right)}{4\pi R_1} \\ &+ \frac{g\left(t - \frac{R_{-1}}{c} + \frac{\eta X}{c}\right)}{8\pi R_{-1}} + \frac{g\left(t - \frac{R_2}{c} - \frac{2\eta X}{c}\right)}{8\pi R_2} \\ &+ G^{RE} * g(t), \end{aligned} \tag{16a}$$

where

$$\begin{aligned} G^{RE} = &G_+^{FW} . \left[1 - U\left(x'_+(t) + 1\right) \cdot U\left(2 - x'_+(t)\right)\right] \\ &+ G_-^{FW} . \left[1 - U\left(x'_-(t) + 1\right) \cdot U\left(2 - x'_-(t)\right)\right] \end{aligned} \tag{16b}$$

and $U(\cdot)$ is the Heaviside function. The terms in brackets in (16b) effectively extinguish the Floquet-mode contributions from the region between the point sources corresponding to m= -1 and m=2. The result in (16) is quite general and not limited to using B-spline functions for g(t). Using (16), High accuracy reconstruction of the final band-limited TDGF can be obtained at both early and late times without including higher order modes.

For B-spline functions, the implementation of convolutions in (16) can benefit from the simplification and convolution-acceleration technique discussed in the previous section. Furthermore we can incorporate the four leading terms in (16) in the convolution process, by considering $g(t-a)=\delta(t-a)*g(t)$. For computer implementation, we insert four samples in the computer vector corresponding to G^{RE} prior to convolution with $g(t)$. These samples correspond to discrete versions of the Dirac delta function, whose amplitudes and locations are shown in Table 2 in order to facilitate the reproduction of our results.

By the process of moving averages, these will automatically give rise to the four direct terms, thereby avoiding programming calls to evaluate $g(t)$ altogether. The desired values of the TDGF for a TDIE solver which runs at steps of T are then obtained by down-sampling by N_b.

Table 2: Locations and amplitudes of the four discrete impulse functions to numerically generate the first four terms in (16)

Corresponding term in (16)	Sample Amplitude	Location[a]
$\dfrac{g\left(t-\dfrac{R_0}{c}\right)}{4\pi R_0}$	$\dfrac{\Delta t^{-1}}{4\pi R_0}$	$\left\lceil \dfrac{R_0}{c}-t_0 \right\rceil$
$\dfrac{g\left(t-\dfrac{R_1}{c}-\dfrac{\eta X}{c}\right)}{4\pi R1}$	$\dfrac{\Delta t^{-1}}{4\pi R_1}$	$\left\lceil \dfrac{R_1}{c}+\dfrac{\eta X}{c}-t_0 \right\rceil$
$\dfrac{g\left(t-\dfrac{R_2}{c}-\dfrac{2\eta X}{c}\right)}{4\pi R_2}$	$\dfrac{\Delta t^{-1}}{4\pi R_2}$	$\left\lceil \dfrac{R_2}{c}+\dfrac{2\eta X}{c}-t_0 \right\rceil$
$\dfrac{g\left(t-\dfrac{R_{-1}}{c}+\dfrac{\eta X}{c}\right)}{4\pi R_{-1}}$	$\dfrac{\Delta t^{-1}}{4\pi R_{-1}}$	$\left\lceil \dfrac{R_{-1}}{c}-\dfrac{\eta X}{c}-t_0 \right\rceil$

[a]The element location assumes the first element of the computer vector $\mathbf{G}^{\mathbf{RE}}$ to correspond to t_0.

B. Numerical example

We shall now consider an example where the observation point is extremely close to the source, i.e. $x=y=0.00025m, z=0$ in an array with $X=1m$ and $\eta=0$ and by choosing $T=0.1T_X$. The results for this example are shown in Fig. 8. The accuracy of (16) has been compared against the previous pure-Floquet-modes approach. The number of modes in both cases are the same, and are chosen as low as indicated by (9). In addition to the capability of accurate reconstruction, the formula in (16) is free from the Gibbs-phenomenon at early times. It smoothly joins the Floquet-modes results. at later times, where they are more accurate.

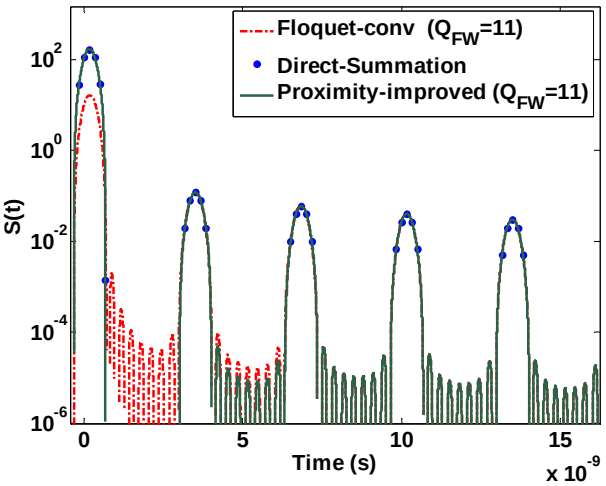

Fig. 8. Comparison of the Floquet-convolution approach with the proximity- improved formula in (16). As the amplitude of the first peak is at least two orders of magnitude higher than others near the source point, a logarithmic scale has been chosen to observe the whole-range function behaviour.

In Fig. 9 we compare the performance of several methods of computing the convolution in the proximity-improved function $S_{1D}(\vec{r},t)$ in (16). This is done by implementing all methods in MATLAB programming environment and running the computations for increasing simulation times T_{sim}. In this way the computation load on each method is increased by increasing the number of required time samples (vector length), while keeping a constant $\Delta t=0.01\min\left[T,\,2\pi/\max(\omega_{FW})\right]$ for accurate numerical convolutions. The temporal basis functions are QB-spline pulses and for each value of T_{sim}, the total computer time required to perform the GF calculation for t=-T to T_{sim} is taken

as an approximate indicator of computational cost.(Considering the faster implementation of built-in functions, this might not be a fair criterion, i.e. underestimating the proposed method. Nevertheless, we expect to have at least a correct qualitative comparison.)

Convolution and FFt-based Floquet refer to evaluating the first four terms of (16) directly and using either direct convolution or FFt-based convolution to evaluate the fifth term. Floquet-MA refers to implementing Table 1 and using the MA convolution scheme. To perform a fair comparison, we note that direct summation (DS) needs to evaluate no more than $M_{DS} = T_{sim} / T_X + 1$ individual elements at both sides of the origin, as the contribution from other elements of the lattice arrive later than $t = T_{sim}$. furthermore, in accordance with a real TDIE scenario, only samples at integer multiples of T are required, which amount to $N_{sim} = T_{sim} / T$ time points. These indicate that direct summation GFs can have low computational time for small simulation times. The rise in Computation time is, however, proportional to $M_{DS} N_{sim}$, which is $O\left(N_{sim}{}^2\right)$, as evidenced by the corresponding slope in Fig. 9. Direct numerical convolution will have a computational cost of at least $2N_G N_b$, which is $O\left(N_{sim}\right)$. Indirectly computing the convolution by means of three times Fast Fourier Transforms (two times FFT, and one inverse FFT) all of equal lengths N_G will result in a cost of $O(N_{sim} \log(N_{sim}))$ [17], and might not necessarily be more efficient than direct convolution for all N_{sim}. Finally, the proposed method, which relies on a moving-average (MA) scheme and needs no evaluation of g(t), has a computational cost of $7N_G$ only and has considerably better efficiency. In Fig. 9, all Floquet-based computation times also include the time to compute the Q+1 Floquet-modes, prior to convolution.

V. COMPUTATION OF THE TD GREEN'S FUNCTION CLOSE TO A SOURCE: 2D PERIODICITY

This section extends the previous investigation to doubly periodic GFs and discusses some specific points for more efficient programming. To preserve notational simplicity, we reuse some of the symbols from the previous sections with new meanings specific to the 2D periodic GF.

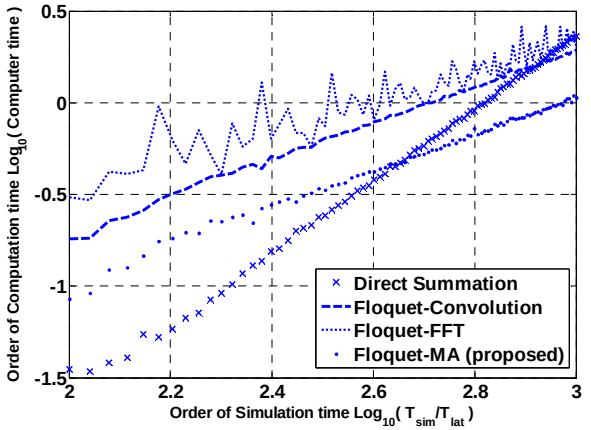

Fig. 9. Comparison of the computation times for the proposed method with several other approaches.

A. Formulation

For a sequentially excited doubly-periodic array of point-dipole elements, which has unit cell dimensions of X and Y as shown in Fig. 10, one can readily write the field at an observation point (x,y,z) as a summation over all elements in Frequency domain (FD) and time domain (TD):

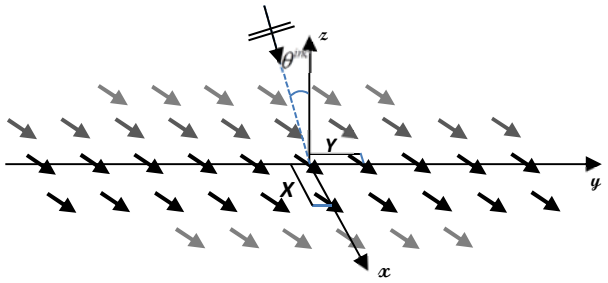

Fig. 10. Schematic description of the infinite doubly periodic array. The hypothetical plane wave shows one possible way to excite this array by an inter-element delay of $\eta \hat{u}^{inc} = \eta \cos\varphi^{inc} \hat{x} + \eta \sin\varphi^{inc} \hat{y}$, where $\eta = \sin\theta^{inc}$

$$\tilde{G}(\vec{r},\omega) = \sum_{m=-\infty}^{\infty} \sum_{n=-\infty}^{\infty} \frac{\exp\left[-jk\left(R_{mn} + mX\eta\cos\varphi^{inc} + nY\eta\sin\varphi^{inc}\right)\right]}{4\pi R_{mn}} \tag{17}$$

$$G(\vec{r},t) = \sum_{m=-\infty}^{+\infty} \sum_{n=-\infty}^{+\infty} \frac{\delta\left(t - \frac{R_{mn}}{c} - \eta\frac{mX\cos\varphi^{inc} + nY\sin\varphi^{inc}}{c}\right)}{4\pi R_{mn}} \tag{18}$$

where $R_{mn} = \sqrt{(x - mX)^2 + (y - nY)^2 + z^2}$ and $k = \omega/c$, and η, φ^{inc} and θ^{inc} have been explained

in Fig. 1. We note that the symbol η is reused form the previous section and $\eta = \sin\theta^{inc}$. It has been assumed in (18), in accordance with previous work [10], that the sources are impulsively excited. Direct computation of (17) and (18) is even more costly than in the 1D case (considering that the minimum number of elements now varies with the square of the simulation time). As in the 1D periodic case, for both FD and TD, the Floquet-wave representations can very efficiently reconstruct the TDGF (18); in most cases requiring up to only a few tens of modes to converge. The 2D periodic TD modes are given in (3) as:

$$G^{FW}(\vec{\rho},z,t) = \sum_{p=0}^{\infty}\sum_{q=-\infty}^{\infty}\varepsilon_p \frac{c\cos\left[\alpha_{pq}.(x\hat{x}+y\hat{y})-\bar{\omega}_{pq}\tau\right]}{XY\sqrt{1-\eta^2}} \times J_0\left(\tilde{\omega}_{pq}\sqrt{\tau^2-\tau_0^2}\right)U(\tau-\tau_0), \quad (19a)$$

where $\varepsilon_p = 1$ for $p \neq 0$ and $\varepsilon_p = 1/2$ for $p = 0$, $J_0(\cdot)$ denotes the zero'th order Bessel function and $U(\cdot)$ the Heaviside function, and the parameters are[10]:

$$\begin{aligned}
&\eta = \sin\theta^{inc} \quad , \quad \hat{u}^{inc} = \cos\varphi^{inc}\hat{x} + \sin\varphi^{inc}\hat{y} \\
&\alpha_{pq} = \frac{2\pi p}{X}\hat{x} + \frac{2\pi q}{Y}\hat{y} \\
&\bar{\omega}_{pq} = \frac{\eta c}{1-\eta^2}\hat{u}^{inc}\cdot\alpha_{pq} \\
&\tilde{\omega}_{pq} = \sqrt{\bar{\omega}_{pq}{}^2 + \alpha_{pq}{}^2 c^2/1-\eta^2} \\
&\tau = t - \frac{\eta}{c}\hat{u}^{inc}\cdot(x\hat{x}+y\hat{y}) \\
&\tau_0 = \frac{\sqrt{1-\eta^2}}{c}z,
\end{aligned} \quad (19b)$$

and it has to be reminded that to produce the band-limited GFs that are necessary in the implementation of TD integral equation solvers, the TDGF in (19) has to be convolved with a TBF (denoted $g(t)$), which we consider to have a bandwidth of approximately T^{-1}, where T is the solver time step. The efficiency of (19) can be understood by a glance at Fig. 11, where the reconstruction process is shown in both time and frequency domains. It is seen that away from the x-y plane, the evanescent character of higher modes in FD below $f=T^{-1}$ enables a limited number of modes to reproduce the band-limited TDGF. Nevertheless, as $|z| \to 0$, Like the 1D case, it is the early time of the TDGF that is affected. For a 2D periodic TDGF, this is more rigorously shown in [11; Appendix].

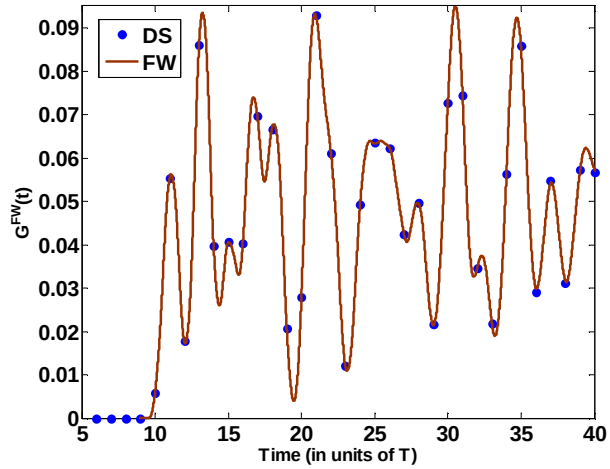

(a)

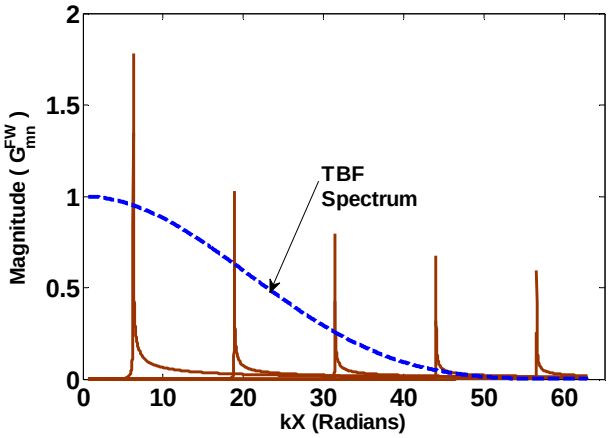

(b)

Fig. 11. (a) The 2D periodic TDGF for an example with $x = y = 0.25m, z = 1$ in an array with $X = Y = 1m$ and $\eta = 0$ where we have chosen $T = 0.1X/c_0$ for the TBF. Only modes with $|p|,|q| \le 10$ have been used. (b) the frequency domain description for the same example shows a limited number of modes being "selected" by the TBF spectrum. The FD modes shown correspond to $p = 0, q = 1,3,5,7,9$.

On the other hand, direct summation is most efficient for early times, because at early times one

can exclude from the summation in (18), all the element signals that have not yet arrived at the observation point (The observation point resides in the unit cell). Consequently, as with the 1D periodic GF, we seek a combination that uses direct summations at early times and Floquet-mode GFs at later times. However, unlike the 1D case, it might be easier here to separate the two methods in time, rather than in space. In [7], it has been suggested to separate the very early-time and compute it directly, and treat the later times with Floquet-modes. The following approach for 2D periodic GFs uses a similar technique in combining DS and Floquet-series. Additionally, we treat the TDGF explicitly, and optimize its computational procedure to arrive at a formulation which is accurate, and still more efficient computationally from either of the DS, or FW formulations.

A separation of the two methods in time requires defining a transition time T_{trans}. The simulation time T_{sim} is then divided into two parts, namely $0<t< T_{\text{trans}}$, and $T_{trans}<t<T_{sim}$. For the first part, the evaluation of the TDGF is done using direct summation in (18) with a limited number of elements determined by T_{trans}. The remaining time points after and including T_{trans} can be computed by Floquet-series. We can thus write:

$$S_{2D}\left(\vec{r}, t < T_{trans}\right) = \sum_{m=-M}^{+M}\sum_{n=-N}^{+N} \frac{g\left(t_{DS} - \frac{R_{mn}}{c} - \eta\frac{mX\cos\varphi^{inc} + nY\sin\varphi^{inc}}{c}\right)}{4\pi R_{mn}}$$

$$S_{2D}\left(\vec{r}, t \geq T_{trans}\right) = \left\{\sum_{p=0}^{P}\sum_{q=-Q}^{Q}\varepsilon_p \frac{c\cos\left[\alpha_{pq}.\left(x\hat{x}+y\hat{y}\right) - \bar{\omega}_{pq}\tau_{trunc}\right]}{2XY\sqrt{1-\eta^2}} \times J_0\left(\tilde{\omega}_{pq}\sqrt{{\tau_{trunc}}^2 - \tau_0^2}\right)\right\} * g(t), \quad \text{(20a)}$$

where

$$t_{DS} = jT, \quad j = 0,1,...,N_{trans}-1.$$
$$N_{trans} = T_{trans}/T.$$
$$M = \left\lceil \frac{T_{trans}}{X/c} \right\rceil + 1,\ N = \left\lceil \frac{T_{trans}}{Y/c} \right\rceil + 1$$

$$t_{trunc} = t_{trans} - (n_{TBF} - 1)T + i\Delta t, \quad i = 0,1,2,...$$
$$\tau_{trunc} = t_{trunc} - \frac{\eta}{c}\hat{u}^{inc}\cdot\left(x\hat{x}+y\hat{y}\right). \quad \text{(20b)}$$

Like the 1D case, we note in (20b) that the truncated time vector for the Floquet-part has samples with $\Delta t < T$ for accurate numerical convolution. We also note that to have the correct value at $t = T_{trans}$ after convolution with $g(t)$, the Floquet-series has to be computed from $(n_{TBF}-1)T$ seconds before $t = T_{trans}$, where n_{TBF} is related to the temporal support of the $g(t)$; assumed to be $\left[-T, (n_{TBF}-1)T\right]$. As the final TDGF is required at samples that are T seconds apart, the Floquet-wave part of (20a) has to be properly trimmed at the beginning and down-sampled by N_b, before the two parts are appended. All other parameters, including P and Q are treated as before.

It remains to choose a proper value for T_{trans}. It is shown in [7] that the Floquet-modes inefficiency appears at times on the order of the width of the TBF pulse after t_0. We set $T_{trans} = t_0(x,y,z) + n_{trans}T$ with $n_{trans} = 10$ as a typical value. Further remarks on accelerating the computation of (20) and a numerical example will elucidate these points.

B. Practical aspects and Numerical verification

It becomes evident in the computer implementation of (20a) that the evaluation of the special function $J_0(\cdot)$ can be highly time-consuming. This computational cost can be mitigated in the formula (20a) because by virtue of the third property in (20b), the argument of the Bessel function is guaranteed to be real for all $t > t_{trans}$. Therefore, in addition to using real arithmetic, the Bessel function itself can be obtained by 1D linear interpolation on a table of Bessel function values for real samples which needs to be calculated only once. The Heaviside function in (19) is no more necessary and is removed in (20), because it always equals unity for all $t > t_{trans}$. Furthermore, for the B-Spline family of temporal basis functions, the accelerated convolution method based on moving averages can be used as with the 1D periodic case. However, its contribution to efficiency will be relatively small

here, as the main computational cost for the 2D periodic case now arises from the evaluation of the 2D Floquet modes (their total number being typically one order of magnitude higher than the 1D case) prior to convolution, which dominates over the cost of convolutions.

In Fig. 12 we show the TDGF for a close-to-source observation point; $x = y = 0.0025m, z = 0$ in an array with $X = Y = 1m$ and $\eta = 0$. The time step is defined as $T = 0.1X / c_0$. For Floquet series, P=Q=10 is used and the Floquet modes are obtained at a higher resolution for numerical convolution with the TBF, determined by $\Delta t = 0.1\min\left(T, 2\pi / \omega_{FW\max}\right)$. The TBF is the QBspline function. It is seen that the proximity-improved formula (20) is exact at both early and late times.

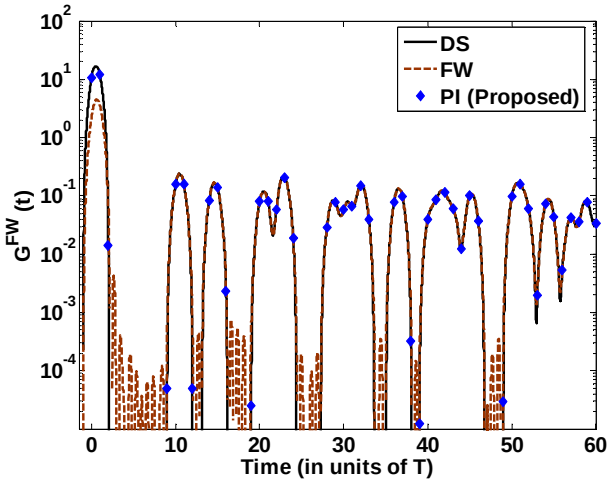

Fig. 12. An example of the near-to-source observation point $x = y = 0.0025, z = 0$ in a 2D periodic array with $X = Y = 1$ and $\eta = 0$. The point of transition corresponds to 42T. the proximity improved (PI) method (20) is exact at both early and late times.

To show the efficiency of the above-mentioned techniques, in Fig. 13 we perform a comparison between the computational efficiencies of direct summation, conventional Floquet-series with direct convolution but with either direct evaluation of Bessel functions or their interpolation, and the proximity-improved method of (5) implemented with the above-mentioned computational techniques, i.e. interpolation for Evaluation of Bessel functions and MA-based convolutions. Because at least O(N_{sim}^2) elements have to be summed for each of the time samples up to T_{sim}, the computational cost of direct summation scales with $O(N_{sim}^3)$. The Floquet-series methods and the Proximity-improved formula have computational times of $O(N_{sim})$. It can be also seen that the main cost is determined by how the computation of the modes, and in particular the Bessel function, is done. The proposed, proximity-improved method is seen to have a computation time as low as, or better than both DS and the conventional Floquet-series.

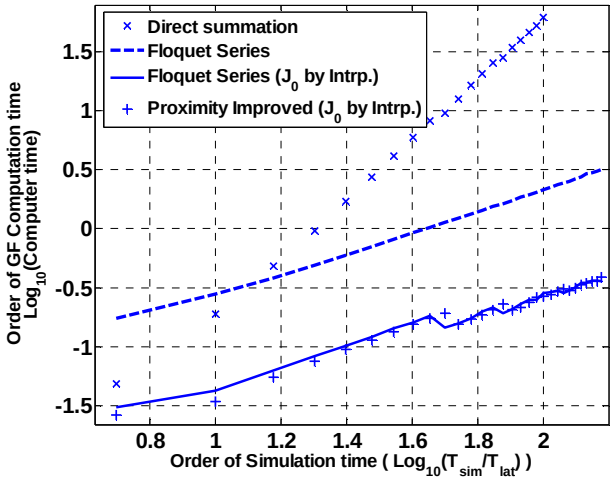

Fig. 13. Comparison of the computation times for the proposed method with several other approaches.

VI. CONCLUSION

We have presented solutions to some of the practical computational challenges of time domain GFs with regard to their implementation in TDIE solvers. It has been shown that for the B-spline basis functions the cost of numerical convolution with basis functions can be reduced by employing an iterative Moving average scheme. Furthermore the inefficiency and the need for higher order modes in the Floquet-series when the observation point approaches a source point is addressed for both the 1D and 2D periodic TDGFs. For the 1D periodic case the problem has been solved by spatially separating the sources adjacent to the unit-interval and treating the remaining sources by the Floquet modes of truncated, semi-inifinite arrays. For the 2D periodic case, we temporally separate the computation of the GF into early and late times, and treat the early times efficiently by direct summation. Several computational

techniques were introduced to accelerate the computation of the obtained results. Together, the contributions presented in this paper can provide for more robust and efficient computation of TDGFs, needed in filling the TDIE coefficients matrices, at both early and late times.

ACKNOWLEDGMENT

M. Saviz thanks Prof. Dr. M. Clemens, Director of the Chair of Electromagnetic Theory, University of Wuppertal for facilitating this research. This work has been partially supported by the Iran Telecommunication Research Center (ITRC) through a research grant.

REFERENCES

[1] A. B. Ali, E. A. Hajlaoui, A. Gharsallah, "Efficient Analysis Technique for Modeling Periodic Structures based on Finite Element Method using High-order Multiscalets Functions," *Applied Computational Electromagnetics Society (ACES) Journal*, vol. 25, no. 9, pp. 755-763, Sept. 2010.

[2] C. Craeye, D. G.-Ovejero, X. Dardenne, "Efficient Numerical Analysis of Arrays of Identical Elements with Complex Shapes" *Applied Computational Electromagnetics Society (ACES) Journal*, vol. 24, no. 2, pp. 224-232, Apr. 2009.

[3] L. E. R. Petersson and J. M. Jin, "A Three-dimensional Time-domain Finite-element Formulation for Periodic Structures," *IEEE Trans. on Antennas Propagat.*, vol. 54, no. 1, pp. 1656-1666, Jan. 2006.

[4] L. E. R. Petersson and J. M. Jin, "A Two-dimensional Time-domain Finite-element Formulation for Periodic Structures," *IEEE Trans. on Antennas Propagat.*, vol. 53, no. 4, pp. 1480-1488, Apr. 2005.

[5] G. Valerio, P. Baccarelli, P. Burghignoli and A. Galli, "Comparative Analysis of Acceleration Techniques for 2-D and 3-D Green's Functions in Periodic Structures Along One and Two Directions," *IEEE Trans. Antennas Propagat.*, vol. 55, pp. 1630, 2007.

[6] A. Cucini, S. Maci, "Macro-Scale Basis Functions for the Method of Moment Analysis of Large Periodic Microstrip Arrays," Applied *Computational Electromagnetics Society (ACES) Journal*, vol. 21, no. 3, pp. 256-266, November 2006.

[7] N-W. Chen, M. Lu, F. Capolino, B. Shanker and E. Michielssen, "Floquet-wave-based Analysis of Transient Scattering from Doubly Periodic Discretely Planar, Perfectly Conducting Structures," *Radio Sci.*, vol. 40, RS4007, 2005.

[8] L.B. Felsen and F. Capolino, "Time Domain Green's Function for an Infinite Sequentially Excited Periodic Line Array of Diploes," *IEEE Trans. Antennas Propagat.*, vol. 48, no. 6, pp. 921-931, Jun. 2000.

[9] F. Capolino and L.B. Felsen, "Frequency and Time Domain Green's Functions for a Phased Semi-Infinite Periodic Line Array of Dipoles," *IEEE Trans. Antennas Propagat.*, vol. 50, no. 1, pp. 31-41, Jan. 2002.

[10] F. Capolino and L.B. Felsen, "Time Domain Green's Functions for an Infinite Sequentially Excited Periodic Planar Array of Dipoles," *IEEE Trans. Antennas Propagat.*, vol. 51, no. 2, pp. 160-170, Feb. 2003.

[11] F. Capolino and L.B. Felsen, "Frequency and Time Domain Green's Functions for a Phased Semi-Infinite Periodic Line Array of Dipoles," *IEEE Trans. Antennas Propagat.*, vol. 50, no. 1, pp. 31-41, Jan. 2002.

[12] J. Gao and B. Shanker, "Time Domain Weyl's Identity and the Causality Trick Based Formulation of the Time Domain Periodic Green's Function," *IEEE Trans. on Antennas Propagat.*, vol. 55, no. 6, pp. 1656-1666, 2007.

[13] P. Wang, M. Y. Xia, J. M. Jin, L. Z. Zhou, "Time-domain Integral Equation Solvers using Quadratic B-spline Temporal Basis Functions," *Microwave and Optical Technology Letters*, vol. 49, Issue 5, pp. 1154-1159, May 2007.

[14] M.Y. Xia, G.H. Zhang, G.L. Dai and C. H. Chan, "Stable Solution of Time Domain Integral Equation Methods using Quadratic B-Spline Temporal Basis Functions," *Journal of Computational Mathematics*, vol. 25, no. 3, pp. 374-384, 2007.

[15] M. Ghaffari-Miab, Z. H. Firouzeh, R. Faraji-Dana, R. Moini, S. H. H. Sadeghi, and G. A. E. Vandenbosch, "Time-domain MoM for the Analysis of Thin-wire Structures above Half-space Media using Complex-time Green's Functions and Band-limited Quadratic B-spline Temporal Basis Functions," *Engineering Analysis with Boundary Elements*, vol. 36, pp. 1116-1124, 2012.

[16] M.J. McDonnell, "Box-Filtering Techniques," *Computer Graphics Image Processing*, vol. 17, pp. 65-70, 1981.

[17] A. V. Oppenheim and R.W. Schafer, *Discrete-Time Signal Processing, Third Edition*. Upper Saddle River, NJ: Prentice-Hall Inc., 2009.

Mehrdad Saviz received his B.Sc. from the Iran University of Science and Technology, in 2005 and the M.Sc. degree from the University of Tehran, in 2007, where he is currently a Ph.D. Candidate. His research interests include computational electromagnetics, periodic electromagnetic structures, and numerical microwave dosimetry.

Reza Faraji-Dana received the B.Sc. degree (with honors) from the University of Tehran, Tehran, Iran, in 1986 and the M.Sc. and Ph.D. degrees from the University of Waterloo, Waterloo, ON, Canada, in 1989 and 1993, respectively, all in electrical engineering. He was a Postdoctoral Fellow with the University of Waterloo for one year. In 1994, he joined the School of Electrical and Computer Engineering, University of Tehran, where he is currently a professor.

He has been engaged in several academic and executive responsibilities, among which was his deanship of the faculty of Engineering for more than four years, up until summer 2002, when he was elected as the University President by the university council. He was the President of the University of Tehran until December 2005. He is the author of several technical papers published in reputable international journals and refereed conference proceedings and received the Institution of Electrical Engineers Marconi Premium Award in 1995. He was the Chairman of the IEEE-Iran Section from 2007 until 2009. Prof. Faraji-Dana is an associate member of the Iran Academy of Sciences.

Analytical Solution of Scattering by a 2D Dielectric Filled Crack in a Ground Plane Coated by a Dielectric Layer: TE Case

B. Ghalamkari [1], A Tavakoli [1, 2], and M. Dehmollaian[3]

[1] Department of Electrical Engineering
[2]Institute of Communications Technology and Applied Electromagnetics
Amirkabir University of Technology, Tehran, 15914, Iran
B.Ghalamkari@aut.ac.ir,Tavakoli@aut.ac.ir

[3] Department of Electrical and Computer Engineering
University of Tehran, Tehran, 14395-515, Iran
M.Dehmollaian@ece.ut.ac.ir

Abstract ─ Analytical solution of scattering by a 2D loaded crack on a ground plane, coated by a dielectric layer for TE case is studied theoretically using Kobayashi and Nomura's (Kobayashi Potential) method. The geometry is divided into three regions whose fields are expressed in terms of Bessel eigenfunctions. The problem is reduced to a system of equations involving truncated summations with an infinite number of unknowns. Excitation coefficients are determined by applying the boundary conditions. By applying Weber-Schafheitlin discontinuous integrals, the infinite summations could efficiently be truncated with high numerical accuracy. For validation, in addition to convergence analysis, near-field magnetic current densities on the crack and the radar cross section (RCS) results are compared with those of Finite Element Method (FEM). Having the analytical method, the influence of the filling and the dielectric layer is investigated.

Index Terms - Plane wave scattering, 2D coated crack, dielectric layer, Kobayashi and Nomura method, Weber-Schafheitlin discontinuous integrals.

I. INTRODUCTION

Crack detection is one of the important tasks in nondestructive testing (NDT) of industrial materials and products. Near-field microwave resonator [1] and waveguide techniques [2], [3] have been utilized to detect surface cracks on metals. For non-accessible cracks like those on boilers or blast furnaces, far-field electromagnetic (EM) scattering measurement is recommended [4-18].

The solution of EM scattering by a narrow and arbitrary shaped gap was given by Senior et al. using a point matching method of moment (MoM) [19]. Barkeshli and Volakis have applied the equivalence principal to obtain the equivalent current on the aperture for a quasi static solution [20]. Park et al. formulated the scattering problem for a rectangular crack in a spectral Fourier spectrum domain [21]. Jin used finite element method (FEM) for inside the crack and boundary integral (BI) for field over a perfect electric conductor (PEC) plane [22]. The natural frequency poles extraction with matrix pencil method (MPM) is also given by Deek et al. for detecting cracks in buried pipes [23]. Bozorgi, et al. presented a direct modeling technique based on field integral equation (FIE) for determining the back scattering signatures of a crack in a metallic surface by removing singularities in hypersingular integrals [4, 5]. Honarbakhsh and Tavakoli introduced meshfree collocation method to solve 2D filled cracks in PEC [24]. Other techniques that have been used to solve similar geometries include overlapping T-block method [13-16] transparent boundary condition (TBC) [17] and mode expansion scattering solution for wide rectangular cracks in 2D [25] and cavities in 3D [26].

The Kobayashi potential (KP) method has also been used in various EM scattering problems [6-12]. This method is applicable to all geometrical cracks for TE and TM cases.

Submitted On: June 10, 2012
Accepted On: Aug. 22, 2012

The KP method has some simplifying advantages compared to other numerical techniques (mainly MoM). First, the KP method is accurate and simple in the sense of not dealing with singularity of the Green's functions. Second, since each function involved in the integrand of the potential functions satisfies a part of required boundary conditions, solutions converge rapidly [7].

Sato and Shirai utilized KP method to analyze EM plane wave scattering by a 2D filled rectangular crack on a ground plane without any dielectric coating [9]. They applied the standard impedance boundary condition (SIBC) [10] and estimated the depth of the crack [11]. They also applied KP method to model the propagation through slits array [12].

Since paint, rust, and oil coatings on cracks alter the scattering signature, a solution that takes the dielectric coating effect into consideration is in demand for practical purposes. Here, EM plane wave scattering by a 2D gap in a PEC ground plane coated by a dielectric layer is analyzed. The scattered field is rigorously formulated using the KP method.

The paper is organized as follows. In section II, standing waves in the paint layer are formulated. The KP method is utilized to derive the governing field equations with unknown excitation coefficients in section III. In section IV, the truncated unknown excitation coefficients are computed. The numerical results and validations are presented in section V.

We assumed a time dependence of $e^{-i\omega t}$ throughout the context.

II. THE SCATTERING PROBLEM WITHOUT CRACK

The geometry of a slab of height y_t and relative permittivity of ε_1 and relative permeability of μ_1 on an infinite PEC ground plane is depicted in Fig. 1.

Here, $k_0 = \omega\sqrt{\varepsilon_0\mu_0}$ and $k_1 = k_0\sqrt{\varepsilon_1\mu_1}$ are respectively the free space and the dielectric slab wave numbers. The slab is illuminated by a vertically polarized EM plane wave:

$$\phi^i\left(=H_z^i\right)=e^{-ik_0(x\cos\theta_0+y\sin\theta_0)}, \tag{1}$$

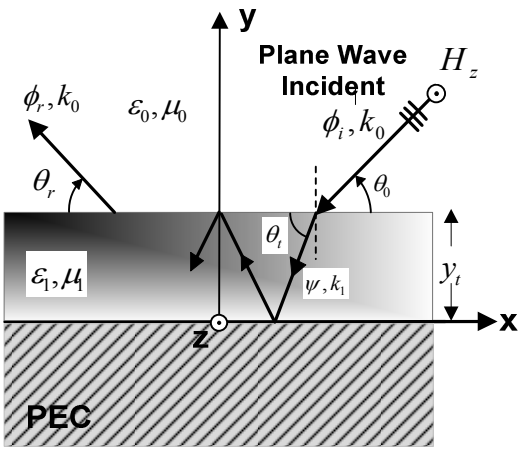

Fig. 1. Geometry of an infinite ground plane coated with a slab.

and the reflected plane wave is:

$$\phi^r\left(=H_z^r\right)=\mathrm{Re}^{-ik_0(x\cos\theta_0-y\sin\theta_0)}, \tag{2}$$

where, R is the reflection coefficient, θ_0 is the incident angle, θ_t is the transmission angle, and θ_r is the reflection angle. Assuming ψ is the total magnetic field in dielectric slab. Thus,

$$\psi=\left[Ae^{-ik_1\sin\theta_t(y-y_t)}+Be^{+ik_1\sin\theta_t y}\right]e^{-ik_1\cos\theta_t x}, \tag{3}$$

Where A and B are unknown coefficients. The first term in (3) represents the down-going and the second term is the up-going wave.

In order to find the aforementioned unknowns first, we note that the tangential field component $E_x=-\frac{1}{i\omega\varepsilon}\frac{\partial\psi}{\partial y}$ is zero over the PEC boundary $(y=0)$ therefore:

$$B=Ae^{ik_1y_t\sin\theta_t}, \tag{4}$$

Second, imposing the continuity of the tangential field components H_z and E_x at $y=y_t$ yields:

$$e^{-ik_0y_t(\sin\theta_0)}+\mathrm{Re}^{ik_0y_t(\sin\theta_0)}=A\left[1+e^{ik_1 2y_t(\sin\theta_t)}\right], \tag{5}$$

$$\left(-\frac{1}{\varepsilon_0}e^{-ik_0y_t(\sin\theta_0)}+\frac{R}{\varepsilon_0}e^{ik_0y_t(\sin\theta_0)}\right)\left(ik_0\sin\theta_0\right)=$$

$$\frac{A}{\varepsilon_0\varepsilon_1}\left(ik_1\sin\theta_t\right)\left[-1+e^{ik_1 2y_t(\sin\theta_t)}\right]. \tag{6}$$

By solving (5) and (6) simultaneously, we get

$$A=\frac{2e^{-ik_0y_t(\sin\theta_0)}}{1+\dfrac{k_1\sin\theta_t}{\varepsilon_1k_0\sin\theta_0}+e^{ik_1 2y_t(\sin\theta_t)}\left[1-\dfrac{k_1\sin\theta_t}{\varepsilon_1k_0\sin\theta_0}\right]}, \quad (7)$$

$$R=\frac{-\dfrac{k_1\sin\theta_t}{\varepsilon_1k_0\sin\theta_0}\left[-1+e^{ik_1 2y_t(\sin\theta_t)}\right]-1-e^{ik_1 2y_t(\sin\theta_t)}}{\dfrac{k_1\sin\theta_t}{\varepsilon_1k_0\sin\theta_0}\left[-1+e^{ik_1 2y_t(\sin\theta_t)}\right]-1-e^{ik_1 2y_t(\sin\theta_t)}} .e^{-ik_0 2y_t(\sin\theta_0)}. \quad (8)$$

Thus, the magnetic field in dielectric slab can be expressed as:

$$\psi=A\left[e^{-ik_1(y-y_t)\sin\theta_t}+e^{+ik_1(y+y_t)\sin\theta_t}\right]e^{-ik_1\cos\theta_t x}. \quad (9)$$

where A is given in (7).

III. THE SCATTERING PROBLEM WITH CRACK

After deriving ψ, a dielectric filled rectangular crack of width $w=2a$ and depth b is assumed in the geometry, as shown in Fig. 2. The crack is assumed to be filled by a material with relative permittivity and permeability of ε_r and μ_r respectively. The filling and coating materials could be both lossy, meaning that $\varepsilon_r,\mu_r,\varepsilon_1$ and μ_1 could be complex.

Three distinctive regions are recognized here:

I) Semi-infinite half space $(y>y_t)$.

II) Slab region $(y_t>y>0)$.

III) Cavity region $(-b\le y<0,|x|<a)$.

We now derive the field representations in each region. The total z-component of the magnetic field and the additional scattering contribution of the crack are denoted by $\phi_i^t(i=1,2,3)$ and $\phi_i^s(i=1,2)$, respectively. Where the subscript i represents the region. In each region, the field is expanded over an appropriate Bessel eigenfunctions. The total fields in regions I and II are

$$\phi_1^t=\phi^i+\phi^r+\phi_1^s, \quad (10)$$

and

$$\phi_2^t=\psi+\phi_2^s. \quad (11)$$

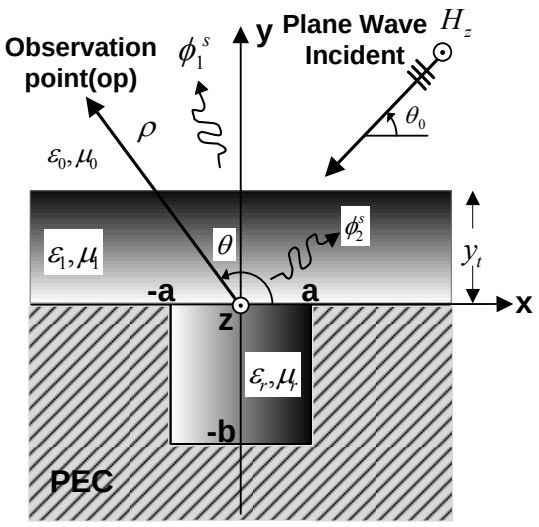

Fig. 2. Geometry of the filled rectangular crack underneath a coating layer in an infinite ground plane.

Additionally, since the scattered fields satisfy the homogeneous Helmholtz equation, utilizing the method of separation of variables, they could be represented as an integral of the general solutions [9]. Thus,

$$\phi_1^s=\frac{1}{a}\int_0^\infty\{d(\xi/a)\cos(\xi u)+e(\xi/a)\sin(\xi u)\}e^{-v\sqrt{\xi^2-\kappa_0^2}}d\xi. \quad (12)$$

and

$$\phi_2^s=\frac{1}{a}\int_0^\infty\{f(\xi/a)\cos(\xi u)+g(\xi/a)\sin(\xi u)\}e^{-v\sqrt{\xi^2-\kappa_1^2}}d\xi + \frac{1}{a}\int_0^\infty\{h(\xi/a)\cos(\xi u)+k(\xi/a)\sin(\xi u)\}e^{(v-t)\sqrt{\xi^2-\kappa_1^2}}d\xi. \quad (13)$$

where $d(.),e(.),f(.),g(.),h(.)$ and $k(.)$ are unknown weighting functions. In (12) and (13) normalized variables and parameters with respect to the half aperture width a are introduced as:

$$u=\frac{x}{a},v=\frac{y}{a},k_0=\frac{\kappa_0}{a},k_1=\frac{\kappa_1}{a},t=\frac{y_t}{a}. \quad (14)$$

It is worth mentioning that ϕ_1^s contains only an up-going wave while the first term of ϕ_2^s is an up-going wave and the second term is a down-going wave. Now, using

$$\begin{cases}\cos(\xi u)=\sqrt{\dfrac{\pi\xi u}{2}}J_{-1/2}(\xi u),\\ \sin(\xi u)=\sqrt{\dfrac{\pi\xi u}{2}}J_{1/2}(\xi u).\end{cases} \tag{15}$$

the weighting functions can be expanded over Bessel functions. Thus,

$$\begin{Bmatrix}d\\f\\h\end{Bmatrix}(\xi/a)=\sum_{m=0}^{\infty}\begin{Bmatrix}D_m\\F_m\\H_m\end{Bmatrix}\frac{J_{2m}(\xi)}{\sqrt{\xi^2-\kappa_0^2}}a, \tag{16}$$

And

$$\begin{Bmatrix}e\\g\\k\end{Bmatrix}(\xi/a)=\sum_{m=0}^{\infty}\begin{Bmatrix}E_m\\G_m\\K_m\end{Bmatrix}\frac{J_{2m+1}(\xi)}{\sqrt{\xi^2-\kappa_0^2}}a. \tag{17}$$

Substituting (15)-(17) into (12) and (13) yields:

$$\phi_1^s=\sqrt{\frac{\pi u}{2}}\sum_{m=0}^{\infty}\int_0^{\infty}\sqrt{\frac{\xi}{\xi^2-\kappa_0^2}}\begin{Bmatrix}D_mJ_{2m}(\xi)J_{-\frac{1}{2}}(\xi u)\\+E_mJ_{2m+1}(\xi)J_{\frac{1}{2}}(\xi u)\end{Bmatrix}.e^{-v\sqrt{\xi^2-\kappa_0^2}}d\xi, \tag{18}$$

$$\phi_2^s=\sqrt{\frac{\pi u}{2}}\sum_{m=0}^{\infty}\int_0^{\infty}\sqrt{\frac{\xi}{\xi^2-\kappa_1^2}}\begin{Bmatrix}F_mJ_{2m}(\xi)J_{-\frac{1}{2}}(\xi u)\\+G_mJ_{2m+1}(\xi)J_{\frac{1}{2}}(\xi u)\end{Bmatrix}e^{-v\sqrt{\xi^2-\kappa_1^2}}d\xi$$
$$+\sqrt{\frac{\pi u}{2}}\sum_{m=0}^{\infty}\int_0^{\infty}\sqrt{\frac{\xi}{\xi^2-\kappa_1^2}}\begin{Bmatrix}H_mJ_{2m}(\xi)J_{-\frac{1}{2}}(\xi u)\\+K_mJ_{2m+1}(\xi)J_{\frac{1}{2}}(\xi u)\end{Bmatrix}e^{(v-t)\sqrt{\xi^2-\kappa_1^2}}d\xi. \tag{19}$$

Each component in the above integral expression is identified as a class of Weber-Schafheitlin type integral that automatically satisfy the zero tangential electric field boundary condition on a part of the ground plane where $|u|>1, v=0$.

The region III is like a parallel plate waveguide. Therefore, the field is expressed by a summation of waveguide modal eigenfunctions. Considering the boundary conditions at $x=\pm a$ and $y=-b$, ϕ_3^t is given by:

$$\phi_3^t=\sum_{n=0}^{\infty}L_n\left\{e^{-ih_nav}+e^{ih_na(v+2b_0)}\right\}\cos\left(\frac{n\pi}{2}(1-u)\right). \tag{20}$$

where $h_n=\sqrt{\varepsilon_r\mu_rk_0^2-(n\pi/w)^2}$ is the propagation constant for n th parallel plate waveguide mode, $b_0=\dfrac{b}{a}$ and L_n is an unknown coefficient.

IV. COMPUTATION OF THE UNKNOWN COEFFICIENTS

To determine the unknown coefficients D_m, E_m, F_m, G_m, H_m and K_m the continuity of the tangential field components $\phi^t(=H_z)$ and E_x at $y=0$ and $y=y_t$ are examined. Therefore,

$$\begin{cases}BC.1: at\ v=t(y=y_t)\ is\ \phi_1^s=\phi_2^s,\\ BC.2: at\ v=t(y=y_t)\ is\ \dfrac{\partial}{\partial v}\phi_1^s=\dfrac{\partial}{\varepsilon_1\partial v}\phi_2^s,\\ BC.3: at\ v=0(y=0)\ is\ \phi_2^t=\phi_3^t,\\ BC.4: at\ v=0(y=0)\ is\ \dfrac{\partial}{\varepsilon_1\partial v}\phi_2^t=\dfrac{\partial}{\varepsilon_r\partial v}\phi_3^t\end{cases} \tag{21}$$

By substituting *BC.1-4* and (15)-(17) in (18) and (19) and after some mathematical manipulation, the following equations are derived:

$BC.1$:

$$\sum_{m=0}^{\infty}\int_0^{\infty}\frac{1}{\sqrt{\xi^2-\kappa_0^2}}\begin{Bmatrix}D_mJ_{2m}(\xi)\cos(\xi u)\\+E_mJ_{2m+1}(\xi)\sin(\xi u)\end{Bmatrix}e^{-t\sqrt{\xi^2-\kappa_0^2}}d\xi$$
$$=\sum_{m=0}^{\infty}\int_0^{\infty}\frac{1}{\sqrt{\xi^2-\kappa_1^2}}\begin{Bmatrix}F_mJ_{2m}(\xi)\cos(\xi u)\\+G_mJ_{2m+1}(\xi)\sin(\xi u)\end{Bmatrix}e^{-t\sqrt{\xi^2-\kappa_1^2}}d\xi$$
$$+\sum_{m=0}^{\infty}\int_0^{\infty}\frac{1}{\sqrt{\xi^2-\kappa_1^2}}\begin{Bmatrix}H_mJ_{2m}(\xi)\cos(\xi u)\\+K_mJ_{2m+1}(\xi)\sin(\xi u)\end{Bmatrix}d\xi. \tag{22}$$

$BC.2$:

$$\varepsilon_1\sum_{m=0}^{\infty}\int_0^{\infty}\begin{Bmatrix}D_mJ_{2m}(\xi)\cos(\xi u)\\+E_mJ_{2m+1}(\xi)\sin(\xi u)\end{Bmatrix}e^{-t\sqrt{\xi^2-\kappa_0^2}}d\xi$$
$$=\sum_{m=0}^{\infty}\int_0^{\infty}\begin{Bmatrix}F_mJ_{2m}(\xi)\cos(\xi u)\\+G_mJ_{2m+1}(\xi)\sin(\xi u)\end{Bmatrix}e^{-t\sqrt{\xi^2-\kappa_1^2}}d\xi \tag{23}$$
$$-\sum_{m=0}^{\infty}\int_0^{\infty}\begin{Bmatrix}H_mJ_{2m}(\xi)\cos(\xi u)\\+K_mJ_{2m+1}(\xi)\sin(\xi u)\end{Bmatrix}d\xi.$$

$BC.3$:

$$\sum_{k=0}^{\infty}(-1)^k\begin{Bmatrix}L_{2k}\gamma_{2k}\cos(k\pi u)\\+L_{2k+1}\gamma_{2k+1}\sin\left(\dfrac{2k+1}{2}\pi u\right)\end{Bmatrix}=A2e^{ik_0y_t\sin\theta_0}e^{-ik_0x\cos\theta_0}$$
$$+\sum_{m=0}^{\infty}\int_0^{\infty}\frac{1}{\sqrt{\xi^2-\kappa_1^2}}\begin{Bmatrix}F_mJ_{2m}(\xi)\cos(\xi u)\\+G_mJ_{2m+1}(\xi)\sin(\xi u)\end{Bmatrix}d\xi$$
$$+\sum_{m=0}^{\infty}\int_0^{\infty}\frac{1}{\sqrt{\xi^2-\kappa_1^2}}\begin{Bmatrix}H_mJ_{2m}(\xi)\cos(\xi u)\\+K_mJ_{2m+1}(\xi)\sin(\xi u)\end{Bmatrix}e^{-t\sqrt{\xi^2-\kappa_1^2}}d\xi. \tag{24}$$

where $\gamma(.)=\left\{1+e^{ih(.)2ab_0}\right\}$.

$BC.4$:

$$\frac{\varepsilon_1}{\varepsilon_r}\sum_{k=0}^{\infty}(-1)^k\left\{\begin{matrix}L_{2k}(ih_{2k}a)\beta_{2k}\cos(k\pi u)\\+L_{2k+1}(ih_{2k+1}a)\beta_{2k+1}\sin\left(\frac{2k+1}{2}\pi u\right)\end{matrix}\right\}=$$

$$-\sum_{m=0}^{\infty}\int_0^{\infty}\left\{\begin{matrix}F_mJ_{2m}(\xi)\cos(\xi u)\\+G_mJ_{2m+1}(\xi)\sin(\xi u)\end{matrix}\right\}d\xi$$

$$+\sum_{m=0}^{\infty}\int_0^{\infty}\left\{\begin{matrix}H_mJ_{2m}(\xi)\cos(\xi u)\\+K_mJ_{2m+1}(\xi)\sin(\xi u)\end{matrix}\right\}e^{-t\sqrt{\xi^2-\kappa_1^2}}d\xi. \quad (25)$$

where $\beta(.)=\left\{-1+e^{ih(.)2ab_0}\right\}$.

These equations are solved by KP and then separated into odd and even groups using even and odd identities [6]. Thus:

$BC.1$: *Even Identity*:

$$\sum_{m=0}^{\infty}D_m\int_0^{\infty}J_{2m}(\xi)J_{2n}(\xi)\frac{e^{-t\sqrt{\xi^2-\kappa_0^2}}}{\sqrt{\xi^2-\kappa_0^2}}d\xi=$$

$$\sum_{m=0}^{\infty}F_m\int_0^{\infty}J_{2m}(\xi)J_{2n}(\xi)\frac{e^{-t\sqrt{\xi^2-\kappa_1^2}}}{\sqrt{\xi^2-\kappa_1^2}}d\xi+\sum_{m=0}^{\infty}H_m\int_0^{\infty}\frac{J_{2m}(\xi)J_{2n}(\xi)}{\sqrt{\xi^2-\kappa_1^2}}d\xi. \quad (26)$$

$BC.1$: *Odd Identity*:

$$\sum_{m=0}^{\infty}E_m\int_0^{\infty}J_{2m+1}(\xi)J_{2n+1}(\xi)\frac{e^{-t\sqrt{\xi^2-\kappa_0^2}}}{\sqrt{\xi^2-\kappa_0^2}}d\xi=$$

$$\sum_{m=0}^{\infty}G_m\int_0^{\infty}J_{2m+1}(\xi)J_{2n+1}(\xi)\frac{e^{-t\sqrt{\xi^2-\kappa_1^2}}}{\sqrt{\xi^2-\kappa_1^2}}d\xi+\sum_{m=0}^{\infty}K_m\int_0^{\infty}\frac{J_{2m+1}(\xi)J_{2n+1}(\xi)}{\sqrt{\xi^2-\kappa_1^2}}d\xi. \quad (27)$$

$BC.2$: *Even Identity*:

$$\varepsilon_1\sum_{m=0}^{\infty}D_m\int_0^{\infty}J_{2m}(\xi)J_{2n}(\xi)e^{-t\sqrt{\xi^2-\kappa_0^2}}d\xi=$$

$$\sum_{m=0}^{\infty}F_m\int_0^{\infty}J_{2m}(\xi)J_{2n}(\xi)e^{-t\sqrt{\xi^2-\kappa_1^2}}d\xi-\sum_{m=0}^{\infty}H_m\int_0^{\infty}J_{2m}(\xi)J_{2n}(\xi)d\xi. \quad (28)$$

$BC.2$: *Odd Identity*:

$$\varepsilon_1\sum_{m=0}^{\infty}E_m\int_0^{\infty}J_{2m+1}(\xi)J_{2n+1}(\xi)e^{-t\sqrt{\xi^2-\kappa_0^2}}d\xi=$$

$$\sum_{m=0}^{\infty}G_m\int_0^{\infty}J_{2m+1}(\xi)J_{2n+1}(\xi)e^{-t\sqrt{\xi^2-\kappa_1^2}}d\xi-\sum_{m=0}^{\infty}K_m\int_0^{\infty}J_{2m+1}(\xi)J_{2n+1}(\xi)d\xi. \quad (29)$$

$BC.3$: *Even Identity*:

$$\sum_{k=0}^{\infty}(-1)^k\left\{L_{2k}\gamma_{2k}J_{2n}(k\pi)\right\}=2Ae^{jk_1y_i\sin\theta_i}J_{2n}(\kappa_0\cos\theta_0)$$

$$+\sum_{m=0}^{\infty}F_m\int_0^{\infty}\frac{J_{2m}(\xi)J_{2n}(\xi)}{\sqrt{\xi^2-\kappa_1^2}}d\xi+\sum_{m=0}^{\infty}H_m\int_0^{\infty}J_{2m}(\xi)J_{2n}(\xi)\frac{e^{-t\sqrt{\xi^2-\kappa_1^2}}}{\sqrt{\xi^2-\kappa_1^2}}d\xi. \quad (30)$$

$BC.3$: *Odd Identity*:

$$\sum_{k=0}^{\infty}(-1)^k\left\{L_{2k+1}\gamma_{2k+1}J_{2n+1}\left(\frac{2k+1}{2}\pi\right)\right\}=-2iAe^{jk_1y_i\sin\theta_i}J_{2n+1}(\kappa_0\cos\theta_0)$$

$$+\sum_{m=0}^{\infty}G_m\int_0^{\infty}\frac{J_{2m+1}(\xi)J_{2n+1}(\xi)}{\sqrt{\xi^2-\kappa_1^2}}d\xi+\sum_{m=0}^{\infty}K_m\int_0^{\infty}J_{2m+1}(\xi)J_{2n+1}(\xi)\frac{e^{-t\sqrt{\xi^2-\kappa_1^2}}}{\sqrt{\xi^2-\kappa_1^2}}d\xi. \quad (31)$$

$BC.4$: *Even Identity*:

$$\frac{\varepsilon_1}{\varepsilon_r}L_{2k}(-1)^k(ih_{2k}a)\beta_{2k}(\delta_{0k}+1)=\pi\sum_{m=0}^{\infty}J_{2m}(k\pi)\left\{\begin{matrix}(-1)F_m\\e^{-t\sqrt{(k\pi)^2-\kappa_1^2}}H_m\end{matrix}\right\}. \quad (32)$$

where δ_{mk} is the Kronecker delta.

$BC.4$: *Odd Identity*:

$$\frac{\varepsilon_1}{\varepsilon_r}L_{2k+1}(-1)^k(ih_{2k+1}a)\beta_{2k+1}=\pi\sum_{m=0}^{\infty}J_{2m+1}\left(\frac{2k+1}{2}\pi\right)\left\{\begin{matrix}(-1)G_m\\e^{-t\sqrt{\left(\frac{2k+1}{2}\pi\right)^2-\kappa_1^2}}K_m\end{matrix}\right\}. \quad (33)$$

Equations (26)-(33) are eight sets of equations to solve eight sets of unknown coefficients D_m, E_m, F_m, G_m, H_m, K_m, L_{2k}, L_{2k+1}.

In a cylindrical coordinate system where the observation point is represented by ρ and θ the far-field scattering is [11]:

$$\phi_1^s=\sqrt{\frac{\pi}{2k_0\rho}}e^{i_1\left(k_0\rho+\pi/4\right)}\sum_{m=0}^{\infty}\left\{\begin{matrix}D_mJ_{2m}\left(k_0a\cos\theta\right)\\-iE_mJ_{2m+1}\left(k_0a\cos\theta\right)\end{matrix}\right\}. \quad (34)$$

The above summations are all convergent and therefore, n and m are limited to N and M, respectively.

V. NUMERICAL RESULTS AND VALIDATION

In this section, the proposed analytical method is applied to several coated cracks and validated by three approaches. First, FEM is used to find $\phi_3^t\left(=H_z^t\right)$ and the magnetic current densities M_x, on the aperture for different incident angles. Second, the RCS is computed by exploiting the coated ground Green's function together with the near to far-field transformation [27]. Third, for rigorous validation of the method, convergence analysis curves are provided [28]. The studied scenarios of the crack cases are listed in Table 1.

A. Validation with magnetic current density analysis

Referring to Fig. 2 and Table 1, in case A only the permittivity of the coating layer is complex whereas in case B all filling and coating materials are complex. The calculated magnetic current density distributions $|M_x|$ on the crack $(|x|<a,\ y=0)$ at various incident angles $(\theta_0=15°, 30°, 45°, 60°, 75°, 90°)$ are shown in Fig.

3 where $N = M = 13$. Comparison of the results with the FEM solution demonstrates the accuracy of the method at all incident angles.

Table 1: Different scenarios of cracks

	w	b	ε_r	μ_r	ε_1	μ_1	y_t
A	$0.2\lambda_0$	$0.2\lambda_0$	1	1	$2+0.1i$	1	$\lambda_0/10$
B	$0.2\lambda_0$	$0.2\lambda_0$	$2.5+0.2i$	$1.8+0.1i$	$2+0.1i$	$1.5+0.2i$	$\lambda_0/10$
C	$1\lambda_0$	$0.2\lambda_0$	$2.5+0.2i$	1	2	1	$\lambda_0/7$
D	$1\lambda_0$	$0.2\lambda_0$	$4+0.2i$	1	3	1	$\lambda_0/7$
E [9]	$2\lambda_0$	$0.5\lambda_0$	$2.5+0.2i$	$1.8+0.1i$	---	---	---
F	$2\lambda_0$	$0.5\lambda_0$	$2.5+0.2i$	$1.8+0.1i$	$3.2+0.1i$	$1.6+0.2i$	$\lambda_0/5$
G [22]	2.5 *cm*	1.25 *cm*	1	1	---	---	---
H	$1.5\lambda_0$	$10\lambda_0$	$2.7+0.03i$	$1.4+0.1i$	---	---	---

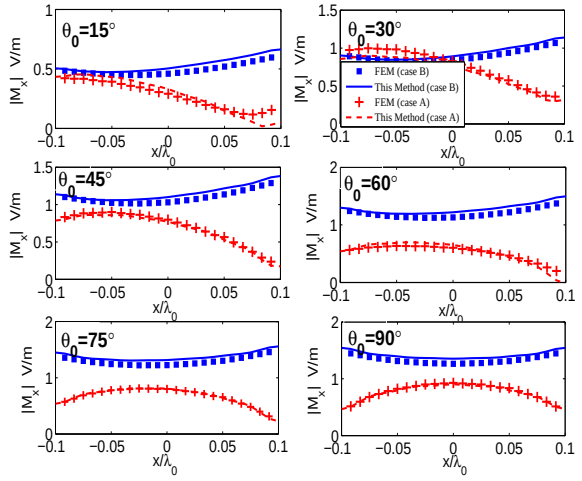

Fig. 3. Magnetic current densities on the crack $(|x| < a,\ y = 0)$ computed by the proposed method and FEM for cases A and B.

B. Validation with RCS analysis

For cases C and D, normalized RCS as a function of incident angle is depicted in Fig. 4. with $N = M = 11$. The results are compared to FEM solution. Here, the width of the crack is $w = 1\lambda_0$ to show the applicability of this method for wide cracks.

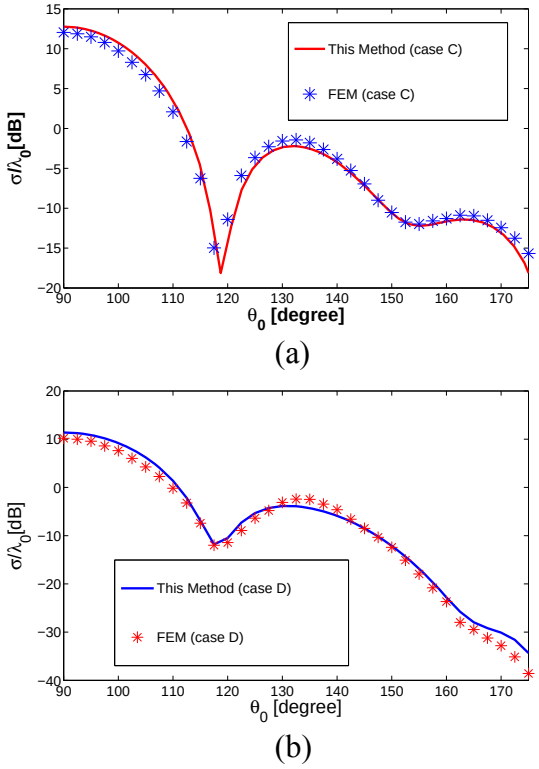

Fig. 4. Normalized RCS as a function of incident angles for (a) case C and (b) case D.

C. Validation with convergence analysis

For error analysis, the convergence curves for cases A, E and F where $\theta_0 = 90^\circ$ are represented in Fig. 5. The error function and Euclidean norm are given by:

$$\begin{cases} e_r = \left\| M^{i+1}_{x_k} - M^{i}_{x_k} \right\| \Big/ \left\| M^{i}_{x_k} \right\|, \ i = 1..N, \\ \left\| M^{i}_{x_k} \right\| = \sqrt{\sum_{k=1}^{K} \left| M^{i}_{x_k} \right|^2}. \end{cases} \quad (34)$$

where x_k is the position of the k th point on the crack and K is the total number of observation points. The results are calculated using $K = 25$ for all three cases.

As mentioned before, Weber-Schafheitlin type integrals automatically satisfy the boundary condition on the PEC $(|x| > a, v = 0)$ and the summations converge very rapidly. Referring to

Fig. 5, for a N close to 12~14, we have the error of $10^{-2.2} = 0.00631$. The rapid convergence of this analytic method makes it desirable for efficient calculation of the scattered field in inverse problems.

D. Results

Here, the reported backscattered results of a crack with the dielectric cover and without the dielectric cover of [9, 22, 24] are compared to the proposed method. In Fig. 6 (a), the normalized RCS of case E (without a coating layer) is compared with that reported in [9]. In addition, by imposing a thin layer on the crack (case F), the influence on the RCS is evident. In addition, our proposed method could also be applied to narrow cracks. Figure 6 (b) shows the normalized RCS of the case H that is a very narrow crack with and without a coating layer. The coating is a $\lambda_0/8$ layer of paint primer ($\varepsilon_1 = 3.48 + 0.12i$). According to Fig. 6, RCS drops down at grazing angles for coated cracks.

Figure 7 shows the normalized RCS as a function of frequency for open crack at a low grazing angle of $\theta_0 = 10^\circ$ (case G). Here, results of finite element boundary integral method (FE-BI) and measurements of [22], meshfree method (MFM) [24] and our method are compared with each other. A good agreement is observed between these methods. Since these solutions do not consider the coating layer, the same case with a 2mm layer of common paint with a relative dielectric constant $\varepsilon_1 = 3 + 0.1i$ [3] is also simulated. Solid line with diamonds in Fig. 7 depicts the results of presented method. Examination of the results shows that the crack dielectric cover alter the RCS signature significantly.

Figures 8 and 9 depict the variation of normalized RCS for various materials of Table 2 for a crack of $w = 0.2\lambda_0$, $b = 0.2\lambda_0$, $\mu_1 = \mu_r = 1$ and $\theta_0 = 90^\circ$. In addition, the cracks in all cases are filled by rust with $\varepsilon_r = 2.7 + 0.03i$.

By increasing the dielectric constant and hence the electrical depth, RCS drops down at first and then increases due to an increase in the electrical thickness of the substrate that excites additional surface wave modes. By increasing the paint depth, the term ψ bounces in slab and its energy decreases. Therefore, RCS reduces as paint depth increases. Additionally, when the coating is lossy, the RCS is significantly affected for even low loss as shown in Fig. 9. Normalized RCS of the crack versus the paint depth for various amount of permeability is shown in Fig. 10. assuming a crack with $w = 0.2\lambda_0$, $b = 0.2\lambda_0$, $\varepsilon_r = 2.7 + 0.03i$ and $\theta_0 = 90^\circ$.

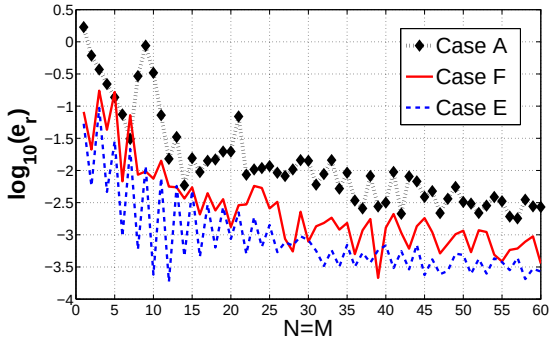

Fig. 5. Convergence curves for cases A, E and F.

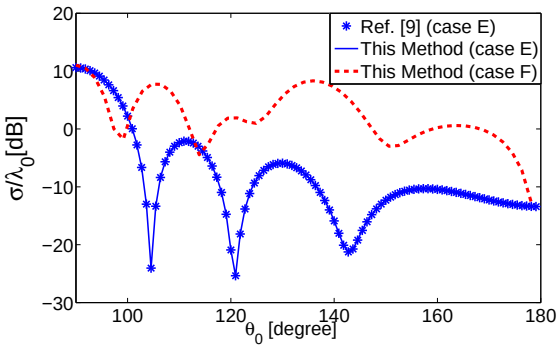

(a)

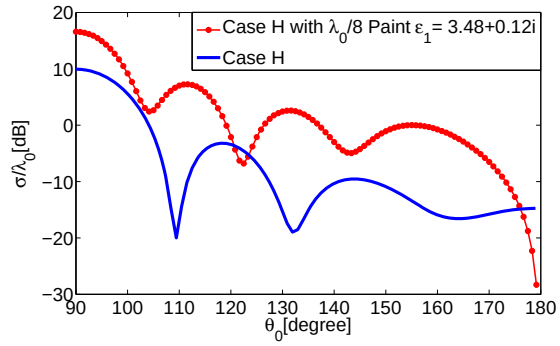

(b)

Fig. 6. Normalized RCS as a function of incident angles for (a) case E[9], and with a dielectric layer of case F (b) case H, and with a $\lambda_0/8$ dielectric layer of $\varepsilon_1 = 3.48 + 0.12i$.

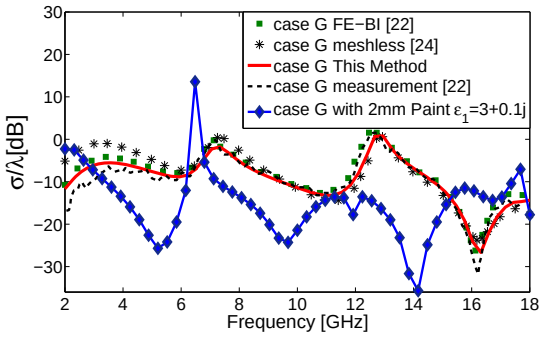

Fig. 7. Normalized RCS as a function of frequency for case G [22, 24] and with a 2mm dielectric layer of $\varepsilon_1 = 3 + 0.1i$ at a low grazing angle of $\theta_0 = 10^\circ$.

Table 2: Some coatings and their complex dielectric constants

Material	ε_r'	ε_r''
Fe_2O_3 Powder (Rust)	2.7	0.03i
Paint Primer	3.48	0.12i
Salt Rust	5.33	1.53i
Red Rust	8.42	1.03i

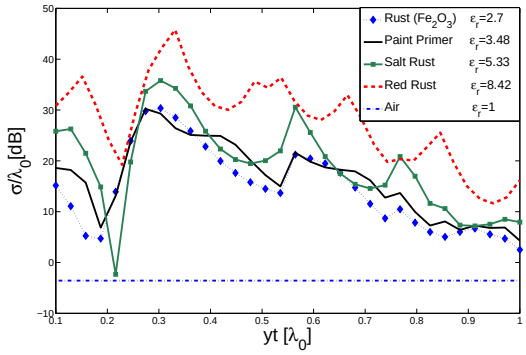

Fig. 8. Normalized RCS of the crack as a function of coating depth for different real dielectric constants where $w = 0.2\lambda_0$, $b = 0.2\lambda_0$, $\mu_1 = \mu_r = 1$, $\varepsilon_r = 2.7 + 0.03\,i$ and $\theta_0 = 90^\circ$.

VI. CONCLUSION

Paint layer on fatigue cracks play an important role in RCS results and thus crack detection as a state of the art in microwave NDT. In this paper, EM plane wave scattering by a 2D rectangular filled and coated crack on a ground plane is analyzed by KP method for TE case. In order to show the validity of the solution, three methods are used. The magnetic current on the aperture and RCS results compared with FEMs'. On the other hand, the approach and its efficiency are validated by convergence analysis. The method is shown to be accurate for both narrow and wide cracks. The proposed method is applicable to all lossy and lossless materials for filled and coated cracks. In addition, the sensitivity of the RCS to the permittivity, permeability and thickness of the overlaying layer is presented.

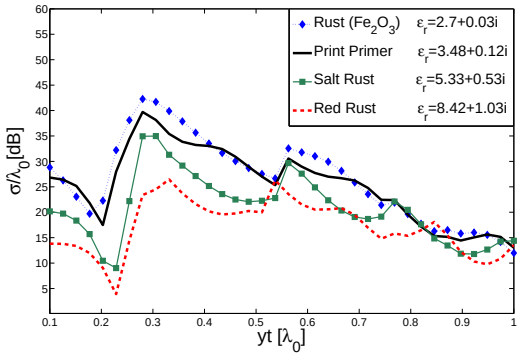

Fig. 9. Normalized RCS of the crack as a function of coating depth for different complex dielectric constants where $w = 0.2\lambda_0$, $b = 0.2\lambda_0$, $\mu_1 = \mu_r = 1$, $\varepsilon_r = 2.7 + 0.03\,i$ and $\theta_0 = 90^\circ$.

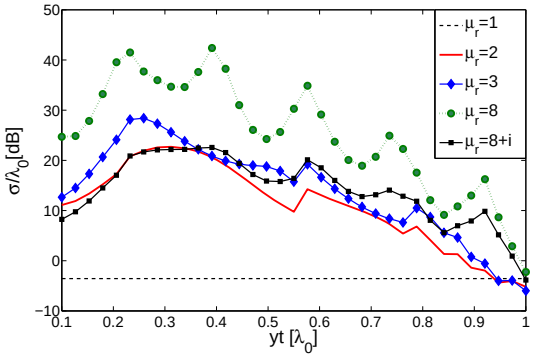

Fig. 10. Normalized RCS of the crack versus paint depth for different permeabilities for $w = 0.2\lambda_0$, $b = 0.2\lambda_0$, $\varepsilon_r = 2.7 + 0.03\,i$ and

ACKNOWLEDGMENT

The authors would like to thank Iran Telecommunication Research Center (ITRC) for supporting this work. The authors also appreciate

Prof. Shirai's of Chuo University for his valuable inputs.

REFERENCES

[1] J. Kerouedan, P. Queffelec, P. Talbot, C. Quendo, and A. L. Brun, "Detecting of Micro-cracks on Metal Surfaces Using Near Field Microwave Dual Behaviour Resonators," *Springer, New Developments and App. in Sen. Tech*, vol. 83, pp. 1-13, 2011.

[2] A. McClanahan, S. Kharkovsky, A. R. Maxon, R. Zoughi, and D. D. Palmer, "Depth Evaluation of Shallow Surface Cracks in Metals Using Rectangular Waveguides at Millimeter-Wave Frequencies," *IEEE Transaction on Instrumentation and Measurement*, vol. 59, no. 6, pp. 1693-1704, June 2010.

[3] N. Qaddoumi, A. Shroyer, and R. Zoughi, "Microwave Detection of Rust under Paint and Composite Laminates," *Taylor and Francis Journal: Research in Nondestructive Evaluation*, vol. 9, no. 4, pp. 201-212, 1997.

[4] M. Bozorgi and A. Tavakoli, "Backscattering From a Two Dimensional Rectangular Crack Using FIE," *IEEE Trans. Antennas Propag.*, vol. 58, no. 2, pp. 552-564, Feb. 2010.

[5] M. Bozorgi and A. Tavakoli, "Plorimetric Scattering From a 3-D Rectangular Crack in a PEC Covered by a Dielectric Layer," *Applied Computational Electromagnetics Society (ACES) Journal*, vol. 26, no. 6, pp. 502-510, June 2011.

[6] Y. Nomura and S. Katsura, "Diffraction of Electromagnetic Waves by Ribbon and Slit. I," *Journal of the physical society of Japan*, vol. 12, pp. 190-200, Feb. 1957.

[7] K. Hongo and Q. A. Naqvi, "Similarities Between Moment Method and Kobayashi Potential," Proceedings of the IEICE General Conference, Kusatsu, Japan, 2001.

[8] K. Hongo and H. Serizawa, "Diffraction of Electromagnetic Plane Wave by a Rectangular Plate and a Rectangular Whole in the Conducting Plate," *IEEE Trans. Antennas Propag.*, vol. 47, no. 6, pp. 1029-1041, June 1999.

[9] R. Sato and H. Shirai, "Electromagnetic Plane Wave Scattering by a Loaded Trough on a Ground Plane," *IEICE Trans. Electron*, vol. E77-C, no. 12, pp. 1983-1989, Dec 1994.

[10] R. Sato and H. Shirai, "EM Scattering Analysis by a Loaded Trough on a Ground Plane using SIBC-E Polarization Case," in *IEEE Antennas and Propagation Society Int. Symp. Digest,* pp. 2858-2861, Aug 1999.

[11] H. Shirai and H. Sekiguchi, "A Simple Crack Depth Estimation Method from Backscattering Response," *IEEE Trans. on Instrumentation and Measurement* vol. 53, no. 4, pp. 1249-1254, Aug 2004.

[12] R. Sato and H. Shirai, "Propagation Analysis for a Simplified Indoor/outdoor Interface Model," in *IEEE Antennas and Propagation Society Int. Symp. Digest, AP-S.*, Nigata, Japan, 2010.

[13] Y. H. Cho, "Transverse Magnetic Plane-wave Scattering Equations for Infinite and Semi-infinite Rectangular Grooves in a Conducting Plane," *IET Microwaves, Antennas & Propagation*, vol. 2, no. 7, pp. 704–710, March 2008.

[14] Y. H. Cho, "TE Scattering from Large Number of Grooves Using Green's Functions and Floquet Modes," in *IEEE Microwave Conference*. Korea-Japan, pp. 41- 44, Nov. 2007.

[15] Y. H. Cho, "TM Plane-Wave Scattering From Finite Rectangular Grooves in a Conducting Plane Using Overlapping T-Block Method," *IEEE Trans. on Antennas and Propagation*, vol. 54, no. 2, pp. 746-749, Feb 2006.

[16] Y. H. Cho, "TM Scattering from Finite Rectangular Grooves in a Conducting Plane using Overlapping T-block Analysis," in *IEEE/ACES Conf. on Wireless Commun. and Applied Computational Electromagnetic*, pp. 744-747, 3-7 April 2005.

[17] K. Du, "Two Transparent Boundary Conditions for the Electromagnetic Scattering from Two-Dimensional Overfilled Cavities," *Elsevier Journal of Computational Physics,* vol. 230, no. 15, pp. 5822–5835, July 2011.

[18] B. Alavikia and O. M. Ramahi, "Fundamental Limitation on the Use of Open-Region Boundary Conditions and Matched Layers to Solve the Problem of Gratings in Metallic Screens," *Applied Computational Electromagnetics Society (ACES) Journal*, vol. 25, no. 8, pp. 652-658, Aug. 2010.

[19] B. A. Senior, K. Sarabandi, and J. R. Natzke, "Scattering by a Narrow Gap," *IEEE Trans. Antennas Propag.*, vol. 38, no. 7, pp. 1102-1111, July 1990.

[20] K. Barkeshli and J. L. Volakis, "Scattering from Narrow Rectangular Filled Grooves " *IEEE Trans. Antennas Propag.*, vol. 39, no. 6, pp. 804-810, June 1991.

[21] T. J. Park, H. J. Eom, and K. Yoshitomi, "An Analysis of Transverse Electric Scattering from a Rectangular Channel in a Conducting Plane," *Radio Science*, vol. 28, no. 5, pp. 663-673, Sept. 1993.

[22] J. Jin, *The Finite Element Method in Electromagnetics*: John Wiley & Sons, 2002.

[23] F. Deek and M. El-Shenawee, "Microwave Detection of Cracks in Buried Pipes Using The Complex Frequency Technique," *Applied*

Computational Electromagnetics Society (ACES) Journal, vol. 25, no. 10, pp. 894-902, Oct. 2010.

[24] B. Honarbakhsh and A. Tavakoli, "Scattering by a 2D Crack: The Meshfree Collocation Approach," *Applied Computational Electromagnetics Society (ACES) Journal*, vol. 27, no. 3, pp. 278 - 284, March 2012.

[25] M. A. Morgan and F. K. Schwering, "Mode Expansion Solution for Scattering by a Material Filled Rectangular Groove," *Progress in Electromagnetics Research (Pier)*, vol. 18, pp. 1-17, 1998.

[26] G. Bao, J. Gao, J .Lin, and W. Zhang, "Mode Matching for the Electromagnetic Scattering From Three-Dimensional Large Cavities," *IEEE Trans. Antennas Propag.*, vol. 60, no. 4, pp. 2004-2010, April 2012.

[27] A. Taflove and S. Hagness, *Computational Electrodynamics: The Finite-Difference Time-Domain Method*, Third ed: Artech House, 2005.

[28] J. C. Rautio, "The Microwave Point of View on Software Validation," *IEEE Antennas Propagat. Mag.*, vol. 38, no. 2, pp. 68-71, April 1996.

Behbod Ghalamkari was born in Tehran, Iran, on December 5, 1981. He received B.Sc. degree in Electrical Engineering from Semnan University of Semnan, Semnan, Iran, in 2005, the M.Sc. degree from the Amirkabir University of Technology (Tehran Polytechnic), Tehran, Iran, in 2007, both in electrical engineering. He is currently working toward the Ph.D. degree in electrical engineering in Amirkabir University of Technology. His main interest lies in the electromagnetic wave propagation, scattering and optimization in electromagnetic problems.

Ahad Tavakoli was born in Tehran, Iran, on March 8, 1959. He received the B.S. and M.S. degrees from the University of Kansas, Lawrence, and the Ph.D. degree from the University of Michigan, Ann Arbor, all in Electrical Engineering, in 1982, 1984, and 1991, respectively.

He is currently a Professor in the Department of Electrical Engineering at Amirkabir University of Technology. His research interests include EMC, scattering of electromagnetic waves and microstrip antennas.

Mojtaba Dehmollaian was born in Iran in 1978. He received the B.S. and M.S. degrees in electrical engineering from the University of Tehran, Tehran, Iran, in 2000 and 2002, respectively. He received the M.S. degree in applied mathematics and Ph.D. degree in electrical engineering from the University of Michigan, Ann Arbor, in 2007.

Currently, he is an Assistant Professor with the Department of Electrical and Computer Engineering, University of Tehran. His research interests are applied electromagnetics, radar remote sensing, and electromagnetic wave propagation, and scattering.

Transform Method for Dielectric Periodic Interface Scattering

L. Li, T. L. Dong, P. Chen*, B. Y. Chen, Q. Huang, L. Lang and Q. X. Li

Department of Electronics and Information
Huazhong University of Science and Technology, Wuhan, 430074, P. R. China
*Corresponding author. chenping1717@163.com

Abstract ─ An extended transform method is developed for calculating the 2-D scattering problem from dielectric periodic interfaces. The method transforms the problem into scattering from two imaginary planes, one of which cuts across the maximum points and another across the minimum points of the periodic interface. The fields just above and below the periodic interface are expanded into Taylor series with respect to the two planes respectively. Then by satisfying boundary condition, the unknown coefficients can be determined. Comparing with T-Matrix and MoM, proposed method is simpler in formulation and less in computational time. Near scattered field distributions above and in the trough region of the periodic interface are calculated by proposed method. The results are in good agreements with those of T-Matrix and MoM respectively.

Index Terms ─ electromagnetic scattering, periodic surface, transform method.

I. INTRODUCTION

Periodic structures frequently appear in the applications such as antenna design, microwave systems, meta-materials etc [1-4] and corresponding problem of electromagnetic waves scattering from periodic surfaces [5-10] is of fundamental importance in science and engineering. Scattering from periodic rough interfaces has been investigated by integral methods such as MoM [6] and T-Matrix [6-8], Because of the slowly convergent integral kernel and the treatment of singularities [6, 11], MoM needs much computational time. While only considering the field points outside the trough region of the corrugation [8] to remove the absolute operation in the periodic Green's function in the spectral domain [6-8] and to speed up the convergence [6], T-Matrix method can not be used to evaluate the fields in the trough region of the corrugation. Those fields may be interested in certain cases [9, 10]. Therefore, more convenient and efficient methods for this kind of problem are always attractive in many applications. Transform method [11] is such a method, but its formulation is only available for perfectly conducting periodic surface scattering.

In this paper, transform method is extended to scattering from dielectric periodic interface. The fields just above and below the periodic interface are expanded into Taylor series with respect to two imaginary planes closest to the interface. By applying the boundary condition that both tangential electric and magnetic fields are continuous on the periodic interface to this form of the scattered and transmitted field, we are able to establish an infinite set of linear equations for the amplitudes of the scattered and the transmitted waves. In section II, the scattering problem is formulated. In Section III, several representative examples are given and compared with T-Matrix. Conclusions are given in Section IV.

II. FORMULATION

The geometry of considered 2-D problem and parameters used in the formulation are shown in Fig. 1. The periodic interface $y=f(x)=f(x+P)$, $x\in[0,P)$, P being period, is illuminated by a z-polarized plane wave with incident angle ϕ_0. The geometrical parameters and the fields do not depend on the z-coordinate. Therefore, the TE and TM problems can be considered independently. The only non-zero component of the total electric fields E_z for TE or that of the total magnetic fields

Submitted On: April 20, 2012
Accepted On: July 22, 2012

H_z for TM mode are denoted by ψ with different script for different regions respectively.

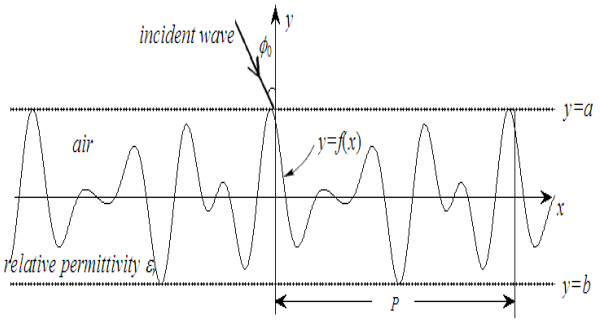

Fig. 1. The geometry of the problem.

Consider two imaginary planes $y=a$ and $y=b$ as shown in Fig. 1, where $a=\max[f(x)]$, $x\in[0,P)$ and $b=\min[f(x)]$, $x\in[0,P)$. These planes are the planes nearest to the rough interface $y=f(x)$ which is sandwiched by them. First, ψ^+, the total field just above the periodic interface and ψ^-, the total field just below the interface, are expanded into Taylor series around planes $y=a$ and $y=b$ respectively [11]

$$\psi^+(x, f(x)) = \sum_{m=0}^{\infty} \frac{1}{m!} \frac{\partial^m \psi}{\partial y^m}|_{y=a} (f(x)-a)^m, \quad (1)$$

$$\psi^-(x, f(x)) = \sum_{m=0}^{\infty} \frac{1}{m!} \frac{\partial^m \psi_1}{\partial y^m}|_{y=b} (f(x)-b)^m, \quad (2)$$

In the mean time, ψ is considered as the summation of incident and scattered field, namely

$$\psi = \psi^i + \psi^s, \quad (3)$$

$$\psi^i = e^{ik(x\sin\phi_0 - y\cos\phi_0)}. \quad (4)$$

As widely accepted [6-9] that the scattered field on and above the top point imaginary plane and the transmitted field on and below the bottom point imaginary plane can be represented by a summation of a discrete set of planar propagating and evanescent harmonics as

$$\psi^s = \sum_{n=-\infty}^{\infty} R_n e^{i\beta_n x} e^{iq_n y}, \quad y \ge a \quad (5)$$

and transmitted field

$$\psi_1 = \sum_{n=-\infty}^{\infty} T_n e^{i\beta_n x} e^{-iq_{1n} y}, \quad y \le b \quad (6)$$

where

$$\beta_n = k\sin\phi_0 + n\frac{2\pi}{P}.$$

and

$$q_n = \begin{cases} (k^2 - \beta_n^2)^{1/2}, & \beta_n^2 \le k^2 \\ i(\beta_n^2 - k^2)^{1/2}, & \beta_n^2 > k^2 \end{cases}.$$

$$q_{1n} = \begin{cases} (k^2\varepsilon_r - \beta_n^2)^{1/2}, & \beta_n^2 \le k^2\varepsilon_r \\ i(\beta_n^2 - k^2\varepsilon_r)^{1/2}, & \beta_n^2 > k^2\varepsilon_r \end{cases}.$$

when $\beta_n^2 \le k^2$ then the harmonic is propagating, otherwise it is evanescent. The assumed time factor $\exp\{-i\omega t\}$ is omitted here and here after. Substituting (4), (5) and (3) into (1) and substituting (6) into (2), it gets that

$$\psi^+(x, f(x)) = \sum_{m=0}^{\infty} \frac{1}{m!} e^{ikx\sin\phi_0} [e^{-ika\cos\phi_0} (-ik\cos\phi_0)^m + \sum_{n=-\infty}^{\infty} R_n (iq_n)^m e^{i(2\pi n/P)x} e^{iq_n a}] (f(x)-a)^m. \quad (7)$$

$$\psi^-(x, f(x)) = \sum_{m=0}^{\infty} \frac{1}{m!} e^{ikx\sin\phi_0} \sum_{n=-\infty}^{\infty} T_n (-iq_{1n})^m e^{-iq_{1n}b} e^{i(2\pi n/P)x} (f(x)-b)^m. \quad (8)$$

The boundary conditions state that the tangential components of electric and magnetic field are continuous across the boundary

$$\psi^+(x, f(x)) = \psi^-(x, f(x)). \quad (9)$$

$$\hat{n}\times(\nabla\times\hat{z}\psi^+(x, f(x))) = c_1\hat{n}\times(\nabla\times\hat{z}\psi^-(x, f(x))). \quad (10)$$

where $c_1=\mu_0/\mu_1=1$ for TE polarization and $c_1=\varepsilon_0/\varepsilon_1$ for TM polarization [8]. Substituting (7) and (8) into (9) and (10), the continuity of tangential electric and magnetic fields on the periodic rough interface gives

$$\sum_{m=0}^{\infty} e^{-ika\cos\phi_0} (-ik\cos\phi_0)^m Z_m(x) + \sum_{n=-\infty}^{\infty} R_n e^{i(2\pi n/P)x} e^{iq_n a} \sum_{m=0}^{\infty} (iq_n)^m Z_m(x) = \sum_{n=-\infty}^{\infty} T_n e^{i(2\pi n/P)x} e^{-iq_{1n}b} \sum_{m=0}^{\infty} (-iq_{1n})^m Z_{1m}(x). \quad (11)$$

$$\sum_{m=0}^{\infty} e^{-ika\cos\phi_0}(-ik\cos\phi_0)^m Z_m(x)(f'(x)k\sin\phi_0 +k\cos\phi_0)+\sum_{n=-\infty}^{\infty} R_n e^{i(2\pi n/P)x}e^{iq_n a}\sum_{m=0}^{\infty}(iq_n)^m Z_m(x)(f'(x)\beta_n - q_n) = c_1\sum_{n=-\infty}^{\infty} T_n e^{i(2\pi n/P)x}e^{-iq_{1n}b}\sum_{m=0}^{\infty}(-iq_{1n})^m Z_{1m}(x)(f'(x)\beta_n + q_{1n}). \quad (12)$$

in which two periodic function sequences denote that

$$Z_m(x) = Z_m(x+P) = \frac{1}{m!}(f(x)-a)^m, \quad m = 0,1,2\ldots \quad (13)$$

$$Z_{1m}(x) = Z_{1m}(x+P) = \frac{1}{m!}(f(x)-b)^m, \quad m = 0,1,2\ldots \quad (14)$$

Both (11) and (12) are periodic function of x so domain [0,P] can be discretized into L intervals each with width P/L. The center of p-th interval is denoted by $x=x_p$. Point matching the two identities at $x=x_p$, p=1,2,…L and truncating terms in Taylor series to M and reducing the other infinite summation from -N to N, (11) and (12) can be written in the matrix-vector form as

$$F + C\cdot R = D\cdot T, \quad (15)$$

$$Fh + Ch\cdot R = Dh\cdot T, \quad (16)$$

in which unknown coefficient vectors

$$R = [R_{-N}\cdots R_{-1}R_0R_1\cdots R_N]^T. \quad (17)$$

$$T = [T_{-N}\cdots T_{-1}T_0T_1\cdots T_N]^T. \quad (18)$$

C, D, Ch and Dh are matrices, F and Fh are column vectors and their elements with respect to element index are given by,

$$C_{pn} = e^{i(2\pi n/P)x_p}e^{iq_n a}\sum_{m=0}^{M}(iq_n)^m Z_m(x_p). \quad (19)$$

$$D_{pn} = e^{i(2\pi n/P)x_p}e^{-iq_{1n}b}\sum_{m=0}^{M}(-iq_{1n})^m Z_{1m}(x_p). \quad (20)$$

$$Ch_{pn} = e^{i(2\pi n/P)x_p}e^{iq_n a}\sum_{m=0}^{M}(iq_n)^m Z_m(x_p)(f'(x_p)\beta_n - q_n). \quad (21)$$

$$Dh_{pn} = c_1 e^{i(2\pi n/P)x_p}e^{-iq_{1n}b}\sum_{m=0}^{M}(-iq_{1n})^m Z_{1m}(x_p)(f'(x_p)\beta_n + q_{1n}). \quad (22)$$

$$F_p = \sum_{m=0}^{M} e^{-ika\cos\phi_0}(-ik\cos\phi_0)^m Z_m(x_p). \quad (23)$$

$$Fh_p = \sum_{m=0}^{M} e^{-ika\cos\phi_0}(-ik\cos\phi_0)^m Z_m(x_p)(f'(x_p)k\sin\phi_0 + k\cos\phi_0). \quad (24)$$

(15) and (16) are linear system of equations and can be solved straightforwardly. Then substituting R into (5), scattered field on and above the top point of the surface can be calculated. In the trough region of the corrugation the scattered field can be calculated by

$$\psi^s(x,y) = \sum_{m=0}^{\infty}\frac{1}{m!}\frac{\partial^m\psi^s}{\partial y^m}|_{y=a}(y-a)^m,\ f(x)\le y < a \quad (25)$$

Also reducing the harmonic summation from -N to N and truncating terms in Taylor series to M, the scattered field is expressed as

$$\psi^s(x,y) = \sum_{n=-N}^{N} R_n e^{i\beta_n x}e^{iq_n a}\sum_{m=0}^{M}\frac{1}{m!}(iq_n)^m(y-a)^m,\ f(x)\le y < a \quad (26)$$

III. NUMERICAL RESULTS

A. Diffracted efficiency

The proposed method is applied to the silver grating described in paper [8]. The grating is made of silver with 830 lines/mm and a sinusoidal profile $f(x)=-h\cos(2\pi x/P)$, P=1205nm, h=100nm. The relative complex permittivity of the silver is −7.29135+i0.294387, the incident wavelength is 482nm. Sum all the propagating powers in the air, the diffracted efficiency is given by

$$P_r = \sum\frac{|R_n|^2 q_n}{k\cos\phi_0}. \quad (27)$$

The sum of the diffracted energy for TM polarization is a severe test of the method since anomaly is generally observed and a significant fraction of the incident light does not reappear in the diffracted orders. The obtained results are shown in Fig. 2 and compared with those by T-Matrix. We can see from the figure that the efficiency curves of the two methods are matched well. Calculation times of proposed and T-Matrix

method for this example are 206.3 s and 1797.8 s, respectively under the same soft and hardware conditions.

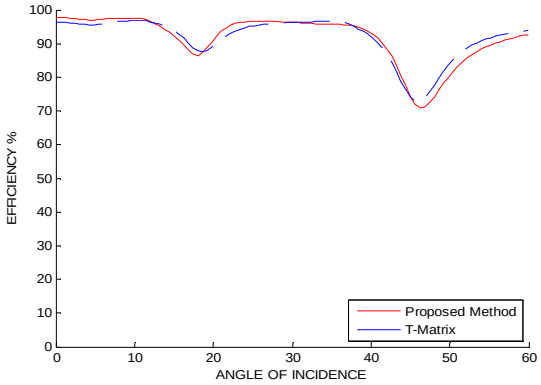

Fig. 2. Diffracted efficiency of the silver grating for TM polarized waves.

B. Scattered field

Proposed method is applied to two representative interfaces for TE polarization, one is sinusoidal $f(x)=0.5\sin(\pi x/2)$ and the other is triangle $f(x)=0.5|x-2|-0.5$. The obtained results are also compared with T-Matrix results. The illuminating plane wave is of frequency 300 MHz, and the relative permittivity of the substrate is 2.25, period P=4 m and the near scattered fields are calculated on y_0=3 m plane within one period. Incident angles are chosen as 45° for sinusoidal and 60 ° for triangle interface. Number of harmonics, terms in Taylor series and point matching number of transformed problem for calculation in (15) and (16) are chosen as N=12, M=20, L=80 respectively. The parameter N is so selected that all the propagating harmonics and part of evanescent harmonics are included for the given truncation errors of (5) (6). The selection of M is related to truncation errors of Taylor series. We choose the biggest M for given accuracy remainder term of equations (19)-(24). As the corrugation depth increases, more harmonics and more Taylor series terms need to be taken into account. Real and Imaginary parts of scattered field are depicted in Figs. 3 and 4, respectively. As seen from figures, results of proposed and T-Matrix method are in satisfactory agreement. Calculation times of the first and second example for proposed method are 5.312 s and 5.469 s, those for T-Matrix method are 47.125s and 47.687 s, respectively.

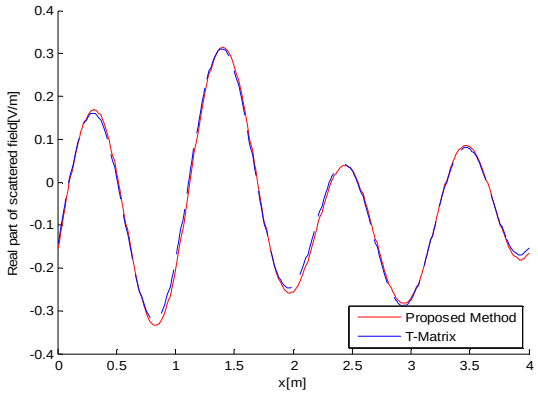

(a)

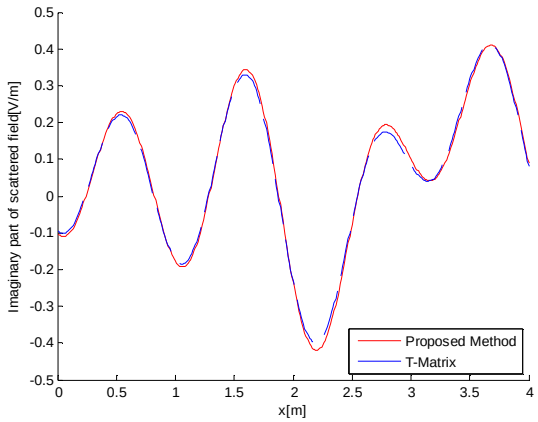

(b)

Fig. 3. Scattered field above sinusoidal interface within one period (a) Real part, (b) Imaginary part.

Then the scattered field within the groove of the first example are calculated on y_0=0 m , $x\in(P/2, P)$. The parameters are the same as the first example. Since the T-Matrix can not calculate the scattered field in the trough region of corrugation, the results of proposed method are compared with MoM [6]. Real and Imaginary parts of the scattered field are depicted in Fig. 5. Calculation times of this example for proposed and MoM are 3.844s and 541.391s respectively. Numerical results show good agreements.

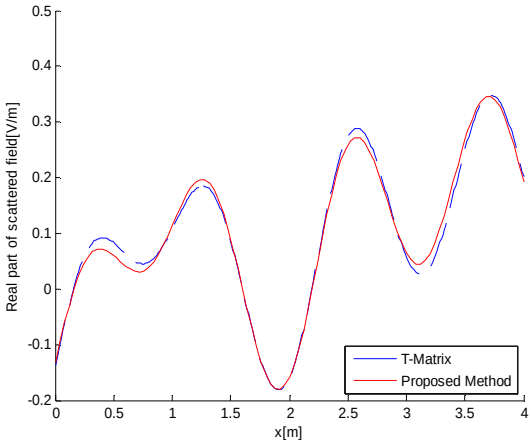

(a)

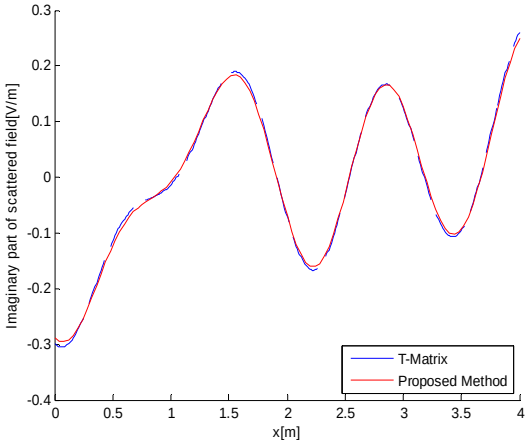

(b)

Fig. 4. Scattered field above triangle interface within one period (a) Real part, (b) Imaginary part.

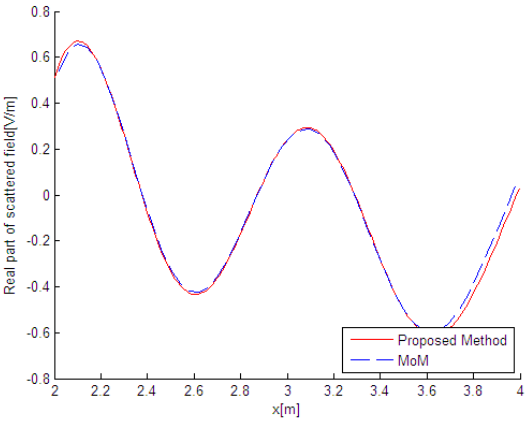

(a)

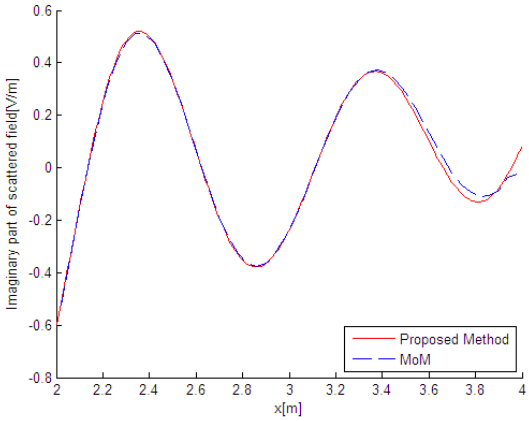

(b)

Fig. 5. Scattered field in the trough region of sinusoidal interface (a) Real part, (b) Imaginary part.

IV. DISCUSSION AND CONCLUSION

The scattering problem from periodic interface is transformed to scattering from two imaginary planes, and then the fields just above and below the rough interface are represented by Taylor expansions at the two planes respectively. Applying the boundary conditions to these fields the scattering problem is solved. Comparing with T-Matrix, the proposed method is of simple formulation and it can calculate the field in the trough region of the corrugation. Obtained numerical results of near field distribution are in good agreements with T-Matrix or MoM and the proposed method is with much higher computation efficiency. Besides, for some particular conditions (such as f=300 MHz, ε_r=2.25, P=4 and ϕ_0=30º), one of the y-components of propagation constants becomes zero, T-Matrix cannot work because its formulation has a factor $(q_n)^{-1/2}$ [7] while proposed method does not have this difficulty. Compare with MoM which is based on the slowly convergent periodic Green's function, the proposed method is much more efficient in the calculation of the field within the grooves.

It is the limitation of proposed method that the matrices C, D, Ch and Dh may become ill-conditioned when the surface corrugation is deep.

ACKNOWLEDGMENT

The research is supported in part by 40971185, 41001195 and 41176156 NSFC, P. R.

China, and by No. 2010AA122200 from the National High Technology Research and Development Program of China (863 Program).

REFERENCES

[1] H. C. Chu, S. K. Jeng and H. C. Chen, "Reflection and Transmission Characteristics of Lossy Periodic Composite Structures," *IEEE Trans. Antennas Propagat*., vol. AP-44, pp. 580-587, 1996

[2] A. Ishimaru, *Electromagnetic Wave Propagation, Radiation and Scattering*, Prentice-Hall, New Jersey, 1991.

[3] A. B. Ali, E. A. Hajlaoui, A. Gharsallah, "Efficient Analysis Technique for Modeling Periodic Structures based on Finite Element Method using High-order Multiscalets Functions," *Applied Computational Electromagnetics Society* (*ACES*) *Journal*, vol. 25, no. 9, pp. 755-763, Sep. 2010

[4] A. Cucini, S. Maci, "Macro-scale Basis Functions for the Method of Moment Analysis of Large Periodic Microstrip Arrays," *Applied Computational Electromagnetics Society* (*ACES*) *Journal*, vol. 21, no. 3, pp. 256-266, Nov. 2006.

[5] T. Arebs, S. N. Chandler-Wilde and J. A. DeSanto, "On Integral Equation and Least Squares Method for Scattering by Diffraction Grating," *Computer Physics Communication*, vol. 1, no. 6, pp. 1010-1042, Dec. 2006

[6] L. Tsang, J. A. Kong, K. H. Ding and C. O. Ao, *Scattering of electromagnetic waves: Numerical simulations*, Wiley, New York, 2001.

[7] J. A. Kong, *Electromagnetic wave theory*, Wiley, 1986

[8] S. L. Chuang and J. A. Kong, "Scattering of Waves from Periodic Surfaces", *Proceedings of the IEEE*, vol. 69, no. 9, pp. 1132-1143, Sep. 1981.

[9] J. Wauer and T. Rother, "Considerations to Rayleigh's Hypothesis", *Optics Communications*, vol. AP-282, pp. 339-350, 2009

[10] M. Ohtsu, Y. Okuno, A. Matsushima and T.Suyama, "A Combination of Up- and Down-Going Floquet Model Functions used to Describe the Field Inside Grooves of a Deep Grating", *Progress in Electromagnetics Research* (*PIER*), vol. 64, pp. 293-316, 2006

[11] N. S. Tezel, "Electromagnetic Scattering from Perfectly Conducting Periodic Surfaces by Transforming into Equivalent Boundary Condition," *Microwave and Optical Technology Letters*，vol. 50, no. 8, pp. 1997-2000, Aug. 2008.

Lin Li received the B. Sc. degrees in Electronic Information Engineering from Xi'an Institute of Posts and Telecommunications, Xi'an, in 2008. She is currently in her Ph. D. program of Electromagnetic field and microwave technology in Huazhong University of Science and Technology (HUST), Wuhan, China. Her research interests include periodic structure and electromagnetic scattering.

Tian-lin Dong received M.Sc. and Ph.D. degrees from the Polytechnic University of New York, New York, in 1982 and 1985, respectively. He is currently a faculty member in Department of Electronics and Information, HUST. His research interests include electromagnetic theory and its microwave and RF applications.

Ping Chen received the Ph.D. degree in and joined HUST in 2002. She is currently an Associate Professor in the Department of electronics and information. Her research interests are periodic structure, rough surface scattering and microwave remote sensing.

New Alternating Direction Implicit Finite-Difference Time-Domain Method with Higher Efficiency

Juan Chen
Key Laboratory for Physical Electronics and Devices of the Ministry of Education,
Xi'an Jiaotong University, Xi'an 710049, China
chenjuan0306@yahoo.com.cn

Abstract ― This letter presents a new unconditionally stable three-dimensional alternating direction implicit finite-difference time-domain (ADI-FDTD) method. The implicit differences of the method along different directions are irrelevant to each other, which results in a new updating equation with much simpler and more concise right-hand sides. This leads to substantial reduction in the number of arithmetic operations required for their computations. The unconditional stability of the proposed method is presented analytically, and the numerical performance of the method over the conventional ADI-FDTD method is demonstrated through numerical example.

Index Terms - ADI-FDTD scheme, CFL condition, implicit difference, unconditional stability

I. INTRODUCTION

To overcome the Courant limit on the time step size of the finite-difference time-domain (FDTD) method, unconditionally stable methods such as the alternating-direction implicit (ADI) FDTD scheme have been studied extensively [1-8]. This method has been demonstrated to be useful for the problems where fine scale structures are involved. However, from the implementation point of view, the ADI-FDTD algorithm is rather complicated. This is because not only there are tridiagonal systems that need to be dealt with, but the right-hand sides of their updating equations also contain numerous terms that call for considerable arithmetic operations.

In this letter, a new unconditionally stable three-dimensional ADI-FDTD method is presented. The implicit differences of the method along different directions are irrelevant to each other, which results in a new updating equation. In this method, four time steps (n, n+1/3, n+2/3 and n+1) are used for defining the field components and three sub-iterations are required for field advancement from n to n+1. It must solve six tridiagonal matrices and six explicit updates for one full update cycle, which is same as the conventional ADI-FDTD method. However, for that the new algorithm is with updating equations whose right-hand sides are much simpler and more concise than those in the conventional implementation, the number of arithmetic operations required is reduced substantially. Thus, the new ADI-FDTD method is with higher computational efficiency than the conventional one. The formulations of the new ADI-FDTD method are given, and the unconditional stability of the method is presented analytically. The numerical performance of the new method over the conventional ADI-FDTD method is demonstrated through numerical example.

II. FORMULATION

In the new ADI-FDTD method, the calculation for one discrete time step is performed using three procedures. The electromagnetic field components are arranged on the Yee's cells in the same way as that using the conventional FDTD method. The numerical formulations of the new ADI-FDTD method for a full three-dimensional wave are presented in (1)-(3).

A) First procedure from n to $n+1/3$

$$E_x^{n+1/3} = E_x^n - a D_z \left(H_y^n + H_y^{n+1/3} \right) \quad (1.1)$$

$$H_y^{n+1/3} = H_y^n - b D_z \left(E_x^n + E_x^{n+1/3} \right) \quad (1.2)$$

$$E_y^{n+1/3} = E_y^n + a D_z \left(H_x^n + H_x^{n+1/3} \right) \quad (1.3)$$

$$H_x^{n+1/3} = H_x^n + b D_z \left(E_y^n + E_y^{n+1/3} \right) \quad (1.4)$$

$$E_z^{n+1/3} = E_z^n \quad (1.5)$$

$$H_z^{n+1/3} = H_z^n \quad (1.6)$$

Submitted On: July 10, 2012
Accepted On: October 1, 2012

B).Second procedure from $n+1/3$ *to* $n+2/3$

$$E_y^{n+2/3} = E_y^{n+1/3} - a D_x \left(H_z^{n+1/3} + H_z^{n+2/3} \right) \quad (2.1)$$

$$H_z^{n+2/3} = H_z^{n+1/3} - b D_x \left(E_y^{n+1/3} + E_y^{n+2/3} \right) \quad (2.2)$$

$$E_z^{n+2/3} = E_z^{n+1/3} + a D_x \left(H_y^{n+1/3} + H_y^{n+2/3} \right) \quad (2.3)$$

$$H_y^{n+2/3} = H_y^{n+1/3} + b D_x \left(E_z^{n+1/3} + E_z^{n+2/3} \right) \quad (2.4)$$

$$E_x^{n+2/3} = E_x^{n+1/3} \quad (2.5)$$

$$H_x^{n+2/3} = H_x^{n+1/3} \quad (2.6)$$

C).Third procedure from $n+2/3$ *to* $n+1$

$$E_z^{n+1} = E_z^{n+2/3} - a D_y \left(H_x^{n+1} + H_x^{n+2/3} \right) \quad (3.1)$$

$$H_x^{n+1} = H_x^{n+2/3} - b D_y \left(E_z^{n+1} + E_z^{n+2/3} \right) \quad (3.2)$$

$$E_x^{n+1} = E_x^{n+2/3} + a D_y \left(H_z^{n+1} + H_z^{n+2/3} \right) \quad (3.3)$$

$$H_z^{n+1} = H_z^{n+2/3} + b D_y \left(E_x^{n+1} + E_x^{n+2/3} \right) \quad (3.4)$$

$$E_y^{n+1} = E_y^{n+2/3} \quad (3.5)$$

$$H_y^{n+1} = H_y^{n+2/3} \quad (3.6)$$

where, $a = \Delta t/2\varepsilon$, $b = \Delta t/2\mu$; $D_w = \partial/\partial w$ ($w = x, y, z$) represents the first derivative with respect to w; n and Δt are the index and size of time-step; ε and μ are the permittivity and permeability of the surrounding media, respectively.

It can be seen from eqs. (1.1)-(1.6) that, only the implicit difference along the z-directions is applied in the first procedure.. Updating of $E_x^{n+1/3}$ component, as shown in eq. (1.1), needs the unknown $H_y^{n+1/3}$ component at the same time; thus the $E_x^{n+1/3}$ component has to be updated implicitly. Substituting eq. (1.2) into eq. (1.1), the equation for $E_x^{n+1/3}$ field is given as,

$$\begin{aligned} &(1 + 2S_1) E_x^{n+1/3}(i + 1/2, j, k) \\ &-S_1 \begin{bmatrix} E_x^{n+1/3}(i + 1/2, j, k - 1) \\ +E_x^{n+1/3}(i + 1/2, j, k + 1) \end{bmatrix} \\ &= (1 - 2S_1) E_x^{n}(i + 1/2, j, k) \\ &+S_1 \begin{bmatrix} E_x^{n}(i + 1/2, j, k - 1) \\ +E_x^{n}(i + 1/2, j, k + 1) \end{bmatrix} \\ &-S_2 \begin{bmatrix} H_y^{n}(i + 1/2, j, k + 1/2) \\ -H_y^{n}(i + 1/2, j, k - 1/2) \end{bmatrix} \end{aligned} \quad (4)$$

with, $S_1 = \Delta t^2/(4\varepsilon\mu\Delta z^2)$, $S_2 = \Delta t/(\varepsilon\Delta z)$.

The updating equation for the electronic field component $E_y^{n+1/3}$ can be written down similarly as eq.(4), then, the magnetic field components $H_y^{n+1/3}$ and $H_x^{n+1/3}$ are explicitly updated straightforward.

In the second and third procedure, the implicit difference along the x and y directions are applied respectively. The flow chart of the new ADI-FDTD method is shown in Fig. 1. It is obvious that, the implicit differences of proposed method along different directions are irrelevant to each other. Thus, at each time step, the new ADI-FDTD method requires the solution of six tridiagonal

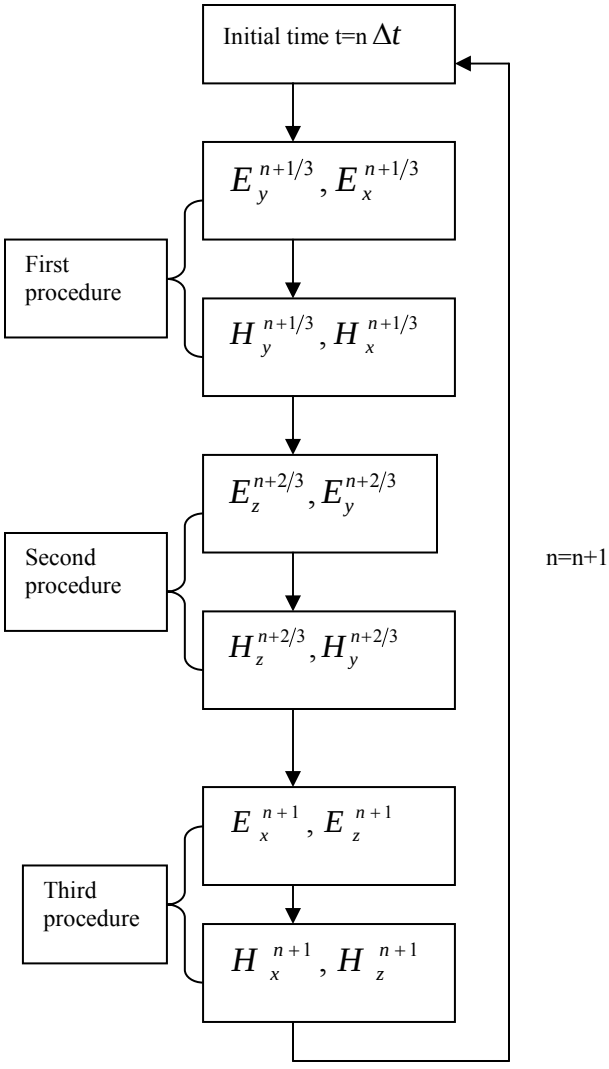

Fig. 1. The flow chart of the new ADI-FDTD method.

matrices and six explicit updates, which is same as the conventional ADI-FDTD method. However, the right side of the updating equation of the new ADI-FDTD method takes much simpler and more concise form compared to the conventional one.

Table 1: Flops count for 3-D ADI-FDTD algorithms

Scheme	Algorithm	Implicit	Explicit	Total
ADI-FDTD	M/D	18	12	102
	A/S	48	24	
New ADI-FDTD	M/D	18	6	72
	A/S	24	24	

To clarify this point further, we recall the updating equation of the conventional ADI-FDTD method. The implicit updating for the E_x component of the conventional ADI-FDTD method is as follows,

$$\begin{aligned}
&(1+2S_1)E_x^{n+1/2}(i+1/2,j,k)\\
&-S_1\begin{bmatrix}E_x^{n+1/2}(i+1/2,j,k-1)\\+E_x^{n+1/2}(i+1/2,j,k+1)\end{bmatrix}\\
&=E_x^{n}(i+1/2,j,k)\\
&-S_3\begin{bmatrix}E_z^{n}(i+1,j,k+1/2)-E_z^{n}(i,j,k+1/2)\\-E_z^{n}(i+1,j,k-1/2)+E_z^{n}(i,j,k-1/2)\end{bmatrix}\\
&+S_4\begin{bmatrix}H_z^{n}(i+1/2,j+1/2,k)\\-H_z^{n}(i+1/2,j-1/2,k)\end{bmatrix}\\
&-S_5\begin{bmatrix}H_y^{n}(i+1/2,j,k+1/2)\\-H_y^{n}(i+1/2,j,k-1/2)\end{bmatrix}
\end{aligned} \tag{5}$$

$S_3 = \Delta t^2/(4\varepsilon\mu\Delta x\Delta z)$, $S_4 = \Delta t/(2\varepsilon\Delta y)$, $S_5 = \Delta t/(2\varepsilon\Delta z)$

To verify the new algorithm, it is desirable to provide detailed assessment and comparison with regard to the computation efficiency of these two methods. The floating point operations (flops) counts taking into account the number of multiplications/divisions (M/D) and additions/subtractions (A/S) required for one complete time step for both conventional and present algorithms are listed in Table 1, based on the right-hand sides of their respective updating equations such as (4) and (5), etc. For simplicity, the number of electric and magnetic field components in all directions has been taken to be the same and assume that all multiplicative factors have been precomputed and stored. From the table, it is clear that the total flops count (M/D +A/S) has been reduced substantially from 102 to 72 in the present implementation. This corresponds to an efficiency gain of 1.42 in flops count reduction for the right-hand sides of updating equations.

III. STABILITY

In this section, the unconditional stability of the new ADI-FDTD method is derived by following a similar procedure described in [9].

The relations between the field components of eq.(1) in the new ADI-FDTD method can be represented in matrix form as,

$$[A]U^{n+1/3} = [B]U^{n} \tag{6}$$

with,

$$[A] = \begin{bmatrix}
1 & 0 & 0 & 0 & aD_z & 0\\
0 & 1 & 0 & -aD_z & 0 & 0\\
0 & 0 & 1 & 0 & 0 & 0\\
0 & -bD_z & 0 & 1 & 0 & 0\\
bD_z & 0 & 0 & 0 & 1 & 0\\
0 & 0 & 0 & 0 & 0 & 1
\end{bmatrix}$$

$$[B] = \begin{bmatrix}
1 & 0 & 0 & 0 & -aD_z & 0\\
0 & 1 & 0 & aD_z & 0 & 0\\
0 & 0 & 1 & 0 & 0 & 0\\
0 & bD_z & 0 & 1 & 0 & 0\\
-bD_z & 0 & 0 & 0 & 1 & 0\\
0 & 0 & 0 & 0 & 0 & 1
\end{bmatrix}$$

For simplicity, we define,

$$\begin{aligned}
U^{n+1} &= \zeta_y U^{n+\frac{2}{3}} = \zeta_y\left[\zeta_x U^{n+\frac{1}{3}}\right]\\
&= \zeta_y\left[\zeta_x\left(\zeta_z U^{n}\right)\right] = \zeta U^{n}
\end{aligned} \tag{7}$$

here, ζ_x, ζ_y and ζ_z denote the growth factor along the x, y and z directions respectively; ζ is the total growth factor from the time step n to $n+1$. In such a case, we have,

$$\left([A]\zeta_z - [B]\right)U^{n} = 0 \tag{8}$$

For a nontrivial solution of eq. (8), the determinant of the coefficient matrix in eq. (8) should be zero, namely,

$$\left|[A]\zeta_z - [B]\right| = 0 \qquad (9)$$

By solving eq. (9), the growth factor ξ_z is obtained:

$$\zeta_{z\,1,2} = 1 \qquad (10)$$

$$\zeta_{z\,3,4} = \zeta_{z\,5,6} = \frac{1 + ab D_z^2 \pm \sqrt{4ab D_z^2}}{1 - ab D_z^2} \qquad (11)$$

Approximating each derivative in space by centered second-order finite differences, it obtains [9],

$$D_z = \frac{2\hat{j}\sin\left(\frac{k_z \Delta z}{2}\right)}{\Delta z} \qquad (12)$$

Then, we have,

$$\left|\zeta_z\right| = 1 \qquad (13)$$

With same manipulation, we can get,

$$\left|\zeta_x\right| = \left|\zeta_y\right| = 1 \qquad (14)$$

Thus, equation $\left|\zeta\right| = \left|\zeta_y\right|\left|\zeta_x\right|\left|\zeta_z\right| = 1$ is unconditionally satisfied. It means that the new ADI-FDTD scheme is unconditionally stable.

IV. NUMERICAL VALIDATION

To demonstrate the computational efficiency of the proposed ADI-FDTD method, a simple numerical example is presented here. An air-filled cavity with dimensions $50\text{cm} \times 50\text{cm} \times 50\text{cm}$, is excited by a current source J_z with Gaussian pulse waveform $\left[\exp\left(-4\pi(t-t_0)^2/t_1^2\right)\right]$, $t_0 = t_1 = 1ns$. The cell size is chosen as $\Delta x = \Delta y = \Delta z = 1\text{cm}$, so that the computational domain is $50 \times 50 \times 50$ cells. The source and observation point is set at the cells (5,5,5) and (45,45,45), respectively. Figure 2 plots the time-domain E_z component recorded at the observation point. The simulations have been carried out using Yee's FDTD method, conventional ADI-FDTD method and new ADI-FDTD method, with same time-step size $\Delta t_{CFL} = 19.2\text{ps}$, which is the maximum time-step size to satisfy the stability condition of the FDTD algorithm. It can be seen from this figure that, both the result of the conventional ADI-FDTD method and the new ADI-FDTD method agree well with that of the FDTD method, which demonstrates that the new ADI-FDTD method is with same accuracy as that of the conventional one.

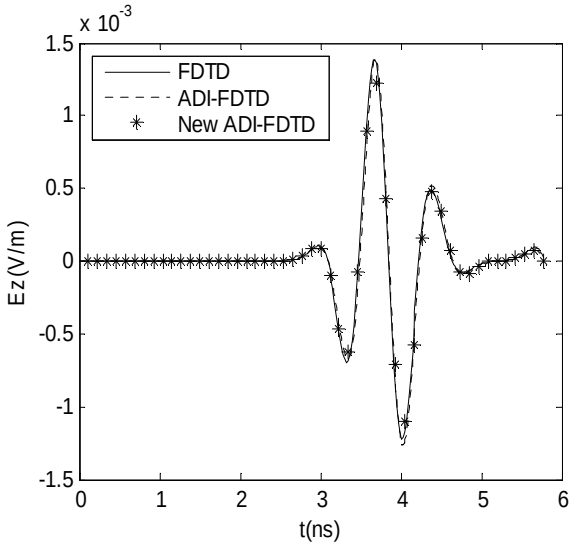

Fig. 2. Time-Domain electric field recorded at the observation point calculated by the FDTD, conventional ADI-FDTD and new ADI-FDTD methods.

The computation efficiency gain of these two ADI-FDTD methods with various $CFLN = \Delta t / \Delta t_{CFL}$ is plotted in Fig. 3. T_0 is the simulation time of the standard FDTD method,

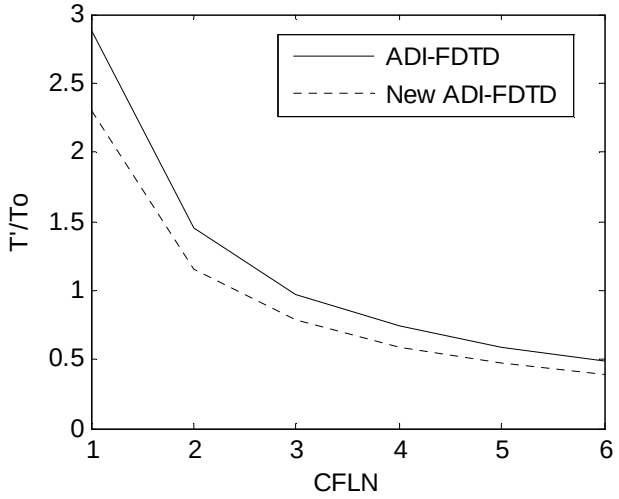

Fig. 3. Computation efficiency gain of both the conventional and present ADI-FDTD methods.

and T' denotes the computational time of the two ADI-FDTD methods respectively. It can be seen from Fig. 3 that, the simulation times for both the conventional and present ADI-FDTD method are reduced by increasing the time step size, and the computation efficiency of the new ADI-FDTD method is higher than that of conventional one obviously.

V. CONCLUSION

This letter has presented a new efficient algorithm for the unconditionally stable ADI-FDTD method. The algorithm applies the implicit difference along different directions independently, which results in updating equations whose right-hand sides are much simpler and more concise than those in the conventional implementation. This leads to substantial reduction in the number of arithmetic operations required for their computations. Compared with the conventional ADI-FDTD method, the new ADI-FDTD method is with same accuracy and higher computational efficiency, which is demonstrated by numerical example.

ACKNOWLEDGMENT

This work was supported by National Natural Science Foundations of China (No. 61001039 and 61231003), and also supported by the Research Fund for the Doctoral Program of Higher Education of China (No. 20090201120030)

REFERENCES

[1] T. Namiki, "3-D ADI-FDTD Scheme-Unconditionally Stable Time-domain Algorithm for Solving Full Vector Maxwell's Equations," *IEEE Trans. Microwave Theory Tech.*, vol.48, pp.1743-1748, 2000.

[2] F. Zheng, Z. Chen, and J. Zhang, "A Finite-difference Time-domain Method Without the Courant Stability Conditions," *IEEE Microwave Guided Wave Lett.*, vol. 9, pp. 441-443, 1999.

[3] J. Chen, and J. Wang, "PEC Condition Implementation for the ADI-FDTD Method," *Microwave Opt. Technol. Lett.*, vol. 49, pp. 526-530, 2007.

[4] S. G. García, T.-W. Lee, and S. C. Hagness, "On the Accuracy of the ADI-FDTD Method," *IEEE Antennas Wireless Propag. Lett.*, vol. 1, pp. 31-34, 2002.

[5] J. Chen, and J. Wang, "An Unconditionally Stable Subcell Model for Thin Wires in the ADI-FDTD Method," *Applied Computational Electromagnetics Society (ACES) Journal*, vol. 25, pp. 659-664, 2010.

[6] N. V. Kantartzis, "Multi-frequency Higher-order ADI-FDTD Solvers for Signal Integrity Predictions and Interference Modeling in General EMC Applications," *Applied Computational Electromagnetics Society (ACES) Journal*, vol. 25, pp. 1046-1060, 2010.

[7] J. Shibayama, J. Yamauchi, and H. Nakano, "Unconditionally Stable Locally One-dimensional FDTD Methods for Efficient Electromagnetic Simulations," 25th Annual Review of Progress in *Applied Computational Electromagnetics (ACES)*, Monterey, California, pp. 787-791, March 2009.

[8] Y. Yu, Z. Chen, "An Unconditionally Stable Radial Point Interpolation Method for Efficient Meshless Modeling in Time Domain," 25th Annual Review of Progress in *Applied Computational Electromagnetics (ACES)*, Monterey, California, pp. 389-394, March 2009.

[9] J. Chen, J. Wang, "A Novel WCS-FDTD Method with Weakly Conditional Stability," *IEEE Trans. Electromagn. Compat.*, vol. 49, pp. 419-426, 2007.

Juan Chen was born in Chongqing, China, in 1981. She received the Ph.D. degree in electromagnetic field and microwave techniques at the Xi'an Jiaotong University, Xi'an, China, in 2008. She now serves as a associate professor at Xi'an Jiaotong University. Her research interests are the numerical electromagnetic methods, antenna designs, and electromagnetic compatibility.

Electromagnetic Band Gap (EBG) Superstrate Resonator Antenna Design for Monopulse Radiation Pattern

Abbas Pirhadi[1], Hadi Bahrami[1], and Alireza Mallahzadeh[2]

[1] Cognitive Telecommunication Research Group, Department of Electrical Engineering, Shahid Beheshti University G.C (SBU), Tehran, Iran
a_prhadi@sbu.ac.ir, m.hadi.bahrami@gmail.com

[2] Faculty of Engineering, Shahed University, Tehran, Iran
mallahzadeh@shahed.ac.ir

Abstract ─ A high directive electromagnetic bandgap (EBG) antenna operating in a wide frequency band is used to design a monopulse radiation pattern. Four aperture coupled microstrip antennas (ACMA) are used as feeding sources in this EBG antenna, and a frequency selective surface (FSS) is used as a superstrate layer. By suitable design of a wideband feeding network, it is possible to obtain a monopulse radiation pattern in E&H-Planes simultaneously. In this antenna, using the superstrate layer and the ACMA simultaneously, leads to produce a wide frequency band for the antenna reflection coefficient. Also, high directivity is achieved only by using the superstrate layer that has been made by the FSS layer with square loop elements. At first, a wideband ACMA is designed to operate in x-band. Secondly, after the design of optimum superstrate layer by the FSS structure, it is added to the four ACMA in order to increase both bandwidth and directivity. Finally, a wideband feeding network which operates in X-Band is designed to produce monopulse radiation pattern. The EBG antenna operates in three different modes including one sum radiation pattern and two difference radiation patterns in E&H-Planes simultaneously.

Index Terms ─ Aperture coupled microstrip antennas (ACMA), electromagnetic bandgap (EBG), and monopulse radiation pattern.

I. INTRODUCTION

Electromagnetic bandgap structures are periodic structures that can be used to control and manipulate the propagation of electromagnetic waves. The high directive resonator antenna is an example of antenna application of EBG structures which is also called the EBG antenna [2-4]. The EBG antenna consists of a feeding source and some superstrate layers. By suitable design of the superstrate layers it is possible to obtain a high directive antenna. There are several configurations for the design of the superstrate layer. In low profile antenna applications this layer must be compact, easy to fabricate and commercially available [5-8]. To this purpose, frequency selective surfaces (FSS) can be good candidates. Various configurations such as ring, patch, square loop, strip and slot shapes have been used to design FSS superstrate layer [9-11]. By using the FSS superstrate layer singularly, or combination of the FSS layer and reactive surface, the bandwidth, polarization and radiation pattern characterizations such as side lobe level (SLL) can be controlled [12-16]. Beside the enhancement of directivity, the FSS superstrate layer can be used as a polarizer. In this case, it is possible to obtain circular polarization by using a single source [17, 18].One of the most important challenges in the design of the EBG antenna is its frequency bandwidth for the reflection coefficient and maximum directivity. These characteristics depend on the FSS superstrate layer and feed source [19-20]. Among various feeding sources that have been used, microstrip antennas, because of their low profile and easy construction are very desirable. The authors in [21], beside the enhancement of directivity, have studied the effect of the FSS

Submitted On: Nov. 30, 2011
Accepted On: March 4, 2012

superstrate layer on the reflection coefficient of a probe-fed microstrip antenna.

In this paper, using an ACMA as the feeding source and an FSS layer as the superstrate, the EBG antenna will be studied. The reflection coefficient of the ACMA has the widest frequency bandwidth among the single fed microstrip antennas. This phenomenon is obtained by suitable design of coupling aperture configuration, but the directivity of the antenna decreases in the 10dB return loss (RL) bandwidth. The FSS superstrate layer is used to solve this problem. In addition, beside the directivity, a wide frequency band for the reflection coefficient by a suitable design of the FSS superstrate layer is obtained. Compared to monopulse slotted waveguide array antennas, it operates in a wider frequency bandwidth. A typical 10dB RL bandwidth of monopulse slotted waveguide array is less than 10% [1-chapt.46, 28]. Also, compared to monopulse microstrip array antennas, it has a simpler feeding network and therefore a little loss of power in the feeding network. It must be noticed that in the microstrip array antennas the microstrip feeding network is distributed for all elements and some of the power is dissipated as undesirable radiation power in the feeding network.

In Section II, the FSS superstrate layer and the ACMA are designed separately and in Section III, the combination of ACMA and FSS superstrate layer are studied. In this section, the most effective parts that influence the radiation characteristics and the bandwidth of the antenna are examined parametrically. In Section IV, to design the monopulse antenna four ACMA are used as the feeds of the EBG antenna. By suitable excitation of these four antennas, it is possible to obtain different radiation patterns including two difference radiation patterns and a sum radiation pattern. Also, in this section a suitable wideband feeding network which produces such excitations of the antennas, is designed. All simulations have been done by high frequency structure simulator (HFSS) based on finite element method (FEM).

II. DESCRIPTION OF THE ANTENNA CONFIGURATION

The antenna structure is composed of three sections including coupling aperture, radiating patch and the FSS superstrate layer (Fig. 1a). The antenna configuration to design monopulse antenna is depicted in the Fig. 1b.

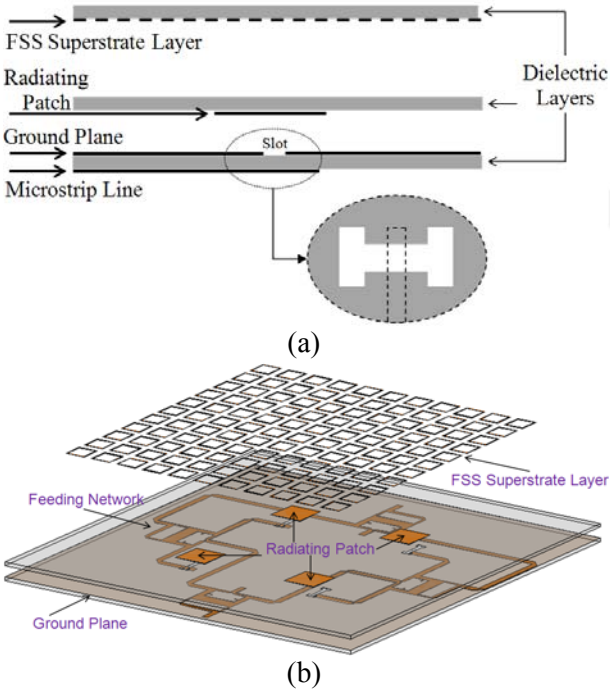

Fig. 1. (a) Geometry of EBG antenna fed by a single aperture coupled microstrip patch. (b) Geometry of EBG antenna fed by four apertures coupled microstrip antennas to design monopulse antenna.

A. Design of the FSS Superstrate Layer

There are different configurations and methods to design the superstrate layer. In fact, this layer acts as a partially reflecting surface. Near its resonance frequency where the reflection coefficient of surface is about unity, radiating source, and the superstrate layer produce resonance condition. In this case, the directivity of antenna increases considerably [7, 11]. The resonance frequency of the FSS superstrate layer has to coincide with a desired operating frequency. In this paper the square loop elements have been used to design the FSS superstrate layer. The square loop has symmetrical geometry and can be used in dual polarize and dual band applications. Also, compared with the patch element it has a more compact size and a more controllable resonance frequency. Figure 2 shows the amplitude and phase of reflection coefficient of the FSS superstrate layer. Because of the periodicity of the FSS superstrate layer, to determine its

reflection coefficient of the FSS, it is enough to analyze just one cell.

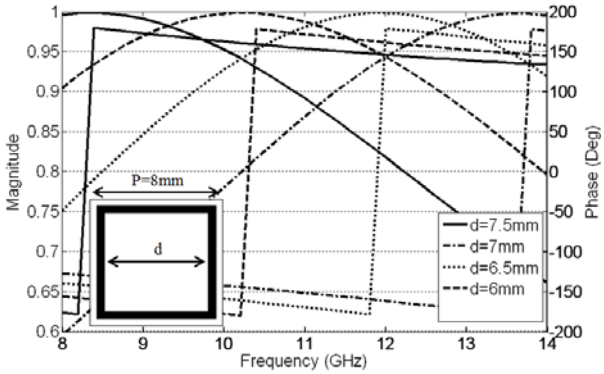

Fig. 2. Magnitude and phase of reflection coefficient of FSS.

Figure 3 shows how the FSS superstrate layer in combination with an aperture coupled microstrip antenna is used to produce resonance condition. In this configuration, there are three layers that are important in producing resonance condition. These layers are the ground plane in which the coupling aperture of ACMA has been placed, the dielectric layer in which the patch has been placed, and the FSS superstrate layer. The reflection coefficient of ground plane for horizontal electric fields is (-1). The dielectric layer reflects and transmits the EM fields with coefficients proportional to the thickness and dielectric properties of layer and the FSS layer reflects and transmits the EM fields according to the Fig. 2. Among these layers, only the FSS layer can be adjusted. This layer must be adjusted so that all of the EM fields in outer region of the structure are added constructively. In this case, the reflection coefficient phase of the whole structure in Fig. 3 is $2n\pi$ and the resonance condition takes place [22].

After determining the primary values of the FSS superstrate parameters, its combination with ACMA will be studied to obtain the optimum values of the EBG antenna. The most important parameters to adjust the resonance frequency are the height of the FSS layer, periodicity of the FSS elements, and dimensions of the FSS elements. In the EBG antenna because the antenna equivalent aperture increases, the directivity increases in the frequency band about the resonance frequency.

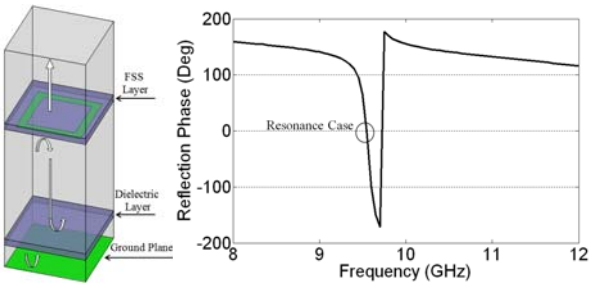

Fig. 3. (a) Unit cell of the whole structure, (b) phase of the reflection coefficient for the resonance condition of unit cell.

B. Design of Wideband Aperture Coupled Microstrip Antenna

The configuration of ACMA is shown in Figure 4. Many useful features of this type of antenna attract designers to use it for various applications [23-25].

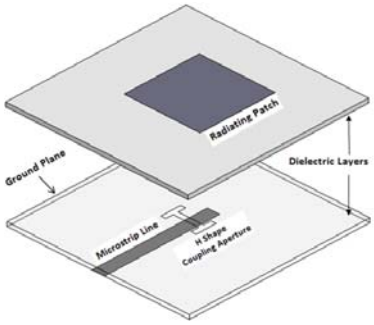

Fig. 4. Configuration of ACMA.

The capability of this antenna is obtaining wide bandwidth for 10dB RL bandwidth by suitable design of its coupling aperture. This phenomenon is obtained by using a cross-shaped coupling slot, two orthogonal offset slots and so on. In this paper the H shape slot is used [26]. By using this structure, two resonance frequencies due to the patch and slot are adjusted to obtain the wide frequency band for reflection coefficient. Figure 5 shows the directivity and reflection coefficient of the ACMA feeding by H shape slot. The ACMA antenna and the FSS superstrate layer are designed on PCB microwave board (Rogers RO3003) with a relative dielectric constant of ε_r=3.38, a dielectric loss tangent=.0027 and thickness=.782mm. By using the H shape slot, the resonance frequency of the coupling aperture moves next to the resonance frequency of patch.

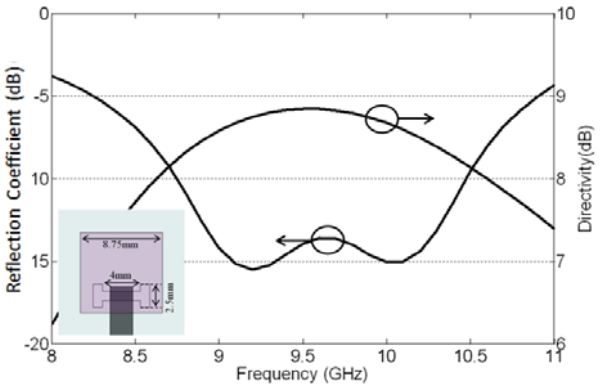

Fig. 5. Reflection coefficient and directivity of ACMA fed by H shape slot and dielectric height=3mm.

III. PARAMETRIC STUDY OF ANTENNA THE WIDEBAND HIGH DIRECTIVE ACMA

In this section, the effects of important parameters such as the height and dimensions of the FSS layer on both the reflection coefficient and the directivity of the antenna are studied. By varying the height of the FSS, the resonance frequency of the EBG antenna is displaced. Moreover, to keep the resonating condition in the EBG antenna, it is necessary to modify the dimensions of the FSS elements. This modification for large variations of the height of the FSS is considerable but for small variations it is negligible. In the Fig. 6, the effects of the height of FSS superstrate layer on the reflection coefficient and the directivity of antenna has been shown. To this purpose, the EBG antenna has been simulated for the different values of the FSS superstrate layer heights. Figure 6a depicts that increasing the height of the FSS leads to the movement of the 2nd resonance frequency toward a lower frequency. Also, it is observed form the Fig. 6-b that the maximum directivity of the antenna moves to the lower bound of the frequency bandwidth.

Another important parameter in the design of the EBG antenna is the FSS dimensions. In this case, the antenna is considered as a leaky wave antenna (LWA). The leaky waves propagate toward the edges of FSS and produce radiating current distribution on the FSS layer. Increasing the dimensions of FSS layer, leads to the increase of the radiating aperture of the antenna.

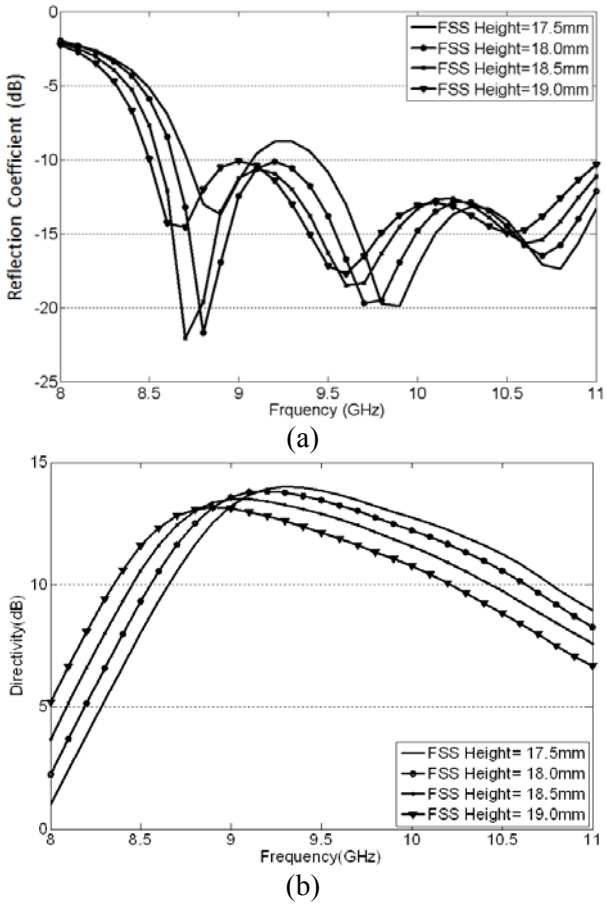

Fig. 6. Effect of FSS height (a) directivity of EBG antenna; (b) reflection coefficient of EBG antenna.

In the 2-D LWAs which are constructed using FSS surface, the leakage current is tapered toward the edges of the FSS [22, 27]. Therefore, the dimensions of the FSS superstrate layer must be chosen such that, the reflected wave from the edges of FSS can be neglected. To examine the effects of the FSS dimensions, the FSS superstrate layer is studied with different number of cells. Figure 7 depicts the reflection coefficient and the directivity of the antenna for the FSS with different number of cells. Simulation results show that enhancing the dimension of the FSS more than 11×11 elements, has a little effect on the 10dB RL bandwidth.

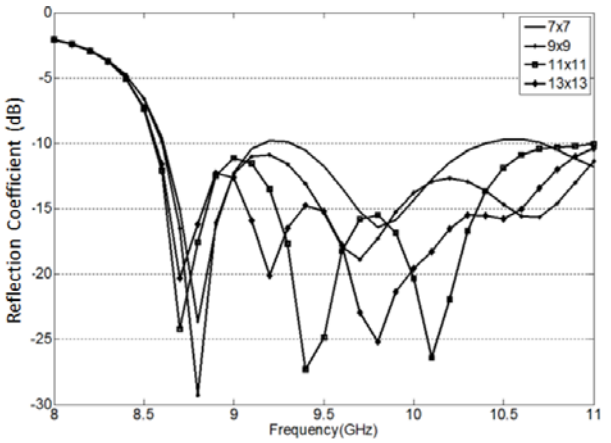

(a)

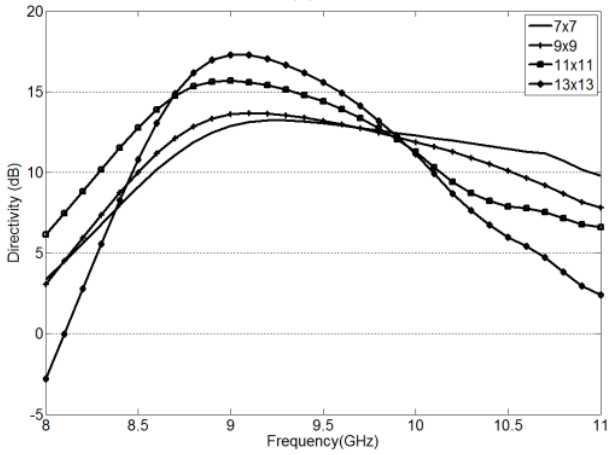

(b)

Fig. 7. Effect of the FSS with different cell number. (a) reflection coefficient of EBG antenna. (b) Directivity of EBG antenna.

The above mentioned parameters are important in the design of the EBG antenna with a single feed. Another important parameter which must be investigated in the design of the EBG antenna to achieve the monopulse radiation pattern is the distance of the feeding sources from each other. This parameter affects the aperture current distribution of the EBG antenna in operating modes. The effect of this parameter on the directivity of the EBG antenna in the sum mode is depicted in the Fig. 8. Increasing the distance of the feeding sources leads to the reduction of mutual coupling and therefore, the reduction of reflection coefficient of the EBG antenna in different operating modes.

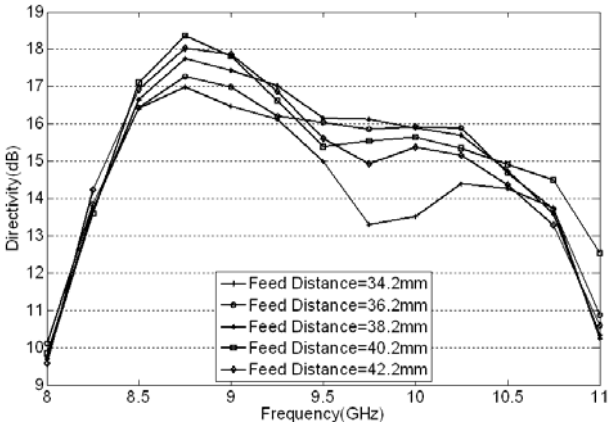

Fig. 8. Effect of the distance of feeding sources.

IV. DESIGN OF MONOPULSE ANTENNA AND EXPERIMENTAL RESULTS

A. Monopulse Radiation Patterns and Feeding Network

To design a monopulse antenna, it is necessary to have four feeds in the EBG antenna. By suitable excitation of the feeds and adjusting their distances, it is possible to obtain different current distributions on the FSS. These currents produce the various operating modes of the monopulse antenna in E and H planes. The combination of the feeds and the FSS layer is depicted in Fig. 1. Also, the current distributions on the FSS layer for various operating modes are depicted in the Fig. 9. In the difference modes as shown in the Fig. 9, the surface currents of the radiating aperture are such that the antenna produces the radiation patterns with the null in E & H planes (Fig. 14).

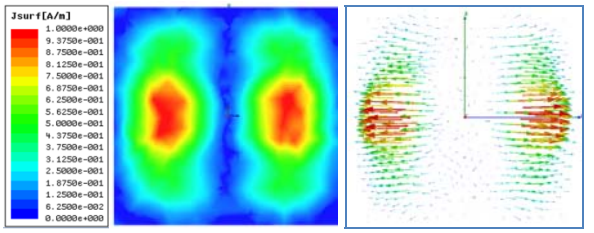

(a)

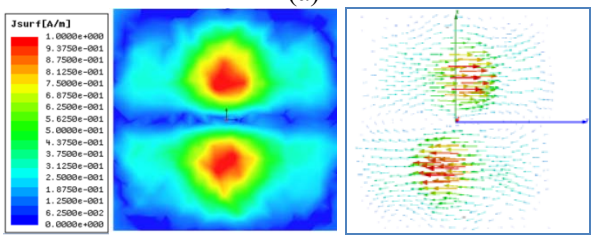

(b)

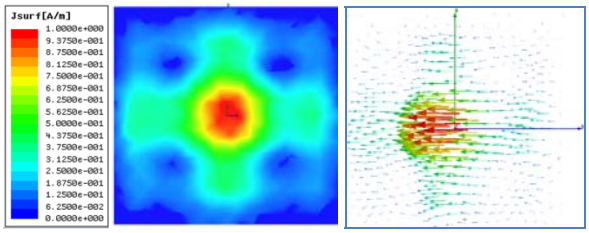

(c)

Fig. 9. Current distribution on the FSS surface at f=9.5GHz. (a) Difference mode in E-plane. (b) Difference mode in H-plane. (c) Sum mode.

The feeding network is necessary to produce the various excitations for the feeds. To design the feeding network four rat-races are necessary. The most important challenge in the design of the feeding network is its wideband operating frequency in which it is necessary to use wide band rat-race. The designed feeding network has been shown in Fig. 10.

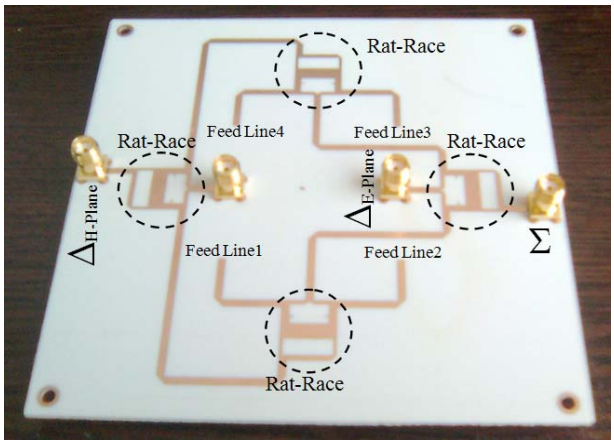

(a)

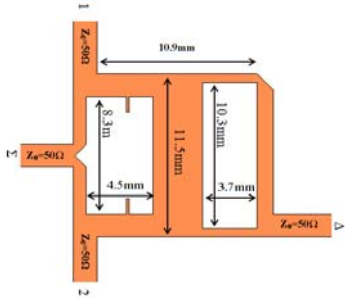

(b)

Fig. 10. (a) Fabricated feeding network for the monopulse EBG antenna; (b) wideband rat-race.

The feeding network has four ports including two difference ports and one sum port. The fourth port is terminated with the 50Ω matched load. Table 1 shows the excitations of four ACMA when the different ports are exited. It must be noticed that the antennas 1 and 2 are symmetrically mirrored respect to antennas 3 and 4. Therefore, in the Table 1, π degree phase shift has to be added to antennas 3 and 4.

Table 1: Excitation of ACMA when the different ports are excited

Input Port	*Antenna 1*	*Antenna 2*	*Antenna 3*	*Antenna 4*
$\sum$	$1e^{j0}$	$1e^{j0}$	$1e^{j\pi}$	$1e^{j\pi}$
Δ_{-E}	$1e^{j0}$	$1e^{j0}$	$1e^{j0}$	$1e^{j0}$
Δ_{-H}	$1e^{j\pi}$	$1e^{j0}$	$1e^{j\pi}$	$1e^{j0}$

B. Experimental Results

The Fig. 11 shows the fabricated EBG antenna. In the final design, the air gap between the substrates of the slots and radiating patches is 3.5mm and the distance of the substrate of FSS from the patch is 14.75mm. Also, the periodicity of FSS elements is 7mm and the width of square loops of the FSS is 5mm with 0.2mm thickness. The distance between the feeding sources of antenna is 36.2mm.

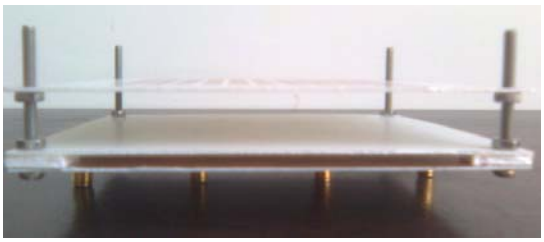

(a)

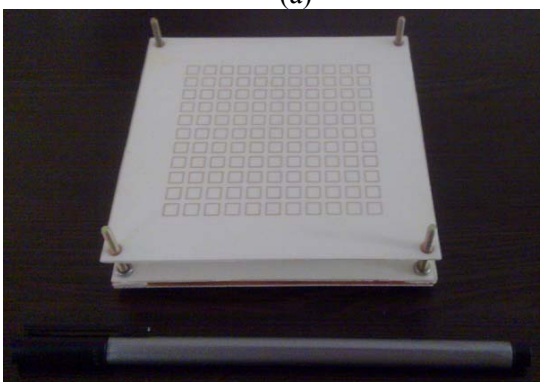

(b)

Fig. 11. The fabricated monopulse EBG antenna (a) side view; (b) top view.

The reflection coefficient of antenna for different ports has been shown in Fig. 12.

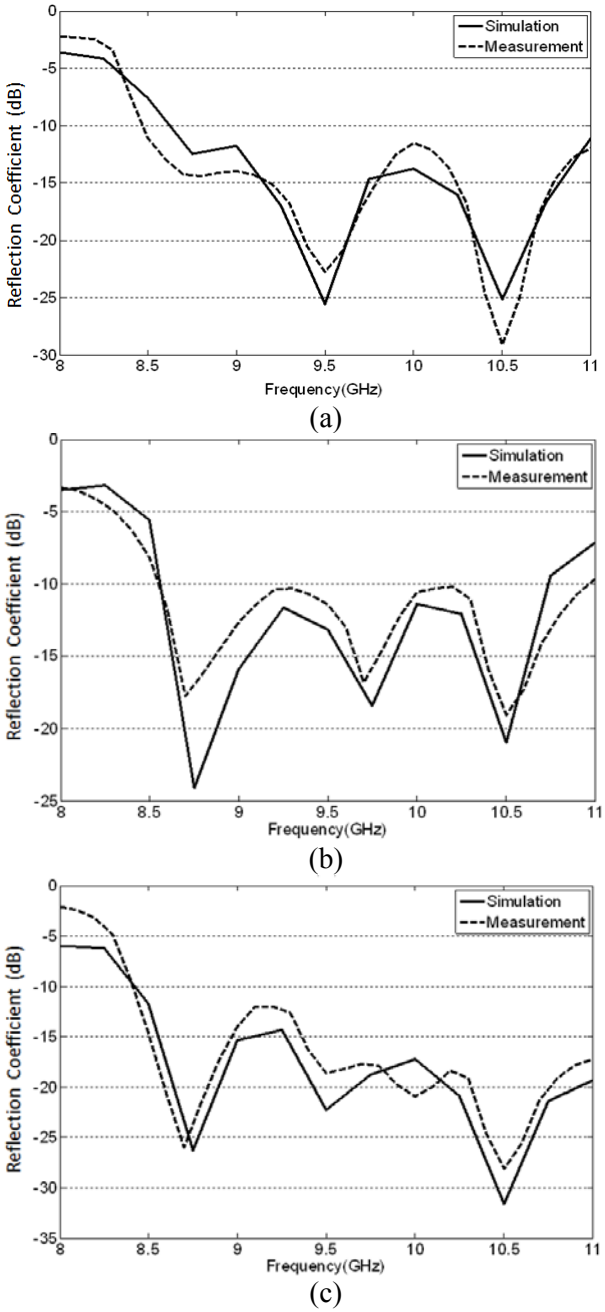

Fig. 12. Reflection coefficient of ACMA in the presence of the FSS layer (a) sum mode, (b) difference mode in E-plane, (c) difference mode in H-plane.

The antenna gain in the sum operating mode has been depicted in Fig. 13.

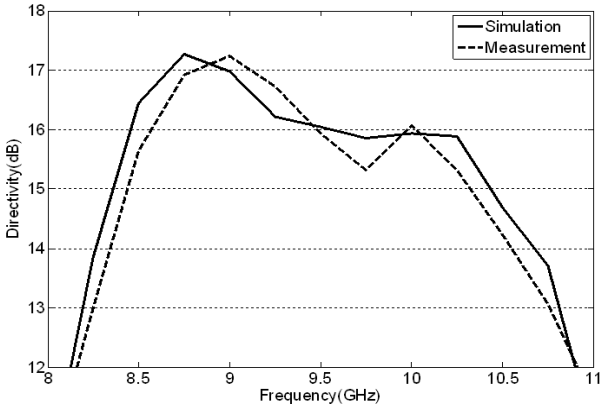

Fig. 13. Directivity of ACMA in the presence of FSS layer in the sum mode.

The radiation patterns of the monopulse EBG antenna for 8.5GHz and 10.5GHz in (E & H) planes for different operating modes are shown in the Fig. 14. By increasing the operating frequency, the relative spaces (respect to λ) between the feeds of the EBG antenna will increase. Therefore, the grating lobes in the sum mode will appear in the upper frequencies. The back lobe of the antenna is due to coupling aperture of ACMA. To reduce the back lobe level especially in the sum mode, the conducting plate or absorbing material can be placed behind the antenna.

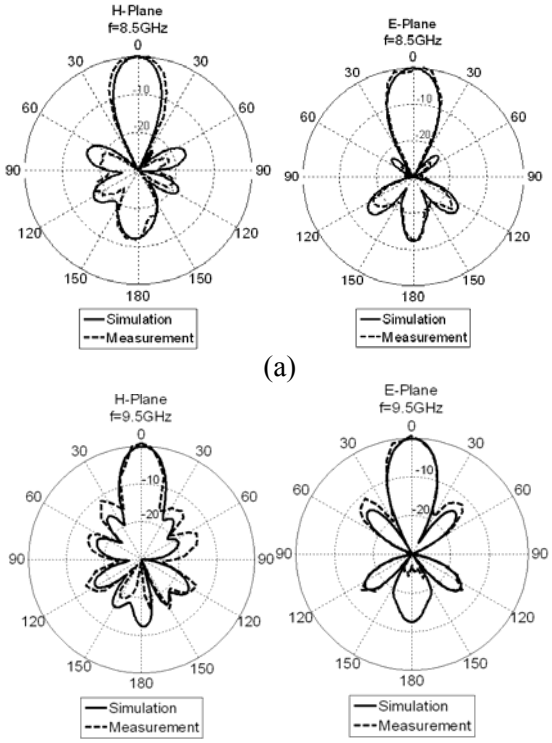

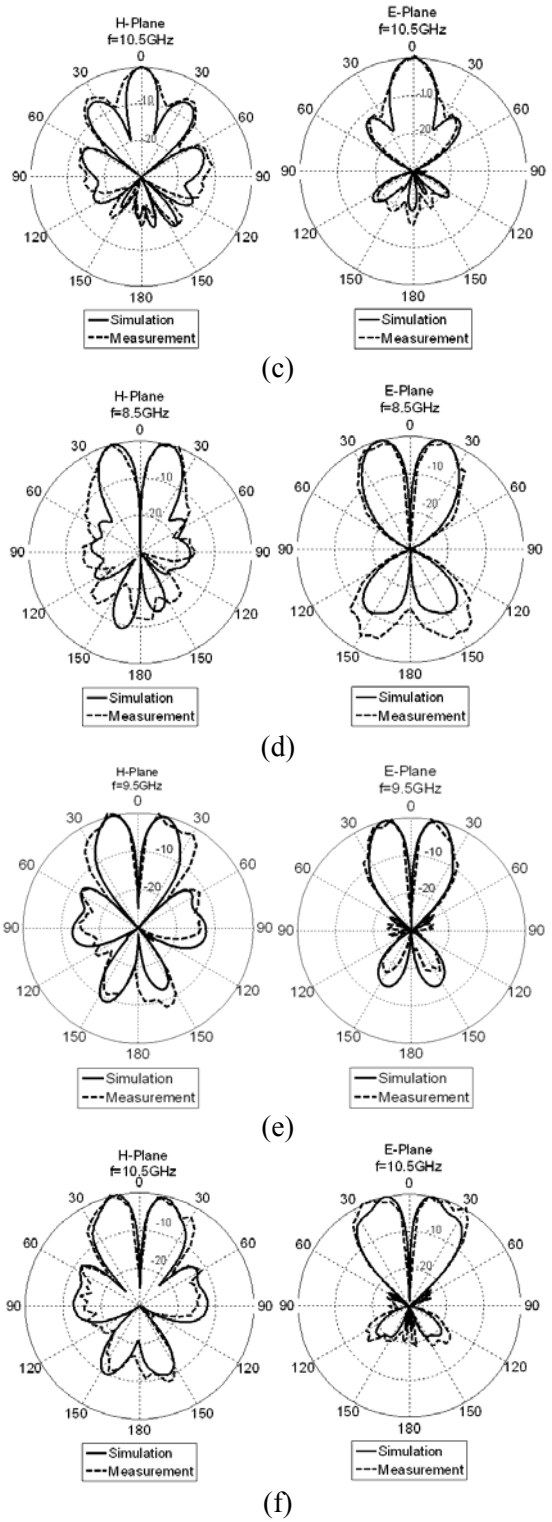

Fig. 14. Measurement and simulation results of normalized electric field radiation patterns of antenna for E&H-planes. (a) Sum mode at f=8.5GHz; (b) sum mode at f=9.5GHz; (c) sum mode at f=10.5GHz; (d) difference mode at f=8.5GHz; (e) difference mode at f=9.5GHz; (f) difference mode at f=10.5GHz.

VI. CONCLUSION

In this paper, the monopulse antenna has been designed using the EBG antenna. The bandwidth of the EBG antenna with ACMA feed for both directivity and reflection coefficient is about 20% at center frequency 9.5GHz. Based on this characteristic it is possible to design a wideband monopulse antenna with the EBG antennas with four ACMA feeds. This type of monopulse antenna has wide bandwidth and also a simple feeding network. In the future, by using the different combinations of the feeds it is possible to obtain shaped beam radiation pattern with the EBG antenna.

REFERENCES

[1] J. Volakis, *Antenna Engineering Handbook*, McGraw-Hill, 2007.

[2] H. Boutayeb, K. Mahdjoubi, A.-C. Tarot, and T. A. Denidni, "Directivity of an Antenna Embedded Inside a Fabry–Perot Cavity: Analysis and Design," *Microwave And Optical Technology Letters* , vol. 48, no. 1, pp.12-17, January 2006.

[3] A. R. Weily, K. P. Esselle, B. C. Sanders, and T. S. Bird, "High-Gain 1d EBG Resonator Antenna," *Microwave and Optical Technology Letters*, vol. 47, no. 2, pp. 107-114, October 20, 2005.

[4] Y. J. Lee,J. Yeo, R. Mittra,, and W. S. Park, "Application of Electromagnetic Bandgap (EBG) Superstrates with Controllable Defects for a Class of Patch Antennas as Spatial Angular Filters," *IEEE Transactions on Antennas And Propagation*, vol. 53, no. 1, pp. 224-235, January 2005.

[5] Y. Lee, X. Lu, Y. Hao, S. Yang, R. Ubic, J.R.G. Evans, and C. G. Parini, "Directive Millimetre-Wave Antenna Based on Free Formed Woodpile EBG Structure," *Electronics Letters* , vol. 43 no. 4, February 2007.

[6] A. Semichaevsky and A. Akyurtlu, "Homogenization of Metamaterial-Loaded Substrates and Superstrates for Antennas," *Progress in Electromagnetics Research*, Pier 71, 129–147, 2007.

[7] A. Pirhadi, M. Hakkak, F. Keshmiri, and R. K. Baee, "Design of Compact Dual Band High Directive Electromagnetic Bandgap (EBG) Resonator Antenna Using Artificial Magnetic Conductor," *IEEE Transactions on Antennas and Propagation*, vol. 55, no. 6, pp. 1682-1690, June 2007.

[8] A. Foroozesh, M. Ngmou Kehn, and L. Shafai, "Application of Artificial Ground Planes in Dual-Band Orthogonally-Polarized Low-Profile High-Gain Planar Antenna Design," *Progress in Electromagnetics Research*, Pier 84, 407–436, 2008.

[9] D. H. Lee, Y. J. Lee, J. Yeo, R. Mittra, and W. S. Park, "Design of Metamaterial Superstrates and Substrates for Directivity and Port Isolation Enhancement of a Dual-Frequency Dual Polarization Microstrip Antenna," *Microwave and Optical Technology Letters*, vol. 48, no. 9, pp. 1873-1876, September 2006.

[10] A. Pirhadi, F. Keshmiri, M. Hakkak, and M. Tayarani, "Analysis and Design of Dual Band High Directivity EBG Resonator Antenna using Square Loop FSS as Superstrate Layer," *Progress in Electromagnetics Research*, Pier 70, pp. 1–20, 2007.

[11] U. Ge and K. P. Esselle, "A Resonant Cavity Antenna Based on an Optimized Thin Superstrate," *Microwave and Optical Technology Letters*, vol. 50, no. 12, pp. 3057-3059, December 2008.

[12] A. R. Weily, T. S. Bird, and Y. J. Guo, "A Reconfigurable High-Gain Partially Reflecting Surface Antenna," *IEEE Transactions on Antennas and Propagation*, vol. 56, no. 11, pp. 3382-3390, November 2008.

[13] D. Kim, "Novel Dual-Band Fabry-Perot Cavity Antenna with Low Frequency Separation Ratio," *Microwave and Optical Technology Letters*, vol. 51, no. 8, pp.1869-1872, August 2009.

[14] R. Sauleau and P. Coquet, "Input Impedance of Electromagnetic Bandgap Resonator Antennas," *Microwave and Optical Technology Letters*, vol. 41, no. 5, pp. 369-375, June 2004.

[15] E. Rodes, M. Diblanc, E. Arnaud, T. Monediere, and B. Jecko, "Dual-Band EBG Resonator Antenna Using a Single-Layer FSS," *IEEE Antennas and Wireless Propagation Letters*, vol. 6, pp. 368-371, 2007.

[16] Z.-H. Wu and W.-X. Zhang, "Broadband Printed Compound Air-Fed Array Antennas," *IEEE Antennas and Wireless Propagation Letters*, vol. 9, pp.187-190, 2010.

[17] E. Arnaud, R. Chantalat, M. Koubeissi, T. Monediere, E. Rodes, and M. Thevenot, "Global Design of an EBG Antenna and Meander-Line Polarizer for Circular Polarization," *IEEE Antennas and Wireless Propagation Letters*, vol. 9, pp. 215-218, 2010.

[18] Ibid, "Performance Enhancement of Self-Polarizing Metallic EBG Antennas," *IEEE Antennas and Wireless Propagation Letters*, vol. 9, pp. 538-541, 2010.

[19] R. Alkhatib and M. Drissi, "Improvement of Bandwidth and Efficiency for Directive Superstrate EBG Antenna," *Electronics Letters*, vol. 43, no. 13, June 2007.

[20] L. Moustafa and B. Jecko, "Design of a Wideband Highly Directive EBG Antenna Using Double-Layer Frequency Selective Surfaces and Multi feed Technique for Application in the Ku-Band," *IEEE Antennas and Wireless Propagation Letters*, vol. 9, pp. 342-346, 2010.

[21] A. Pirhadi, M. Hakkak, and F. Keshmiri, "Using Electromagnetic Bandgap Superstrate to Enhance the Bandwidth of Probe-Fed Microstrip Antenna," *Progress in Electromagnetics Research*, Pier 61, pp. 215–230, 2006.

[22] S. Wang, A. P. Feresidis, G. Goussetis, and J. C. Vardaxoglou, "High Gain Sub Wavelength Resonant Cavity Antennas Based on Metamaterial Ground Planes," *IEE Proc. Microwave Antennas and Propagation*, vol. 153, no. 1, pp. 1-6, 2006.

[23] D. M. Pozar, "A Review of Aperture Coupled Microstrip Antennas: History, Operation, Development, and Application", *Microwave Online System Company world wide web site*, July 1996.

[24] F. Croq and A. Papiernik, "Large Bandwidth Aperture-Coupled Microstrip Antenna," *Electronics Letters*, vol. 26, no. 16, pp. 1293-1294, August 1990.

[25] S. D. Targonski, R. B. Waterhouse, and D. M. Pozar, "Design of Wide-Band Aperture-Stacked Patch Microstrip Antennas," *IEEE Trans. on Antennas and Propag*., vol. 46, no. 9, pp. 1245-1251, September 1998.

[26] S.-C. Gao, L.-W. Li, M.-S. Leong, and T.-S. Yeo, "Wide-Band Microstrip Antenna with an H-Shaped Coupling Aperture," *IEEE Trans. on Vehicular Technology*, vol. 51, no. 1, pp.17-27, January 2002.

[27] R. Garg, P. Bhartia, I. Bahl, and A. Ittipiboon, *Microstrip Antenna Design Handbook*, Artech House, 2001.

[28] S. R. Rengarajanl and S. Chatterjee, "An Investigation of Bandwidth Characteristics of Waveguide-Fed Planar Slot Arrays" *Electromagnetics*, vol. 29, issue 7, pp. 515-521, September 2009.

Abbas Pirhadi received B.S. degree in electrical engineering from the Isfahan University of Technology, Isfahan, 2000, and M. S. and Ph.D. degree in communication engineering from Tarbiat Modares University, Tehran, in 2002 and 2007, respectively. From 2002 to 2006, he joined the Antenna and Propagation Group of the Iran Telecommunication Research Center (ITRC) as a researcher. Also, in 2007 he joined the Shahid Beheshti University where he is the Assistant Professor at the faculty of Electrical and Computer engineering. His research interests include microwave antennas, theoretical and computational electromagnetic with applications to antenna theory and design, Metamaterials and electromagnetic Bandgap materials used in antenna design.

Hadi Bahrami received the B.S. and M.S. degrees in electrical engineering 2005 and 2007 from Isfahan University of Technology, Isfahan, Iran and Tarbiat Modares University, Tehran, Iran, respectively. Since then, he has been a Ph.D. student in electrical engineering department, Laval University, Quebec City, Canada. As his Ph.D. research program, he is currently working on design of ultra wideband low-power transceiver for biomedical applications.

Alireza Mallahzadeh received the B.S. degree in electrical engineering from Isfahan University of Technology, Isfahan, Iran, in 1999 and M.S. and the Ph.D. degree in electrical engineering from Iran University of Science and Technology in 2001 and 2006 respectively. He is a member of academic staff, Faculty of Engineering, Shahed University, Tehran, Iran. He has participated in many projects relative to antenna design, which resulted in fabricating different types of antennas for various companies. Also, he is interested in numerical modeling, and microwaves. Dr. Mallahzadeh is a member of IEEE and ACES.

Triangular Patch Yagi Antenna with Reconfigurable Pattern Characteristics

Jian Zhang, Xue-Song Yang, Jia-Lin Li, and Bing-Zhong Wang

Institute of Applied Physics,
University of Electronic Science and Technology of China, Chengdu, 610054, China
zhjian0928@163.com, xsyang@uestc.edu.cn, jialinuestc@gmail.com, bzwang@uestc.edu.cn

Abstract ─ A pattern reconfigurable Yagi patch antenna is proposed. The antenna is composed of three triangular microstrip patches, i.e., one driven patch and two parasitic patches. By controlling switches, which are installed on the parasitic patches, the radiation pattern of the antenna can point to three different directions, covering an elevation range from -61° to +63° in the E-plane. The simulated and measured results are presented and they agree with each other in reasonable precision.

Index Terms ─ Microstrip antennas, pattern reconfigurable antennas, Yagi-Uda arrays.

I. INTRODUCTION

Reconfigurable antennas have received a lot of attention since they can provide various functions in operating frequency, beam pattern, and polarization, etc. [1-2]. The antenna that can change radiation pattern and maintain operating frequency is called pattern reconfigurable antenna. The pattern reconfigurable antenna has the potential to improve the overall system performance by changing beam directions to avoid electronic jamming or noise source, improve security and save energy [3-4].

It is in great demand for pattern reconfigurable antennas in the fields of wireless communications, satellite communications, radars, etc. Usually, phased antenna arrays are used to accomplish beam steering [5-6]. In the traditional microstrip phased array, where the array elements have fixed beam patterns, the beam scanning is accomplished by using phase shifters. As a result, the scanning range of the array is somewhat limited [6]. If the array element is replaced by the pattern reconfigurable antenna, an additional degree of freedom is provided and the scanning range of the array can be enlarged correspondingly [7-8]. Furthermore, the pattern reconfigurable antenna has found application in MIMO wireless communications to improve the communication system performance [9].

Yagi-Uda antenna has the ability to tilt broadside pattern to endfire pattern. Based on the principle of Yagi-Uda antenna, some pattern reconfigurable antennas have been reported [2, 10-12]. For example, a pattern reconfigurable Yagi microstrip dipole antenna has been presented [10]. By adjusting the lengths of parasitic dipoles, the main beams can change directions in the H-plane. Another reconfigurable Yagi antenna is proposed in [11]. All the elements are square patches and have switches installed in the slots on parasitic patches. By changing the states of switches, the parasitic elements can be used as directors or reflectors. The main beams of three modes of this antenna can cover a continuous range in the E-plane in the upper half space.

Most of the reported reconfigurable antennas use switches to achieve antennas reconfigurability [13-16]. With the rapid development of MEMS, semiconductor, and photoconductor technologies, most of the reconfigurable antennas can be easily fabricated using different switches. PIN diode has been extensively explored for designing various reconfigurable antennas due to a lot of advantages, such as good reliability, compact size, high switching speed, and small resistance and capacitance in the ON and OFF states. Although the PIN diode enables fast configuration speed, it is lossy and can affect the antenna performance if

Submitted On: May 22, 2012
Accepted On: August 22, 2012

not properly designed. An alternative is RF MEMS switch, which has excellent properties, such as low loss, low power consumption and high isolation. Photoconductor switch has an outstanding characteristic of immunity to electromagnetic waves, consequently, without interference to antenna radiation pattern. The main disadvantage of MEMS and photoconductor switches is the high cost.

Some papers have compared the effects of the actual switches and the ideal switches [15-16]. In [16], a PIN diode was used to configure the operating frequency of a slot antenna. By controlling its biasing voltage, a diode can be easily turned ON and OFF. It is always very desirable to have a diode that has low loading effect (OFF state) and small resistance (ON state). Obviously, the ON-state resistance can result in power dissipation and degrade the antenna radiation efficiency. For such a reconfigurable antenna, the total dissipated power depends on the diode's ON resistance and the number of switches being used.

A novel triangular patch Yagi antenna, consists of three triangular patches, is proposed in this paper. By controlling the switches installed on the parasitic patches, the antenna can work at three modes, and the maximum beam direction shifts among -32°, +10° and +34° as predicted, where '+' indicates that the radiation pattern tilts towards the positive *x*-axis and '-' towards the negative *x*-axis. The state of the director is different from that in [11], i.e. the director in the proposed antenna has a similar state to the reflector in [11]. Besides, the proposed antenna has only two parasitic elements, which makes the antenna much smaller than that in [11], which makes the antenna more easily be used in antenna arrays. Furthermore, the loaded slots are simpler, and only four switches are needed to control the radiation pattern direction, which reduces the cost and makes the antenna mode adjusting more convenient.

II. ANTENNA DESIGN

The principle of Yagi-Uda patch antenna with a driven and three parasitic rectangular patch elements is well known [12]. In this initiative article, the sizes of parasitic patches are different, with the small patches used as directors and the largest one acted as a reflector. In this paper, the proposed triangular patch Yagi antenna has three elements, one driven patch and two parasitic patches, as shown in Fig. 1. All elements are equilateral triangular patches, and are supported on the top side of a grounded substrate with height of 0.76 mm and dielectric constant of 2.94. The parasitic elements are two identical triangular patches and a little smaller than the driven one. A coaxial probe is used to feed the antenna from the bottom of the substrate and the feed point is located at the symmetry axis of the antenna. There is a narrow rectangular slot on each parasitic patch, and two switches are installed in each slot to change the equivalent capacitance and inductance of the patch. Figure 2 (a) shows the detail of the parasitic element.

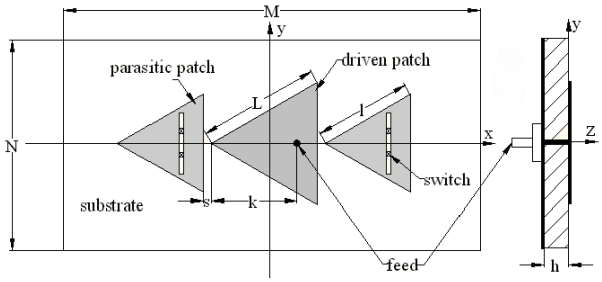

Fig. 1. Geometry of the proposed antenna.

The parameters of the antenna are as follows: M=34 mm, N=17 mm, *a*=0.4 mm, *b*=1.4 mm, *c*=0.4 mm, *d*=5.0 mm, *m*=5.0 mm, *k*=7.0 mm, *L*=10.0 mm, *l*=8.0 mm, *s*=0.7 mm and *h*=0.76 mm.

By controlling the switches on the patch, two states of the parasitic element can be obtained. When both switches on the parasitic patch are open, i.e., the switches are "OFF", the parasite is acted as a director, and this state is called "D", as shown in Fig. 2 (b). This is different from the antenna in [11], where when all the switches on the parasitic patch are open, the parasite is acted as a reflector. Meanwhile, when both switches are closed, the state of the parasite is called "N", as shown in Fig. 2 (b), and the patch has nearly no effect on the radiation pattern, which is similar to that in [11]. By combining the states of parasitic elements at two sides of the driven patch, at least three different modes of the antenna, i.e., DN, ND and NN, can be obtained. DN means that the parasitic element at the left side acts as a director and the right side one has no effect on the pattern. With reference to the coordinate in Fig. 1, the main beam tilts to the negative *x*-axis. Likewise,

ND indicates that the right side parasite acts as a director and the radiated beam directs to the positive *x*-axis. NN means both sides of parasites have nearly no effect on the radiation pattern, and then the antenna has a broadside pattern. By adjusting modes of the antenna, the radiation pattern is reconfigured.

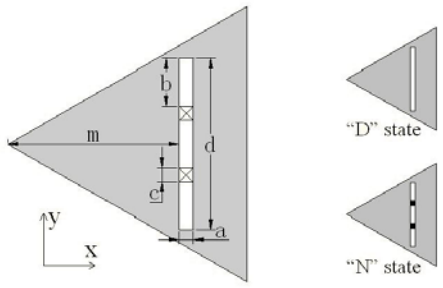

Fig. 2. (a) Geometry of the parasitic patch. (b) the specific structures at two states, where the black squares stand for the closed switches.

III. SIMULATED AND MEASURED RESULTS

A. Ideal Switches

Ansoft's HFSS is used to simulate the performance of the antenna. To validate the simulation, two prototypes, which are at modes DN and ND, respectively, are fabricated and measured. Metallic pads take the places of closed switches in the simulation and fabrication. Figure 3 shows one fabricated model at mode DN.

Fig. 3. Fabricated antenna model (mode DN).

The simulated and measured $|S_{11}|$ are shown in Fig. 4. From the simulation results, it can be seen that the resonant frequencies of all three modes are around 10.9 GHz, and the common bandwidth is from 10.74 GHz to 11.0 GHz, about 260 MHz. Compared with the simulated results, the measured resonant frequencies shift upward by about 0.15 GHz, with the common bandwidth from 10.88 GHz to 11.25 GHz. In addition, for the simulation results, a bulge appears between 10.8~11.0GHz in the DN mode, means that the resonant frequencies of the driven patch and the parasitic patches at this mode are not very closed to each other, where the lower resonance is from the driven patch and the upper one is from the D state parasitic patch [11, 15]. If the slot on the parasitic patch is longer, the upper resonance frequency will decrease, and more closed to the lower one. Consequently, the bulge will disappear. For the other modes, the resonant frequencies of different patches are much closed to each other and then seem to be one resonance. However, appropriate separate of the resonant frequencies of different patches is benefit to the widening of the bandwidth. Preliminary analysis shows that the deviation of resonant frequency of measurement from simulation should be caused by the inaccuracy of dielectric constant and the inevitable machining error.

The simulated maximum beams direct to the elevation angles of -32°, +10° and +34°, when the antenna works at modes DN, NN and ND, respectively, as shown in Fig. 4(b). At modes DN, NN and ND, the 3-dB beamwidths in the E-plane are from -61° to -3°, from -45° to +50° and from +10° to +63°, respectively. That means the radiation pattern of the antenna can cover the elevation range from -61° to +63° in the upper half space by switching among these three modes. Compared with the antenna in [11], whose scanning angle is from -69° to +67°, the beam coverage of the proposed antenna is a little narrower, but its whole dimensions are much smaller. The simulated antenna gains, corresponding to the operating frequency of 10.9 GHz, are 8.44, 6.80 and 8.85 dBi at modes DN, NN and ND, respectively.

Figure 5 shows the current distribution at the modes DN, ND and NN, respectively. When the switches on the left side parasitic patch are open, strong current distribution arises around the slot and also the driven patch bevel edges close to the parasite. While the switches on the right side parasitic patch are open, strong current distribution arises around the slot, but on the driven patch, only weak current appears at the driven patch bevel edges. However, when all the switches are closed, strong current distribution appears at the driven patch, including the bevel edges and the central part. Therefore, both the slots and the shape of the patches have Fig. 5 shows the current distribution.

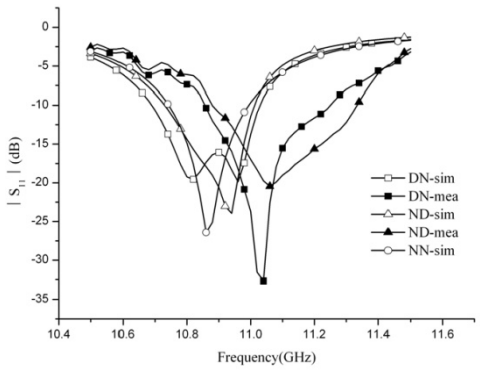

(a)

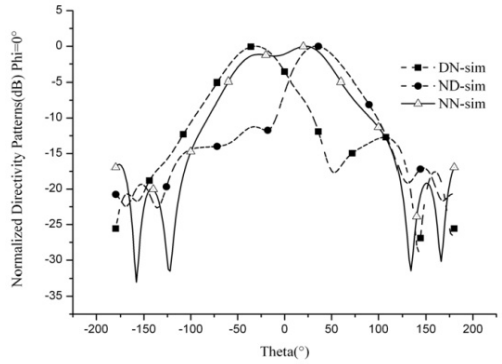

(b)

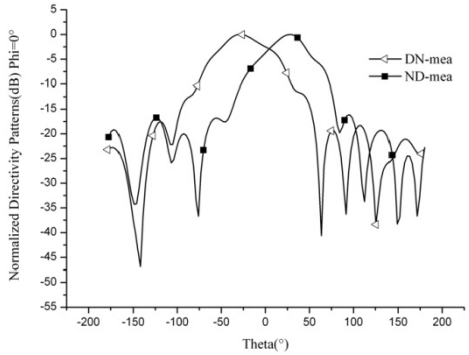

(c)

Fig. 4. S parameters and radiation patterns of three modes. (a) Simulated and measured S parameters. (b) Simulated radiation patterns in the E-plane (xoz-plane). (c) Measured radiation patterns in the E-plane (xoz-plane).

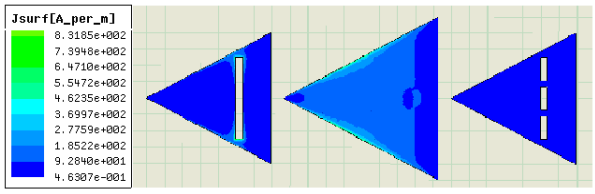

(a)

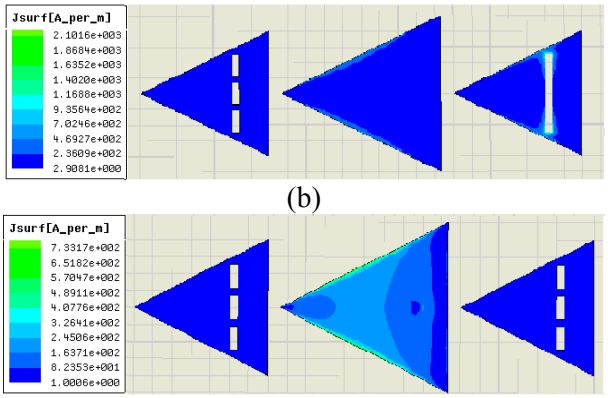

(b)

(c)

Fig. 5. current distribution at different modes. (a) Mode DN. (b) Mode ND. (c) Mode NN.

To validate the simulated results, the radiation patterns of modes DN and ND are measured as well. The measured radiation patterns are shown in Fig. 4(c). From the figure, it can be seen that the measured data coincide well with the simulated ones. The detailed data of the radiation patterns are listed in Table 1.

Table 1: Data of simulation and measurement

M	Cl	BW(GHz)	MD	HPBW
DN	Sim	10.69-11.03	-32°	-61°~-3°
	Mea	10.85-11.25	-30°	-53°~4°
ND	Sim	10.75-11.01	34°	10°~63°
	Mea	10.88-11.33	29°	5°~50°

In Table 1, M means the modes, Cl means the Classification, BW is the bandwidth, MD is maximal direction in elevation, and HPBW is the half power beamwidth in elevation.

B. RF MEMS Switches

HFSS simulations on simplified models of RF MEMS switches integrated into reconfigurable patch antennas have been implemented to examine the switches effects on the antennas [13-15]. The simulation and measurement results indicate that the RF MEMS switches have limited effect on the resonant frequency and radiation pattern. Furthermore, by modifying the antenna structure, such as the slot dimension, the reactance effect introduced by the RF MEMS switches can be eliminated [15].

The structures of a RF MEMS switch model at "ON" and "OFF" states are shown in Fig. 6. The

model consists of a microstrip line and a switch base without the metal ground. The dimensions of switch base are 1.0 mm × 1.0 mm × 0.25 mm, and are composed of silicon substrate (ε_r=11.9). The width (W) of the microstrip line is 0.05 mm, and there is a gap (S=0.05 mm) when the switch is at 'OFF' state (Fig. 6 (a)).

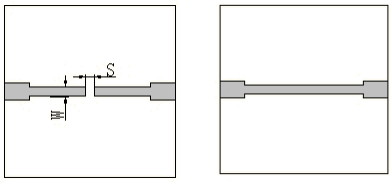

(a) (b)

Fig. 6. Simulation model of a RF MEMS switch. (a) "OFF" state. (b) "ON" state.

In order to investigate the effect of the switch size on the antenna, another MEMS model with size of 0.4 mm × 0.4 mm × 0.25 mm is used in the simulation. In addition, the length of the slot (*d*=5 mm) will be modified to fit two different sizes of switch models. When the large size model (1.0 mm×1.0 mm×0.25 mm) is used, *d* is set to 4.5 mm. When the small size model (0.4 mm × 0.4 mm × 0.25 mm) is used, *d* is 4.8 mm.

Figure 7 shows the $|S_{11}|$ and beam radiation patterns at mode DN when two different sizes of switch models are used. Switch 1 stands for the size of MEMS model of 1.0 mm×1.0 mm×0.25 mm, and Switch 2 is that of 0.4 mm×0.4 mm×0.25 mm. Compared with the simulated results of two different size switches, both S parameters and radiation patterns at mode DN coincide well with each other. Therefore, it can prove that the difference in size of RF MEMS switches has very little effect on the resonance frequency and beam patterns.

C. PIN diode switches

The PIN diode switches are also applied into the reconfigurable antennas, and some analytic methods are given in [16]. A PIN diode can be treated as an equivalent circuit shown in Fig. 8. In the HFSS simulation, the 'RLC' boundary patch often stands for a PIN diode switch model. When the PIN diode is at 'ON' state, it can be regarded as a small equivalent resistance, and when at 'OFF' state, it can be regarded as a small capacitance. By adjusting the PIN-diode equivalent capacitance on the antenna, the radiation pattern is changed. The radiation patterns of mode DN with different PIN diode capacitance are shown in Fig. 9. With the increase of capacitance, the side lobe level increases correspondingly. Therefore, the capacitance should be as small as possible.

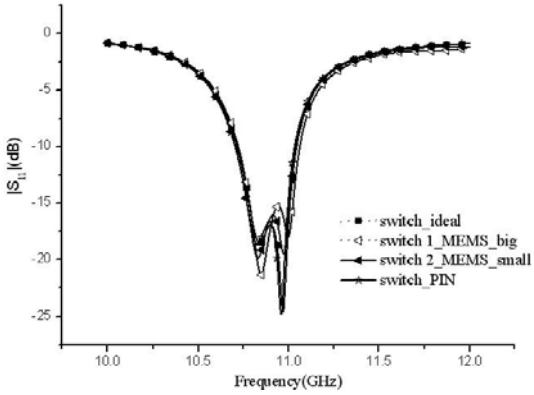

(a)

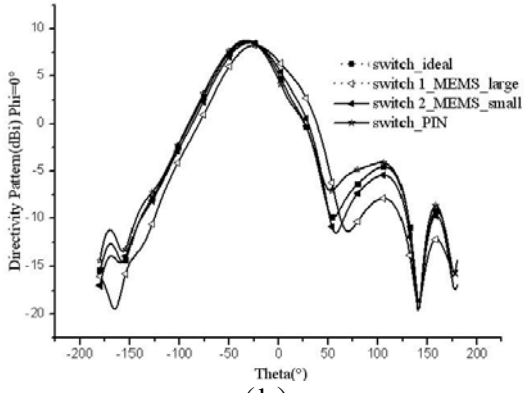

(b)

Fig. 7. S parameters and radiation patterns of ideal, MEMS and PIN switches. (a) S parameters. (b) Radiation patterns.

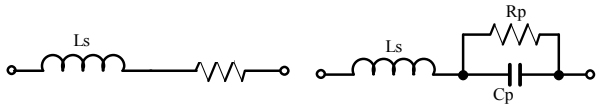

(a) (b)

Fig. 8. The equivalent circuit of the PIN diode switch. (a) 'ON' state. (b) 'OFF' state.

The MPP4203 PIN-diode has an equivalent capacitance of 0.08 pF, and the other parameters can be found in [16]. The performance of the antenna with this PIN diode used is investigated by simulation. The S parameter and radiation pattern at Mode DN are shown in Fig. 6 as well. Here, the slot length *d* is shortened from 5 mm to 4.8 mm.

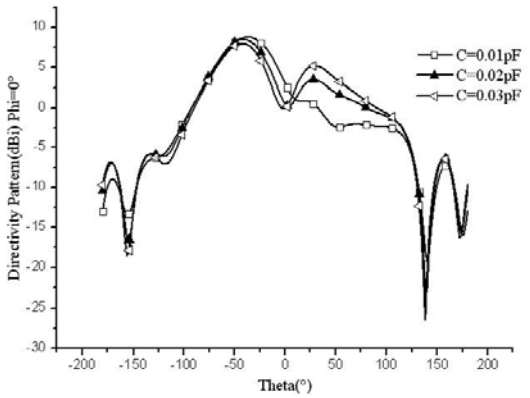

Fig. 9. Radiation patterns at mode DN with different equivalent capacitances of PIN diode switches.

It can be seen that for the results of the two RF MEMS switch models, PIN diode switch model and ideal switch model coincide very well with each other, except the modification of the slots on the parasitic patches.

However, in this simulation, the bias control circuit of the actual switches is not taken into account. For the actual switches, in order to minimize the effect of bias control circuit on the antenna, some methods must be adopted. The key is to isolate the RF signal from the DC control circuit. For example, for PIN diode switch, a low-pass filter structure can be inserted between the bias supply and the antenna. An inductive choke, which is in series with the bias line, and an RF-bypass capacitor, which is in parallel with the RF power supply output impedance, can be used to provide good RF/DC isolation [17]. Of course, with the bias control circuit installed, the impedance matching of the antenna must be tuned once again.

IV. CONCLUSION

In this paper, a novel triangular patch Yagi-Uda antenna with reconfigurable pattern characteristics is reported. Three modes of the antenna can be obtained by adjusting switches installed on the parasitic patches. The antenna can change the beam pattern and maintain the operating frequency. Pattern coverage from -61° to 63° in the E-plane in the upper half space has been shown by simulation, and the measurement results have validated the simulation ones. Compared with that reported in [11], this antenna has fewer parasitic elements, simpler structure and similar radiation beam coverage.

In the simulation, RF MEMS switches and PIN diode switches are integrated with the antenna. The simulated results show that very similar performances of the antenna can be obtained with different switches. The antenna can be used in mobile communications, satellite communications and radars, such as on aircrafts, ships and vehicle-mounted devices. In the near future, further investigation will be performed when actual switches are installed on the antenna.

ACKNOWLEDGMENT

This work was supported by the Fundamental Research Funds for the Central Universities (ZYGX2009J039) and the Natural Science Foundation of China (61271027).

REFERENCES

[1] B.-Z. Wang, S. Xiao, and J. Wang, "Reconfigurable Patch-antenna Design for Wideband Wireless Communication Systems," *IET Microwaves, Antennas and Propagation*, vol. 1, no. 2, pp. 414-419, April, 2007.

[2] H. A. Majid, M. K. A. Rahim, M. R. Hamid and M. F. Ismail, "Frequency and Pattern Reconfigurable Yagi Antenna," *Journal of Electromagnetic Waves and Applications*, vol. 26, no. 2-3, pp. 379-389, 2012.

[3] W. S. Kang, J. A. Park and Y. J. Yoon, "Simple Reconfigurable Antenna with Radiation Pattern," *Electronics Letters*, vol. 44, no. 3, pp. 182-183, Jan. 2008.

[4] Y. Yusuf and X. Gong, "A Low-cost Patch Antenna Phased Array with Analog Beam Steering using Mutual Coupling and Reactive Loading," *IEEE Antennas and Wireless Propagation Letters*, vol. 6, pp. 169-171, 2007.

[5] M. R. Islam and M. Ali, "Elevation Plane Beam Scanning of a Novel Parasitic Array Radiator Antenna for 1900 MHz Mobile Handheld Terminals," *IEEE Transactions on Antennas and Propagation*, vol. 58, no. 10, pp. 3344-3352, Oct. 2010.

[6] Z. J. Zhang, L. Jin and X. R. Shu, "Radar Antenna Technology," Publishing House of Electronics Industry, Beijing, 2007 (in Chinese).

[7] S. Xiao, Y. Y. Bai, B. Z. Wang and S. Gao, "Scan Angle Extension by Array with Pattern Reconfigurable Elements," *Applied Computational Electromagnetics Society (ACES) Journal,* vol. 24, pp. 453-457, 2009.

[8] Y. Y. Bai, S. Xiao, B. W. Wang and S. Gao, "Two-Dimensional Pattern Scanning by Linear Phased Array with Pattern Reconfigurable Elements," *Applied Computational Electromagnetics Society (ACES) Journal*, vol. 25, no. 2, pp. 144-148, February 2010.

[9] C. P. Sukumar, H. Eslami, A. M. Eltawil and B. A. Cetiner, "Link Performance Improvement using Reconfigurable Multiantenna Systems," *IEEE Antennas and Wireless Propagation Letters,* vol. 8, pp. 873-876, 2009.

[10] S. Zhang, G. H. Huff, J. Feng, and J. T. Bernhard, "A Pattern Reconfigurable Microstrip Parasitic Array," *IEEE Transactions on Antennas and Propagation*, vol. 52, no. 10, pp. 2273-2776, Oct. 2004.

[11] X.-S. Yang, B.-Z. Wang, W. Wu, and S. Xiao, "Yagi Patch Antenna with Dual-band and Pattern Reconfigurable Characteristics," *IEEE Antennas and Wireless Propagation Letters*, vol. 6, pp. 169-171, 2007.

[12] J. Huang and A. C. Densmore, "Microstrip Yagi Array Antenna for Mobile Satellite Vehicle Application," *IEEE Transactions on Antennas and Propagation*, vol. 29, pp. 1024-1030, July 1991.

[13] G. H. Huff and J. T. Bernhard, "Integration of Packaged RF MEMS Switches with Radiation Pattern Reconfigurable Square Spiral Microstrip Antennas," *IEEE Transactions on Antennas and Propagation*, vol. 54, no. 2, pp. 464-469, Feb. 2006.

[14] H. Rajagopalan, Y. Rahmat-Samii, and W. A. Imbriale, "RF MEMS Actuated Reconfigurable Reflectarray Patch-slot Element," *IEEE Transactions on Antennas and Propagation*, vol. 56, no. 12, pp. 3689-3699, Dec. 2008.

[15] X.-S. Yang, B.-Z. Wang, S. H. Yeung, Q. Xue, and K. F. Man, "Circularly Polarized Reconfigurable Crossing Yagi Patch Antenna," *IEEE Antennas and Propagation Magazine,* vol. 53, no. 5, pp. 65-80, 2011.

[16] J. H. Lim, G. T. Back, Y. I. Ko, C. W. Song, and T. Y. Yun, "A Reconfigurable PIFA using a Switchable PIN-diode and a Fine-tuning Varactor for USPCS/WCDMA/m-WIMAX/WLAN," *IEEE Transactions on Antennas and Propagation,* vol. 58, no. 7, pp. 2404-2411, July 2010.

[17] Microsemi-Watertown, "The PIN Diode Circuit Designers' Handbook," pp. 7, 1992.

Jian Zhang received the B. Sc. degree in Electronic Information Science and Technology from UESTC, Chengdu, China, in 2009. He is currently working toward the M. Sc. Degree in UESTC. His current research interests include reconfigurable antennas and arrays.

Xue-Song Yang received the B. Eng. degree in Applied Electronic Technology from Huazhong University of Science and Technology (HUST), Wuhan, China, and the Ph.D. degree in Radio Physics from UESTC, Chengdu, China.

She joined the UESTC in 2002, where she is currently an associate professor. From Jan. 2007 to July 2008, she was a senior research associate and then a research fellow at the City University of Hong Kong. From Dec. 2009 to Dec. 2010, she was a Visiting Scholar at the University of Southern California, USA. Her current research interests include reconfigurable antennas, UWB antennas, MIMO antennas, and wireless communications channel modeling.

Jia-Lin Li received the M. Sc. degree from UESTC, Chengdu, China, in 2004, and the Ph. D. degree from the City University of Hong Kong, Hong Kong, in 2009, both in electronic engineering. Since Sept. 2009, he has been with the Institute of Applied Physics, School of Physical Electronics, UESTC, where he is currently a Professor. His research interests include the high performance active/passive microwave/millimeter-wave antennas, circuits and systems realized on PCB, multilayer PCB, LTCC, etc.

Bing-Zhong Wang received the Ph.D. degree in electrical engineering from UESTC, Chengdu, China, in 1988.

He joined the UESTC in 1984 and is currently a Professor there. He has been a Visiting Scholar at the University of Wisconsin-Milwaukee, a Research Fellow at the City University of Hong Kong, and a Visiting Professor in the Electromagnetic Communication Laboratory, Pennsylvania State University. His current research interests are in the areas of computational electromagnetics, antenna theory, and computer-aided design for microwave circuits.

Directivity and Bandwidth Enhancement of Proximity-Coupled Microstrip Antenna Using Metamaterial Cover

Mehdi Veysi[1], and Amir Jafargholi[2]

[1]Department of Electrical Engineering
K. N. Toosi University of Technology, P.O.Box 16315-1355. Tehran, Iran
veysi@ee.kntu.ac.ir

[2]Institute of Space Science and Technology
Amirkabir University of Technology, 424 Hafez Ave., P.O. Box: 15875-4413, Tehran, Iran
jafargholi@ieee.org

Abstract ─ Two major problems associated with patch antennas are low gain and narrow bandwidth. This paper is mainly concerned with directivity and bandwidth enhancement of proximity-coupled microstrip antenna using metamaterial cover. Compared to the patch without metamaterial cover, bandwidth of the antenna is improved about 2.33% and directivity is increased about 9.91dB. The commercial software CST Microwave Studio and a full-wave FDTD numerical technique, developed by the authors, are adopted for the simulations.

Index Terms ─ Metamaterial cover, FDTD.

I. INTRODUCTION

Directive patch antennas are very popular in electromagnetic community. Their attractive features, such as low profile, light weight, low cost and compatibility with MMICs, do not exist in other antennas. Two distinctive types of directive antennas are parabolic antennas and large array antennas. Bulk and curved surface of parabolic antennas limits their use in many commercial applications. Also, complex feeding mechanism and loss in the feeding network are two major disadvantages associated with microstrip array antennas [1]. One solution to these problems is to use metamaterial cover over the patch antenna [2-5]. One of the first works was done by B. Temelkuaran in 2000, [6]. In 2002, S. Enoch proposed a kind of metamaterial for directive emission, [7]. Another problem associated with microstrip antennas is their narrow bandwidth. The previous works so far [3-5] have dealt only with the enhancement of the antenna directivity using metamaterial cover, but the effect of this cover on the antenna input impedance has not been investigated. Recently, a new metamaterial cover has been proposed to enhance both the antenna bandwidth and directivity, [8]. But, its directivity is significantly lower compared to the primary metamaterial cover, [2-5]. In this paper, we have demonstrated that both the antenna impedance bandwidth and directivity can be enhanced using the metamaterial cover over the proximity-coupled patch antenna. It is known that proximity-coupled patch antennas are sensitive to the transverse feed point location. In this paper, a parasitic microstrip line has been used on the opposite side of the feed line to mitigate this drawback. Our new configuration not only increases the antenna directivity from 6.25dB to 16.16dB (at the center frequency), but also increases the impedance bandwidth of the patch antenna from 2.9% to 5.23%. In this paper, we first investigate the impedance bandwidth of the antenna using its resonant frequencies and then examine 3dB directivity bandwidth of the proposed antenna.

II. METAMATERIAL DESIGN

A schematic of the metamaterial cover is shown in Fig. 1. It consists of two planar layers with similar square lattices. It was demonstrated in

Submitted On: March 14, 2012
Accepted On: August 22, 2012

[9-10] that in the frequency range, where the wavelength is very large compared to the period of the periodic cover, this structure acts as a homogenous medium whose equivalent refractive index in the microwave domain is given by

$$n_{eff} = \sqrt{1 - \left(f_P / f \right)^2} \tag{1}$$

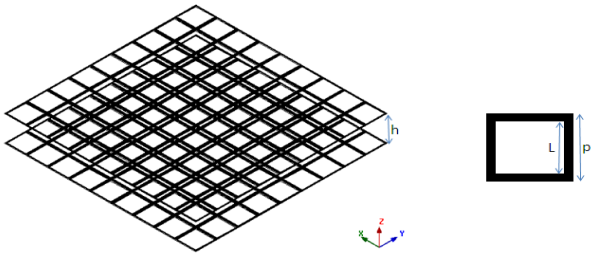

Fig. 1. Schematic view of two-layer metamaterial cover.

Where f_P denotes the plasma frequency and f denotes the operating frequency. If the operating frequency is selected slightly larger than the natural plasma frequency, the equivalent refractive index will be extremely low. Consequently, the transmission phase at the plasma frequency is extremely low [2]. The ultra refraction phenomena can be expected where the transmission coefficient reaches its maximum value [2, 7]. In other words, the zero transmission phase occurs at the same frequencies where the magnitude of the transmission coefficient becomes maximum. Hence, it acts similar to an equally phase surface at its plasma frequency [2]. It is evident from Equ.1, that the equivalent refractive index and thus the antenna directivity are very sensitive to the frequency.

However, these significant changes in the antenna directivity with respect to the frequency represent the potential challenges in the design and application of these metamaterial superstrates in antenna engineering. The transmission characteristic of the metamaterial cover has been investigated, without the ground plane and without the antenna, using FDTD code developed by the authors. Its effective unit cell model is shown in Fig. 2. The normalization in the code consists of choosing the peak magnitude of the transmission coefficient to be unity. Therefore, the magnitude of the transmitted field from the metamaterial cover has been normalized to that without the metamaterial cover. We have used the same methodology applied in the measurements [7]. Since an infinite periodic structure has been simulated, the peak magnitude of the transmission coefficient is unity, unlike the results obtained in the measurements [7]. The dimensions of the analyzed metamaterial cover are:

P=0.41λ_{6GHz}, t = 0.01 λ_{6GHz}, L= 0.31λ_{6GHz}, h=0.49λ_{6GHz}

Where λ_{6GHz} (50mm) denotes the free space wavelength at 6GHz, P is the periodicity, t is the thickness of the metallic grids, L is the edge of the square holes and h is the distance between the two sheets which is the same as the distance between the patch antenna and the first sheet. In the FDTD simulations, a uniform 0.01λ_{6GHz} grid size is used. The resulting transmission curve is also plotted in Fig. 3.

As can be seen, this structure possesses three microwave plasma frequencies at about 5GHz, 5.81GHz and 8.1GHz which make it suitable for the antenna applications. When the aforementioned metamaterial based cover is placed over the conventional proximity-coupled patch antenna, the final metamaterial antenna can be approximated by a homogenous medium terminated in a ground plane, [9-10].

This approximation is similar to that used for the transmission coefficient calculations, as used also by other authors [3, 5, 7]. It is a simple matter to obtain the surface impedance of this grounded slab as a function of metamaterial parameters. A surface impedance of the grounded slab of thickness h is:

$$Z_s = j\eta \tan\left(2\pi h / \lambda\right) \tag{2}$$

Where η and λ are the wave impedance and wavelength in the slab, respectively. For the extremely low value of ε_{eff} the surface impedance is very low and inductive. In addition, the inductive reactance is $X_l = j\omega L$. For equivalence we can equate them, leading to the following equation:

$$j\omega L = j\eta \tan\left(2\pi h / \lambda\right) \tag{3}$$

Since $\varepsilon_{eff} << 1$, we can apply the small-angle

approximation, so that above equation then becomes $L=\mu_0 h$. Consequently, the operation mechanism of this metamaterial based cover can be explained using this equivalent inductance. In addition, coupling between the feed line and the patch antenna is totally capacitive [1]. And thus, one can expect another resonant frequency due to the reactive cancellation between the capacitive feeding structure and the inductive metamaterial cover. Consequently, an appropriate selection of the coupling capacitor value can result in a broadband operation.

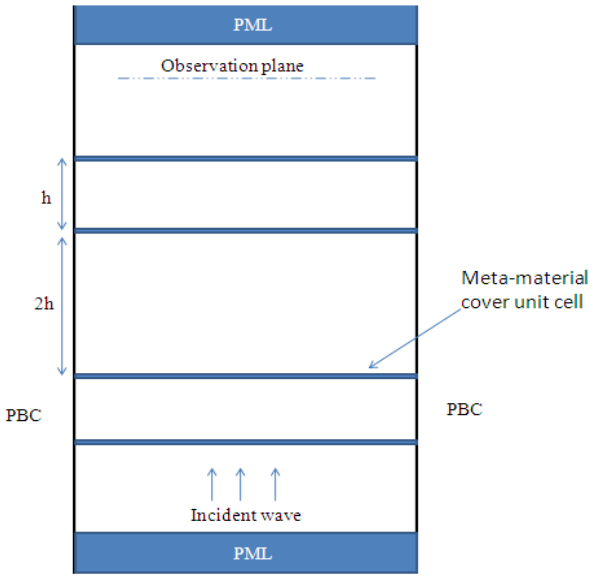

Fig. 2. FDTD model for transmission band selection of a metamaterial cover.

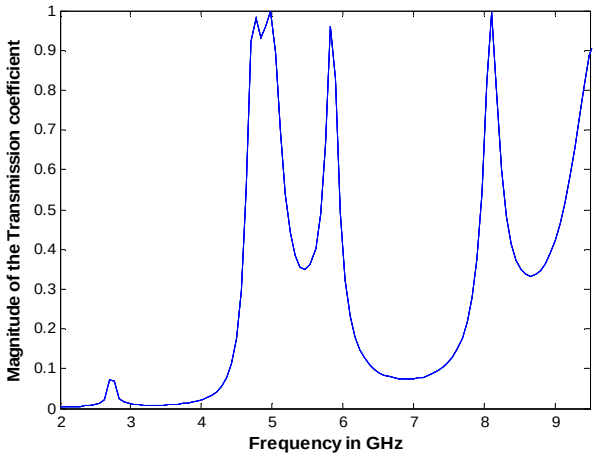

Fig. 3. FDTD simulated transmission of metamaterial cover.

III. ANTENNA CONFIGURATION AND SIMULATION RESULTS

For the purpose of realization, the metamaterial cover described in the previous section is placed over the conventional proximity-coupled patch antenna. A schematic of proposed metamaterial patch antenna is shown in Fig. 4. In general, the two dielectrics can be of different thicknesses and relative permittivity, but here both dielectrics are 30mil (h_1=h_2= 0.762mm) Duroid with, ε_r= 2.2. For the case discussed here, the patch of the antenna is rectangular with 12.45mm width and 16mm length. The distance between the main microstrip line and the parasitic line is also 7mm. Each metamaterial cover composed of 9×9 unit cells, as shown in Fig. 4. Consequently, the total size of the dielectric substrate and the metamaterial cover is 184.5mm×184.5mm. Furthermore, the working frequency of the conventional patch antenna is selected at 5.9GHz.

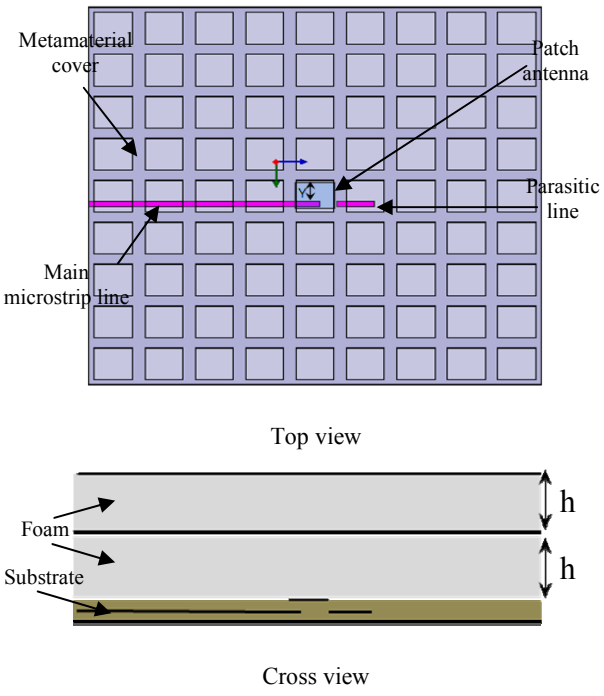

Fig. 4. Geometry of a metamaterial proximity-coupled patch antenna: Y=9mm.

Return loss of the proposed metamaterial patch antenna has been simulated and was compared to the one obtained for the conventional proximity-coupled patch antenna in Fig. 5. As revealed in the figure, the antenna return loss is significantly

improved compared to the reference patch antenna without the metamaterial cover. The impedance bandwidth of the patch antenna is increased from 2.9% to 5.23% (ranging from 5.649GHz to 5.952GHz). Using the usual formulas mentioned in [1], the conventional proximity-coupled patch antenna discussed here possesses a TM_{01} mode resonant frequency of approximately 5.9GHz. The second resonant frequency of the metamaterial patch antenna is obviously due to the TM_{01} mode of the conventional patch antenna. (See Fig. 5) Since the metamaterial superstrate disturbs the current distribution of the TM_{01} mode, this resonant frequency slightly shifts down to a lower frequency. An interested reader is recommended to refer to [11] for more details. The first resonant frequency is the result of reactive cancellation between the capacitive feeding structure and the inductive metamaterial cover. On the other hand, the first resonant frequency is close to the second resonant frequency, which results in broadband operation. The simulation results of Fig. 5 are in good agreement with the theoretical predictions discussed in the last paragraph of the previous section, which serve to justify the approximations that were used to model the metamaterial patch antenna as a grounded homogenous medium. It is necessary to mention that the parasitic line section, used on the opposite side of the feed line, stabilizes the antenna performance at its resonant frequency at the expense of an additional resonance frequency at about 6.24GHz. A detailed discussion on that will be presented in a future work.

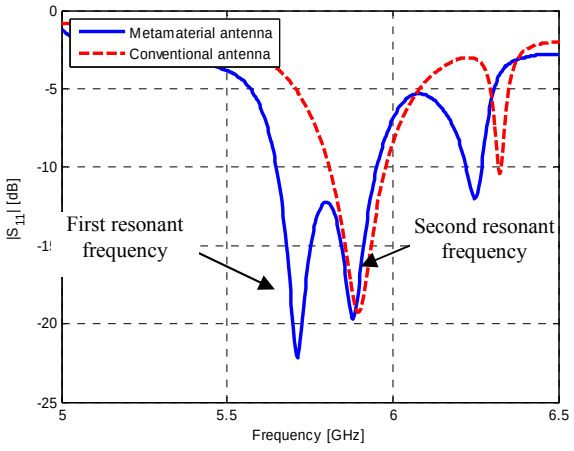

Fig. 5. Simulated return loss versus frequency.

By using the metamaterial cover over the patch antenna, the antenna radiation patterns in E- and H-planes are concentrated in a direction perpendicular to the patch antenna (θ=0).

The simulated broadside directivity versus frequency is shown in Fig. 6. As can be seen, the maximum directivity of the patch antenna is increased from 6.25dB to16.16dB using metamaterial cover. The 3dB directivity bandwidth of the metamaterial antenna is also between 5.685GHz and 5.91GHz, or 3.88%.

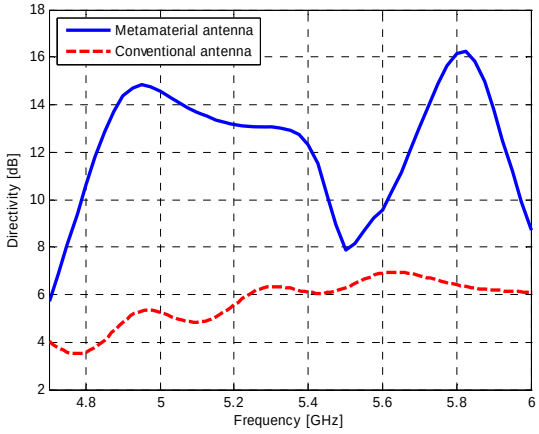

Fig. 6. Simulated broadside directivity versus frequency.

The antenna radiation patterns within its bandwidth are also investigated. The E-plane and H-plane patterns of the metamaterial patch antenna at three frequencies (5.7GHz, 5.8GHz and 5.9GHz) have been simulated and were compared to the one obtained for the conventional antenna, at 5.9GHz, in Fig. 7. Although the radiation pattern of the metamaterial antenna changes a bit at each frequency, the main lobe of the metamaterial antenna at all frequencies (ranging from 5.65 to 5.95GHz) is in the broadside direction and maximum directivity is reasonably good. In the present case, the area of the aperture is A=184.5mm×184.5mm, and $\lambda=c_0/f_0$= 51.724mm, so that maximum directivity then becomes D_{max}= 22dB. The maximum directivity of the metamaterial patch antenna, occurring at 5.81GHz, (16.16dB) has approached the maximal directivity obtained, theoretically, with the same aperture size. In addition, we have investigated the effect of parasitic strip on the antenna return loss.

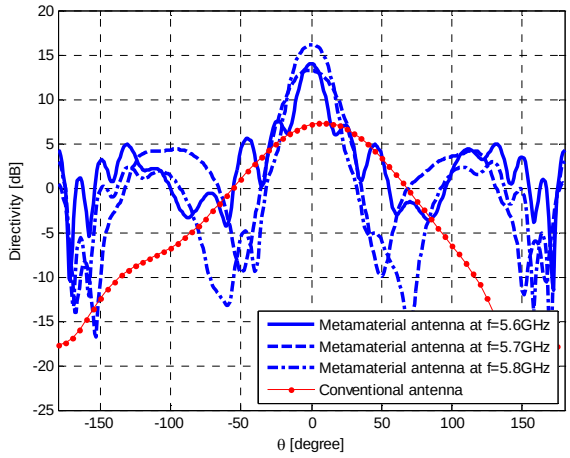

(a)

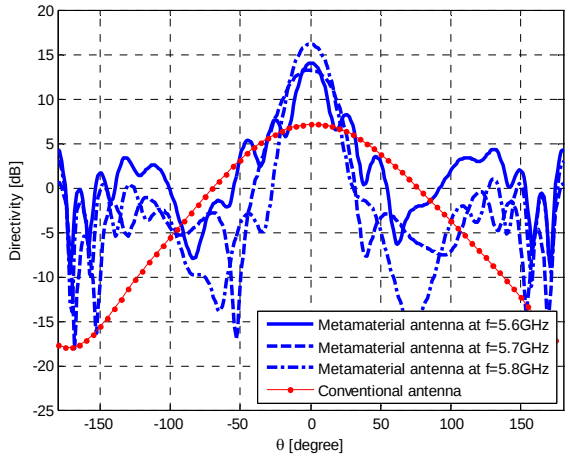

(b)

Fig. 7. CST simulated radiation patterns at different frequencies over the operating bandwidth, (a) E-plane, and (b) H-plane.

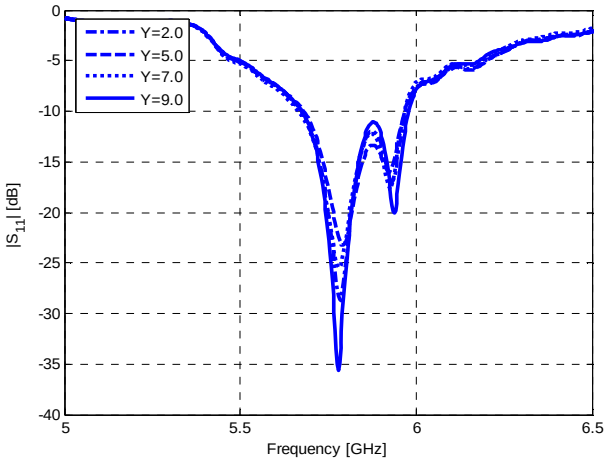

Fig. 8. Return loss of the metamaterial antenna v.s. frequency for the different feed point locations (Y in mm).

Consequently, the transverse feed point location is changed from one side of the metamaterial patch antenna to the other side. The antenna return loss versus frequency is shown for the different values of Y in Fig. 8. As can be seen, displacement of the feed point location does not have a considerable effect on the antenna input impedance and bandwidth, [13].

IV. CONCLUSION

A new metamaterial proximity coupled-patch antenna has been proposed, which is not sensitive to the transverse feed point location. A full-wave FDTD numerical method has been developed for designing and characterizing metamaterial cover. Proximity-coupled patch antenna has been designed and simulated to demonstrate the potential application of this metamaterial cover. Compared to the conventional design both the antenna impedance bandwidth and directivity increase about 2.33% and 9.91dB, respectively. The 3dB directivity bandwidth of the proposed metamaterial patch antenna is about 3.88%. Furthermore, the antenna bandwidth can be also increased by tuning the length of the parasitic strip.

REFERENCES

[1] R. Garg, P. Bhartia, I. Bahl, A. Ittipiboon, *Microstrip Antenna Design Handbook*, Artech House, 2001.

[2] A. Alù, F. Bilotti, N. Engheta and L. Vegni "Metamaterial Covers Over a Small Aperture," *IEEE Trans. Antennas Propag.*, vol. AP-54, no. 6, pp. 1632-1643, June 2006.

[3] H. Xu, Z. Zhao, Y. Lv, C. Du and X. Luo, "Metamaterial Superstrate and Electromagnetic Band-Gap Substrate for High Directive Antenna," *Int J Infrared Milli Waves*, vol. 29, pp. 493-498, 2008.

[4] M. Tang, S. Xiao, D. Wang, J. Xiong, K. Chen, B. Wang, "Negative Index of Reflection in Planar Metamaterial Composed of Single Split-Ring Resonators," *Applied Computational Electromagnetics Society (ACES) Journal*, vol. 26, no. 3, pp. 250-258, March 2011.

[5] C. Huang, Z. Zhao, W. Wang and X. Luo "Dual Band Dual Polarization Directive Patch Antenna Using Rectangular Metallic Grids Metamaterial," *J Infrared Milli Terahz Waves*, vol. 30, pp. 700-708, 2009.

[6] B. Temelkuaran, M. Bayindir, E. Ozbay, R. Biswas, M. Sigalas, G. Tuttle, and K. M. Ho,

"Photonic Crystal-Based Resonant Antenna with a Very High Directivity," *Journal of Applied Physics* 87, pp. 603-605, 2000.

[7] S. Enoch, G. Tayeb , P. Sabouroux, N. Guérin, and P. Vincent, "A Metamaterial for Directive Emission," *Physical Review Letters* 89, 213902, 2002.

[8] J. Ju, D. kim, W. J. Lee, and J. I. Choi "Wideband High-Gain Antenna Using Metamaterial Superstrate with the Zero Refractive Index," *Microwave and Optical Tech. Lett.*, vol. 51, no. 8, pp. 1973-1976, 2009.

[9] J. B. Pendry, A. J. Holden, W. J. Stewart, and I. Youngs, "Extremely Low Frequency Plasmas in Metallic Mesostructures," *Physical Review Letters* vol. 76, pp. 4773-4776, 1996.

[10] C. H. Tsao and J. L. Chern, "Field Propagation of a Metallic Grid Slab That Act As A Metamaterial," *Physics Letters A* 353, pp. 171-178, 2006.

[11] Zhong, S.-S., G. Liu, and G. Qasim, "Closed Form Expressions for Resonant Frequency of Rectangular Patch Antennas with Multidielectric Layers," *IEEE Trans. Antennas Propag.*, vol. Ap-42, pp. 1360-1363, 1994.

[12] C. Balanis, *Antenna Theory Analysis and Design*, Wiley, 2005.

[13] A. Jafargholi, M. Kamyab, M. Veysi, and M. Nikfal Azar, "Microstrip Gap Proximity Fed-Patch Antennas, Analysis, and Design," *International Journal of Electronics and Communications*, *(AEÜ),* vol. 66, pp. 115-121, 2012.

Mehdi Veysi received the B.S. degree in biomedical engineering from the Isfahan University, Isfahan, Iran, in 2007 and the M.S. degree (ranked 1st) in electrical engineering from the K. N. Toosi University of Technology, Tehran, Iran, in 2010. He has authored or coauthored more than 13 journal articles and one conference paper. Mr. Veysi was a recipient of the "distinguished researcher award" during 2010-2011. He has been engaged in various research works on development of satellite-born antenna such as shaped-beam parabolic reflectors and reflectarrays.

Amir Jafargholi received the PhD degree in electrical engineering from K.N. Toosi University of Technology, Tehran, Iran, in 2011. He is the coauthor of about 50 scientific contributions published in international books, journals and peer-reviewed conference proceedings. His research interest includes the applications of metamaterials in the analysis and synthesis of antennas.

Dr. Jafargholi was a recipient of a Student's Best Thesis National Festival award for his BS thesis, on May 2006. He was a recipient of the 22th Khawarizmi International and 13th Khawarizmi Youth Award on Jan. 2009 and Oct. 2011, respectively. He was also the recipient of Research Grant Awarded in Metamaterial 2010.

Ultrawide band Negative Refraction Based on Moving Media Concept

Amir Jafargholi[1] and Ali Jafargholi[2]

[1]Institute of Space Science and Technology
Amirkabir University of Technology, 424 Hafez Ave., P.O. Box: 15875-4413, Tehran, Iran
jafargholi@ieee.org

[2]Department of Electrical Engineering
Sharif University of Technology, Azadi Ave., P.O. Box: 11365-11155, Tehran, Iran
jafargholi@sharif.edu

Abstract ─ The anomalous wave propagation in a homogeneous, isotropic and lossless medium that moves with a constant velocity along the axis of a rectangular waveguide; and its interesting properties lead us to the fact that the moving media may be regarded as double negative metamaterial (DNG). In this paper, the correct sign of the permittivity and permeability of an equivalent stationary media, for each TE and TM modes and for both low and high dielectric velocities are investigated and it is shown that this medium acts as a DNG material over specific frequency ranges.

Index Terms ─ Moving Media, Metamaterial.

I. INTRODUCTION

Theory of negative index was first introduced by Veselago [1]. He showed in his theoretical investigations that the DNG material has negative refraction property. After works of Rotman [2], Pendry [3], and Smith [4], a standard procedure was established for the design of bulk artificial media with negative parameters. Negative refraction has been realized in artificial structures which is made of wires and SRRs [5], photonic crystals [6] and discrete elements [7], hole arrays in thin metal films [8], thin layers of dielectrics [9], vertical loops on a substrate [10], waveguide arrangements [11], and even a natural material based on colossal magnetoresistance [12]. The narrow bandwidth of aforementioned proposed artificial materials is due to resonant nature of these structures and this fact is main limiting factor for negative refraction applications.

In this paper it will be shown that some of the drawbacks might be overcome, by using other types of artificial structures which would have a larger bandwidth, such as moving media. Though moving media, [13-14] have been previously categorized in the bianisotropic groups, the proposed media can also be considered as artificial negative refractive structures. Moreover, similar to SRR the proposed media show DNG properties just in certain directions [3]. In contrast to SRR structures showing resonance and narrow-band DNG properties, the proposed moving media have wide bandwidth which meets the law of entropy.

Recently, Grzegorczyk et al studied the wave refraction phenomenon as a function of frequency and medium velocity in an isotropic non-dispersive moving medium which its velocity is parallel to the interface where refraction occurs, using spectral domain approach [15]. They investigated the effects of motion of the medium on a rotation of refraction. They showed that it can either enhance or attenuate the natural negative refraction of the medium. However, it should be emphasized that our approach is fundamentally different with [15] in three aspects: it involves permittivity and permeability definition of an equivalent stationary media based on moving medium parameters, negative refraction is obtained for both TE and TM modes for each frequency range, and we consider that the

Submitted On: May 9, 2012
Accepted On: August 22, 2012

direction of medium movement to be in the same direction of wave propagation.

In this paper, we consider stationary medium with equivalent permittivity and permeability for both TE and TM waveguide modes. The range of validity for each quantity is clearly stated. It has been demonstrated that this media acts as an ultrawide band negative refractive structure. It is to be noted that treatment of this issue at present is purely theoretical, however developing waveguide which filling medium with specified physical constituent moving with constant velocity may not be impossible in future, however, the applications of metamaterial in waveguide have been already addressed in literatures, [16]-[18-19].

II. QUANTITIES DEFINITIONS

The moving media are not a new concept in electromagnetic and it has been discussed in [13-14]. In [13], it has been showed that for a general moving media, the cutoff frequency of ordinary waveguide is lowered by a factor which depends upon the velocity of the medium. It has been also shown that change in the cutoff frequency, propagation constant and transverse-wave impedance are modified independent of the guide geometry.

In [14], Du and Compton showed that for a slowly moving medium, $n\bar{v}<1$, where n is the index of refraction and v is the velocity of the medium, $\bar{v}$, divided by the velocity of light in vacuum, there are two critical frequencies, separating three frequency ranges in each of which there is a different type of propagation. Furthermore, for a high-speed medium i.e. $n\bar{v}>1$, it is found that there is no cutoff phenomenon at all, although there is one critical frequency separating two frequency ranges in which the propagation is different.

In Fig. 1, the anomalous properties of this medium are shown, [14]. We assume that a homogeneous, isotropic and lossless media that moves with a constant velocity along the axis of a waveguide acts as an equivalent medium to a rectangular waveguide which is filled with stationary media and modified permittivity and permeability. First, we define the main quantities of such equivalent rectangular waveguide compared with same quantities of moving media. Then, the restrictions on the range of validity of derived quantities are specified, and finally the correct sign of equivalent permittivity, ε_e, and permeability, μ_e, of moving media will be determined. In a dielectric loaded rectangular waveguide the cutoff frequency, f_c, is,

$$f_c = \frac{k_c}{2\pi\sqrt{\mu\varepsilon}} = \frac{k_c}{2\pi n} \tag{1}$$

where k_c is, in general, a different propagation constant for each mode (i.e. for a rectangular waveguide $k_c^2 = \left(\frac{p\pi}{a}\right)^2 + \left(\frac{q\pi}{b}\right)^2$ .where a and b are the dimensions of the waveguide, and p, q specify the mode) and,

$$n = \sqrt{\mu\varepsilon} = \sqrt{\mu_r\varepsilon_r}\cdot\sqrt{\mu_0\varepsilon_0} \tag{2}$$

which in this equation, ε_r and μ_r are the dielectric permittivity and permeability respectively. And the wave impedance of TE and TM modes are equal to

$$Z^{TE} = \frac{\omega\mu_r}{\beta_r} \tag{3}$$

$$Z^{TM} = \frac{\beta_r}{\omega\varepsilon_r} \tag{4}$$

where $\beta_r = \omega\sqrt{\mu_r\varepsilon_r}$ is the propagation constant.

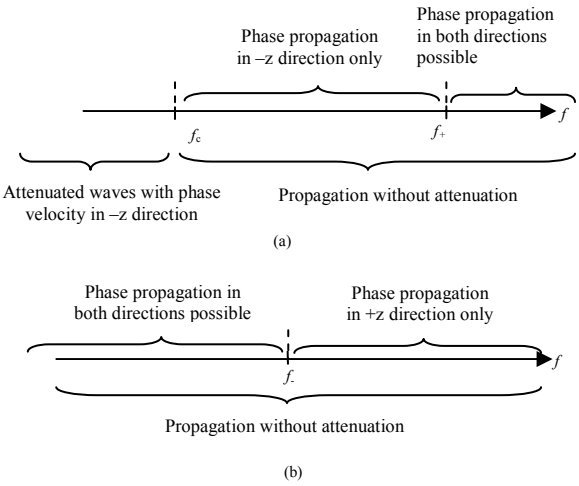

Fig. 1. Frequency ranges for wave propagation in the waveguide, with the medium moving in the +Z direction, (a) the low velocity case: $n\bar{v}<1$. (b) the high velocity case: $n\bar{v}>1$, [14].

Now, for an equivalent medium which is filled with stationary media and modified permittivity, ε_e, permeability, μ_e ; propagation constant, β_e, and comparing (3) and (4) with TE and TM impedance of moving media, based on [14], one can show that [17]

$$Z^{TE} \Rightarrow \frac{\omega\mu_e}{\beta_e} \equiv \frac{\omega\mu a}{h+\omega\Omega} \tag{5}$$

$$Z^{TM} \Rightarrow \frac{\beta_e}{\omega\varepsilon_e} \equiv \frac{h+\omega\Omega}{\omega\varepsilon a} \tag{6}$$

Where ε and μ are the permittivity and permeability of the moving material in rectangular waveguide, and a and Ω are defined as

$$\Omega = \frac{\left(n^2-1\right)\bar{v}}{\left(1-n^2\bar{v}^2\right)c} \tag{7}$$

$$a = \frac{1-\bar{v}^2}{1-n^2\bar{v}^2} \tag{8}$$

Here, $h = -\omega\Omega \pm a\sqrt{k^2-k_c^2}$ and c is the velocity of light.

$$\bar{v} = \frac{v}{c} \tag{9}$$

From equations (5) and (6), we have

$$\frac{\mu_e}{\varepsilon_e} = \frac{\mu_r}{\varepsilon_r} \rightarrow \mu_e = \frac{\mu_r}{\varepsilon_r}\varepsilon_e \tag{10}$$

Using (10) and (2), we get

$$n_e = \sqrt{\mu_e\varepsilon_e} = \left|\varepsilon_e\right|\sqrt{\frac{\mu_r}{\varepsilon_r}} = \left|\mu_e\right|\sqrt{\frac{\varepsilon_r}{\mu_r}} \tag{11}$$

The modal impedances of an ordinary rectangular waveguide depend on the modal indexes. As it mentioned before, in [13-14] it has been shown that for a general moving media, the transverse-wave impedance are modified independent on the guide geometry. Hence in the equivalent medium, it is expected that the equivalent transverse-wave impedance is independent from the modal indexes and it related to the velocity of the moving medium.

III. CRITICAL FREQUENCIES

As stated earlier we assume that a rectangular waveguide which is filled with stationary media and modified permittivity and permeability acts as an equivalent medium to a homogeneous, isotropic and lossless media that moves with a constant velocity along the axis of a waveguide.

When the velocity of the moving medium is small, i.e. $n\bar{v} < 1$, the cutoff frequency is [14],

$$f = f_c = \frac{k_c}{2\pi\sqrt{\mu_0\varepsilon_0}} \cdot \sqrt{\frac{1-n^2\bar{v}^2}{n^2\left(1-\bar{v}^2\right)}} \tag{12}$$

Comparing (1) and (12) it is evident that for frequencies below the cutoff frequency

$$f < f_c \Rightarrow \frac{1}{\sqrt{\mu_e\varepsilon_e}} < \sqrt{\frac{1-n^2\bar{v}^2}{n^2\left(1-\bar{v}^2\right)}} \tag{13}$$

or

$$n_e > \sqrt{\frac{n^2\left(1-\bar{v}^2\right)}{1-n^2\bar{v}^2}} \tag{14}$$

Using (11), (14) can be written as

$$n_e = \left|\varepsilon_e\right|\sqrt{\frac{\mu_r}{\varepsilon_r}} > \sqrt{\frac{n^2\left(1-\bar{v}^2\right)}{1-n^2\bar{v}^2}} \tag{15}$$

Combination of (2) and (15) leads to the following inequalities for small values of velocity

$$\varepsilon_e > \varepsilon_r\sqrt{\frac{1-\bar{v}^2}{1-n^2\bar{v}^2}} \tag{16}$$

or

$$\varepsilon_e < -\varepsilon_r\sqrt{\frac{1-\bar{v}^2}{1-n^2\bar{v}^2}} \tag{17}$$

Waveguide impedances for TE and TM modes are, [14]

$$Z^{TE} = \mp i\frac{\omega}{\omega_C}\eta \cdot \left[1-\left(\frac{f}{f_C}\right)^2\right]^{-1/2} \tag{18}$$

$$Z^{TM} = \pm i\frac{\omega_C}{\omega}\eta \cdot \left[1-\left(\frac{f}{f_C}\right)^2\right]^{1/2} \tag{19}$$

Where, η is the intrinsic impedance of medium.

By comparing (18) and (19) with (3) and (4) respectively, the correct sign for the permittivity can be determined. For TE mode, the equivalent permittivity and permeability in +z direction are negative, whereas for -z direction, they are positive. Similarly, for TM mode, the equivalent permittivity and permeability in +z and -z directions are positive and negative, respectively. When the frequency is less than f_c, the fields are attenuated along the guide axis, but unlike an ordinary waveguide below cutoff, there is a phase velocity $v_P = 1/\Omega$ in the negative z-direction for both solutions, [14]. Based on what stated, one may conclude that the moving media acts as DNG and double positive (DPS) for TM and TE respectively.

When the frequency is slightly above f_c, there is no attenuation, but the two waves both have different phase velocities in the negative z-direction. For large enough frequency we have from [14]

$$f_+ = \frac{k_c}{2\pi\sqrt{\mu_0\varepsilon_0}} \cdot \sqrt{\frac{1-\bar{v}^2}{n^2-\bar{v}^2}} \tag{20}$$

This means that the waves can propagate in either direction without attenuation, but again with different phase velocities. For frequency above f_+, we have

$$\frac{1}{n_e} > \frac{1}{\sqrt{\mu_r\varepsilon_r}} = \frac{1}{n} \rightarrow n_e < n \tag{21}$$

Using (11), (21) can be written as

$$|\varepsilon_e| < \varepsilon_r \Rightarrow -\varepsilon_r < \varepsilon_e < \varepsilon_r \tag{22}$$

Equ. (22) shows that it is possible to have negative and positive values for permitivity. With the following wave impedances defined in [14]

$$Z^{TE} = \pm\eta \cdot \left[1 - \left(\frac{f_C}{f}\right)^2\right]^{-1/2} \tag{23}$$

$$Z^{TM} = \pm\eta \cdot \left[1 - \left(\frac{f_C}{f}\right)^2\right]^{1/2} \tag{24}$$

We note that both TE and TM waves in +z and -z directions can exist and equivalent permittivity and permeability are positive for +z direction and negative for -z direction.

For frequency $f_c < f < f_+$, one can show that

$$f_c < f < f_+ \Rightarrow \begin{cases} n_e > n \\ n_e < \sqrt{\dfrac{n^2\left(1-\bar{v}^2\right)}{1-n^2\bar{v}^2}} \end{cases} \tag{25}$$

This condition leads to

$$\begin{cases} n_e > n \\ n_e < \sqrt{\dfrac{n^2\left(1-\bar{v}^2\right)}{1-n^2\bar{v}^2}} \end{cases} \Rightarrow \begin{cases} |\varepsilon_e| > \varepsilon_r \\ |\varepsilon_e| < \varepsilon_r\sqrt{\dfrac{1-\bar{v}^2}{1-n^2\bar{v}^2}} \end{cases} \tag{26}$$

From which we have

$$\begin{cases} \varepsilon_e < -\varepsilon_r \ , \ \varepsilon_e > \varepsilon_r \\ -\varepsilon_r\sqrt{\dfrac{1-\bar{v}^2}{1-n^2\bar{v}^2}} < \varepsilon_e < \varepsilon_r\sqrt{\dfrac{1-\bar{v}^2}{1-n^2\bar{v}^2}} \end{cases} \tag{27}$$

Again defining of ψ as

$$\psi = \sqrt{\frac{1-\bar{v}^2}{1-n^2\bar{v}^2}} \tag{28}$$

The second inequality in (27) can be expressed

$$\begin{cases} if \quad n^2 < 1 \rightarrow \psi < 1 \\ if \quad n^2 > 1 \rightarrow \psi > 1 \end{cases} \Rightarrow \begin{cases} \varepsilon_r\psi < 1 \\ \varepsilon_r\psi > 1 \end{cases} \tag{29}$$

Hence, the limit for the range of validity of (27) may be shown by doted region in Fig. 2. When $n\bar{v} < 1$ then $n^2\bar{v}^2 < 1$ and $\bar{v}^2 < 1/n^2 < 1$, thus

$$\frac{v}{c} < \frac{1}{\sqrt{\mu_r\varepsilon_r}} \tag{30}$$

This is the necessary condition for (27) to have a solution. Now we should reject one of these two solutions of (27). Figure 2, shows that if $n^2 < 1$, (27) has no solution for permittivity and no wave could propagate. However, the doted region is the valid region for (27).

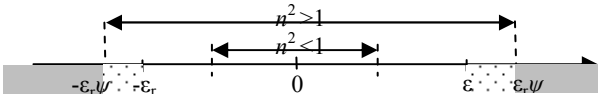

Fig. 2. Region of solution for permittivity, $n\bar{v}<1$.

Since the only propagating mode is in -z direction, therefore the moving media for both TE and TM waves in -z direction act as DNG medium. For the case where the velocity of the moving medium is high, i.e. $n\bar{v}>1$, the cutoff frequency is [14],

$$f = f_{-} = \frac{k_c}{2\pi\sqrt{\mu_0\varepsilon_0}}\cdot\sqrt{\frac{1-\bar{v}^2}{n^2-\bar{v}^2}} \tag{31}$$

For frequencies below the cutoff

$$f < f_{-} \Rightarrow \frac{1}{n_e} < \sqrt{\frac{1-\bar{v}^2}{n^2-\bar{v}^2}} \tag{32}$$

$$n_e > \sqrt{\frac{n^2-\bar{v}^2}{1-\bar{v}^2}} \tag{33}$$

Further, using (11), we can show

$$\varepsilon_e > \varepsilon_r\sqrt{\frac{\varepsilon_r}{\mu_r}\cdot\frac{n^2-\bar{v}^2}{1-\bar{v}^2}} \tag{34}$$

or

$$\varepsilon_e < -\varepsilon_r\sqrt{\frac{\varepsilon_r}{\mu_r}\cdot\frac{n^2-\bar{v}^2}{1-\bar{v}^2}} \tag{35}$$

Similar to previous method of solution, defining

$$\psi = \sqrt{\frac{n^2-\bar{v}^2}{1-\bar{v}^2}} \tag{36}$$

Leads to

$$\begin{cases} if \quad n^2<1 \rightarrow \psi<1 \\ if \quad n^2>1 \rightarrow \psi>1 \end{cases} \Rightarrow \begin{cases} \varepsilon_r\psi<1 \\ \varepsilon_r\psi>1 \end{cases} \tag{37}$$

The range of validity of (33) is shown in Fig. 3. It seems in Fig. 3, we note that both negative and positive signs for permittivity are acceptable.

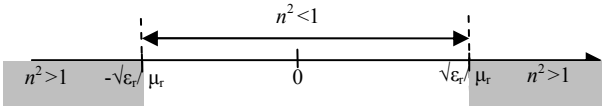

Fig. 3. Region of solution for permittivity, $n\bar{v}>1$.

Again, TE and TM wave impedances can be expressed as

$$Z^{TE} = \frac{\omega\mu_e}{\beta_e} \equiv \pm\frac{\omega\mu a}{\sqrt{k^2a^2-k_c^2a}} \tag{38}$$

$$Z^{TM} = \frac{\beta_e}{\omega\varepsilon_e} \equiv \pm\frac{\sqrt{k^2a^2-k_c^2a}}{\omega\varepsilon a} \tag{39}$$

And both TE and TM waves may propagate in +z and -z directions simultanously, and the equivalent permittivity and permeability in +z and -z directions are positive and negative, respectively. Finally, for frequency above the cutoff frequency

$$n_e < \sqrt{\frac{n^2-\bar{v}^2}{1-\bar{v}^2}} \tag{40}$$

One can show that

$$-\sqrt{\frac{\varepsilon_r}{\mu_r}\cdot\frac{n^2-\bar{v}^2}{1-\bar{v}^2}} < \varepsilon_e < \varepsilon_r\sqrt{\frac{\varepsilon_r}{\mu_r}\cdot\frac{n^2-\bar{v}^2}{1-\bar{v}^2}} \tag{41}$$

Based on TE and TM impedances (38), and (39) and the propagation mode [14], the only propagating mode is in +z direction and so the moving media for both TE and TM waves in +z direction act as DPS medium.

As a summary, for a slowly moving medium there are two critical frequencies, separating three frequency ranges with different type of propagation. For frequencies below the cutoff, in TE mode, the equivalent permittivity and permeability in +z direction are negative, whereas in -z direction, they are positive. Similarly, for TM mode, the equivalent permittivity and permeability in +z and -z directions are positive and negative, respectively. For frequency $f_c < f < f_+$, the only propagating mode is -z and so the moving media for both TE and TM waves in -z direction act as DNG medium. For frequency above f_+, for both TE and TM modes, the equivalent permittivity and permeability in +z and -z directions are positive and negative, respectively.

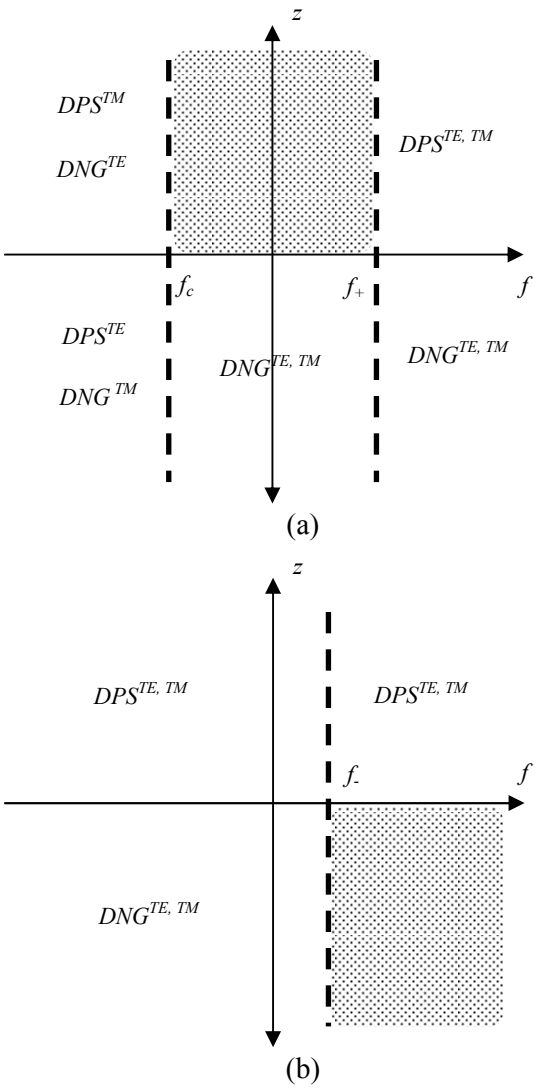

Fig. 4. Moving media as a DNG or DPS equivalent medium for each frequency band and propagation mode, (a) $n\bar{v}<1$, (b) $n\bar{v}>1$.

IV. CONCLUSION

The anomalous wave propagation in a homogeneous, isotropic and lossless medium that moves with a constant velocity along the axis of a rectangular waveguide is investigated. The correct sign of the permittivity and permeability of an equivalent stationary medium, for each TE and TM modes and for both low and high dielectric velocities are extracted and it demonstrated that this media acts as an metamaterial structure over specific frequency ranges.

REFERENCES

[1] V. G. Veselago, "The Electrodynamics of Substances with Simultaneously Negative Values of ε and μ," *Sov. Phys. Usp*., vol. 10, no. 4, pp. 509-514, 1968.

[2] W. Rotman, "Plasma Simulation by Artificial Dielectrics and Parallel-plate Media," *IRE Trans. Antennas Propag.*, vol. 10, pp. 82-95, 1962.

[3] J. B. Pendry, A. J. Holden, D. J. Robbins, and W. J. Stewart "Magnetism from Conductors and Enhanced Nonlinear Phenomena," *IEEE Trans. Microw. Theory Tech.*, vol. 47, pp. 2075-2084, 1999.

[4] D. R. Smith, W. J. Padilla, D. C. Vier, S. C. Nemat-Nasser, and S. Schultz "Composite Medium with Simultaneously Negative Permeability and Permittivity," *Phys. Rev. Lett.*, vol. 84, pp. 4184, 2000.

[5] D. R. Smith, J. B. Pendry, and M. C. Wiltshire," Metamaterials and Negative Refractive Index," *Science*, vol. 305, pp. 788, 2004.

[6] F. Villa-Villa, J. A. Gaspar-Armenta, A. Mendoza-Su´arez, "Surface Modes in One Dimensional Photonic Crystals that Include Left Handed Materials," *J. of Electromagn. Waves and Appl.*, vol. 21, no. 4, pp. 485-499, 2007

[7] N. Liu, H. Guo, L. Fu, S. Kaiser, H. Schweizer and H. Giessen, "Three-dimensional Photonic Metamaterials at Optical Frequencies," *Nature Materials,* vol. 7, pp. 31-37, 2008.

[8] S. Zhang, W. Fan, N. C. Panoiu, K. J. Malloy, R. M. Osgood, and S. R. J. Brueck "Experimental Demonstration of Near-infrared Negative-index Metamaterials," *Phys. Rev. Lett.*, vol. 95, pp. 137404, 2005.

[9] G. Shvets, "Photonic Approach to Making a Material with a Negative Index of Refraction," *Phys. Rev. B* 67, 035109, 2003.

[10] S. Zhang, W. Fan, B. K. Minhas, A. Frauenglass, K. J. Malloy, and S. R. Brueck, "Midinfrared Resonant Magnetic Nanostructures Exhibiting a Negative Permeability," *Phys. Rev. Lett*., vol. 94, 37402, 2005.

[11] H. J. Lezec, J. A. Dionne, H. A. Atwater, "Negative Refraction at Visible Frequencies," *Science,* vol. 316, pp. 430-432, 2007.

[12] A. Pimenov, A. Loidl, K. Gehrke, V. Moshnyaga, K. Samwer, "Negative Refraction Observed in a Metallic Ferromagnet in the Gigahertz Frequency Range," *Phys. Rev. Lett*., vol. 98, pp. 197401-197401- 4, 2007.

[13] J. R. collier and C. T. Tai, "Guided Waves in Moving Media," *IEEE Trans. Microw. Theory Tech.*, vol. MTT-13, pp. 441- 445, July 1965.

[14] L. J. Du and R. T. Compton, Jr., "Cutoff Phenomena for Guided Waves in Moving Media,"

IEEE Trans. Microw. Theory Tech., vol. MTT-14, pp. 358-363, August 1966.

[15] T. M. Grzegorczyk and J. A. Kong, "Electrodynamics of Moving Media Inducing Positive and Negative Refraction," *Phys. Rev. B*, vol. 74, 033102, 2006.

[16] S. Hrabar, J. Bartolic, and Z. Sipus, "Waveguide Miniaturization Using Uniaxial Negative Permeability Metamaterial, " *IEEE Trans. Antennas . Propag.*, vol. 53, no. 1, pp. 110-119, Jan. 2005.

[17] C. A. Balanis, *Advanced Engineering Electromagnetics*, Wiley, 1989.

[18] E. Oezguer; G. Levent, "Rigorous Analysis of Double-Negative Materials with the Multilevel Fast Multipole Algorithm," *Applied Computational Electromagnetics Society (ACES) Journal*, vol. 27, no. 2, pp. 161-168, Feb. 2012.

[19] T. Nikolaos, "Analysis of Electromagnetic Wave Propagation in Frequency Bands of Nonlinear Metamaterials," *Applied Computational Electromagnetics Society (ACES) Journal*, vol. 27, no. 2, pp. 169-180, Feb. 2012.

Amir Jafargholi received the PhD degree in electrical engineering from K.N. Toosi University of Technology, Tehran, Iran, in 2011. He is the coauthor of about 50 scientific contributions published in international books, journals and peer-reviewed conference proceedings. His research interest includes the applications of metamaterials in the analysis and synthesis of antennas. Dr. Jafargholi was a recipient of a Student's Best Thesis National Festival award for his BS thesis, on May 2006. He was a recipient of the 22th Khawarizmi International and 13th Khawarizmi Youth Award on Jan. 2009 and Oct. 2011, respectively. He was also the recipient of Research Grant Awarded in Metamaterial 2010.

Ali Jafargholi was born in Tehran, Iran, on November 3, 1989. He received the B.S degree in electrical engineering from Sharif University of Technology, Tehran, Iran, in 2012, and is currently working toward the M.S degree in communication engineering. His research interests include metamaterial applications to antenna designs.

A New Method of QPSK Demodulation Based on Modified 26 GHz Six-Port Circuit

Lotfi Osman, Imen Sfar, and Ali Gharsallah

Department of Physics, UR "CSEHF" - 05/UR/11-10
University of Sciences El Manar, 2092 Tunisia
lotfi.osman@supcom.rnu.tn, imen.sfar@voila.fr, ali.gharsallah@gmail.com

Abstract - In this paper, we propose to study a new demodulation technique of a QPSK signal exploited in a homodyne receiver by using a modified six-port circuit as demodulator. We will present two techniques of the same structure but we will retain only the best configuration. The new approach allows the integration of the receiver module in a high-performance millimeter wave technology, reducing the size and overall cost of the receivers. This approach is validated by using Agilent's Advanced Design System (ADS) software for RF design and simulation.

Index Terms - ADS software, direct conversion receiver, QPSK demodulator, Six-port circuit.

I. INTRODUCTION

Due to the overwhelming demand for wireless communications, efforts were deployed to simplify the structure of receivers used in demodulators thus reducing both their dimensions and costs. The new communication systems need a high fidelity transmission of high-speed information. In the case of conventional receivers, the manufacturing defaults which are unavoidable in high-frequency generate distortions of the in-phase and quadrature RF signals. We know that the increase in frequency leads to a decrease in wavelength. It then becomes more and more difficult to perform couplers with excellent performance [1]. The new architecture shown in Fig. 1 makes it possible through a new phase demodulation system not only to correct the imperfections of manufacture, but also to adjust both the gain and phase errors of conventional demodulators. The six-port structure was successfully used in the design of network analyzers and other applications. Recall that the theory of the six-port circuit was widely developed by many researchers in order to show its qualities as a reflectometer [2, 3].

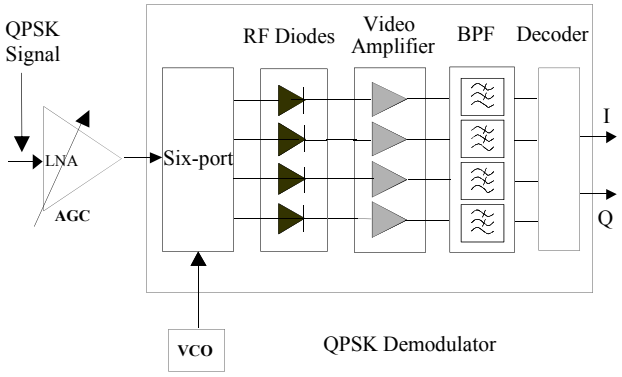

Fig. 1. Structure of the new QPSK demodulation technique.

The circuit can be considered as a black box with two inputs, one for the reference signal and the other for the signal to identify, with four possible combinations between the input signals.

In this paper, we propose a new technique to extract the information contained in a quadrature modulated signal. This will be achieved with a new type of QPSK demodulator based on a modified six-port circuit. But first of all, we will explain how a conventional six-port junction was initially designed to measure the reflection coefficient of a load (one-port device).

II. THE CONVENTIONAL SIX-PORT JUNCTION

It is a linear passive component composed of several couplers connected by transmission lines [4, 5]. It was originally designed in the sixties to measure the phase of RF signals. This component has two inputs and four outputs. The first input is

Submitted On: Dec. 7, 2011
Accepted On: May 22, 2012

reserved to the reference signal; whereas, the second input receives the signal to be identified. The six-port structure has been successfully used in the design of network analyzers and other similar applications. The theory of the six-port junction was further developed by Glenn F. Engen [6] by highlighting its qualities of reflectometer.

The response of this junction can be characterized by the following set of equations that express the powers at its four outputs:

$$\begin{cases} P_1 = |b_1|^2 = |\mathrm{Aa} + \mathrm{Bb}|^2 \\ P_2 = |b_2|^2 = |\mathrm{Ca} + \mathrm{Db}|^2 \\ P_3 = |b_3|^2 = |\mathrm{Ea} + \mathrm{Fb}|^2 \\ P_4 = |b_4|^2 = |\mathrm{Ga} + \mathrm{Hb}|^2 \end{cases}, \quad (1)$$

where the coefficients A to H are complex constants which must be determined by a calibration procedure, and a & b are incident and reflected waves at the input of a load.

Figure 2 illustrates a schema of a six-port reflectometer using 90° hybrid couplers to measure the reflection coefficient Γ of the load.

The schema of a 90° hybrid coupler and its scattering matrix are shown in Fig. 3.

(a)

$$S = \frac{1}{\sqrt{2}}\begin{bmatrix} 0 & \mathrm{j} & 1 & 0 \\ \mathrm{j} & 0 & 0 & 1 \\ 1 & 0 & 0 & \mathrm{j} \\ 0 & 1 & \mathrm{j} & 0 \end{bmatrix}. \quad (2)$$

(b)

Fig. 3. (a) 90° hybrid coupler; (b) corresponding scattering matrix.

The following set of equations give the expressions of powers at the four outputs:

$$\begin{cases} P_1 = \frac{|a|^2}{4}|\Gamma - 1|^2 \\ P_2 = \frac{|a|^2}{8}|\Gamma - (-1 + \mathrm{j})|^2 \\ P_3 = \frac{|a|^2}{8}|\Gamma - (-1 - \mathrm{j})|^2 \\ P_4 = \frac{|a|^2}{4} \end{cases}. \quad (3)$$

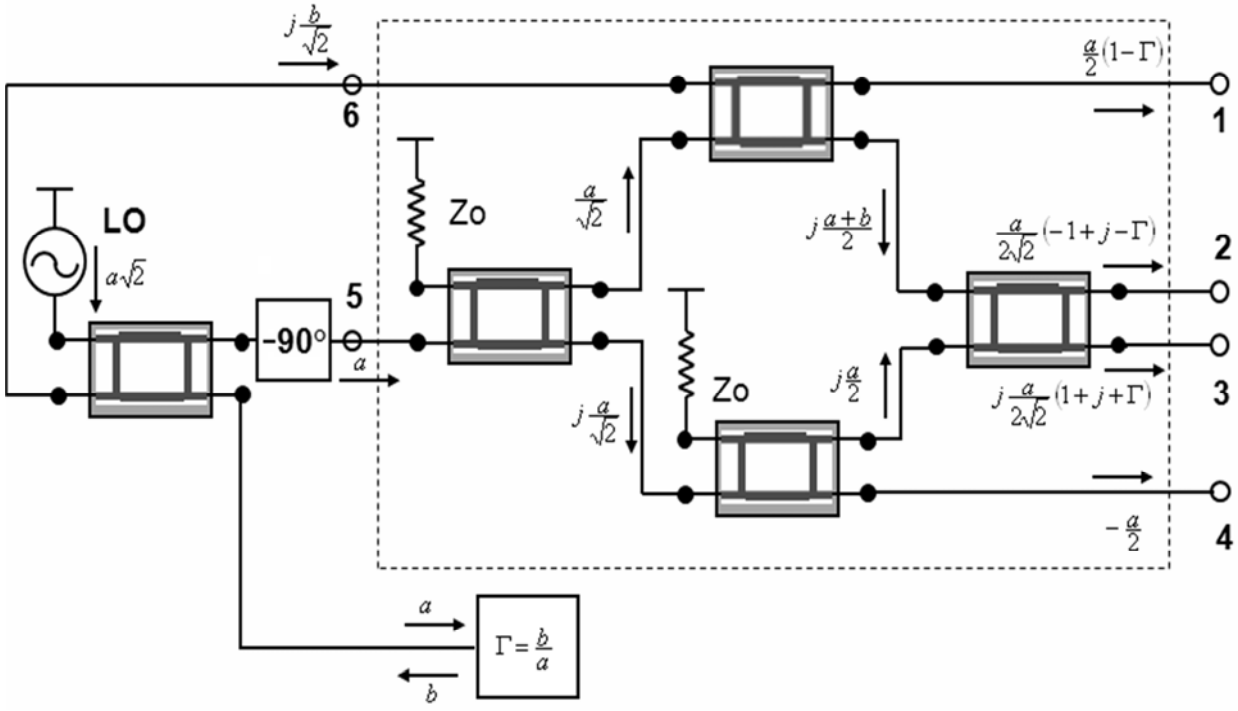

Fig. 2. Block diagram of the conventional six-port junction.

Only P_4 is independent of Γ. It will therefore be used as reference power, which leads to the following three normalized powers:

$$\begin{cases} p_1 = \dfrac{P_1}{P_4} = |\Gamma - 1|^2 \Rightarrow |\Gamma - 1| = \sqrt{p_1} \\ p_2 = \dfrac{P_2}{P_4} = |\Gamma - (-1 + \mathrm{j})|^2 \Rightarrow \\ \qquad |\Gamma - (-1 + \mathrm{j})| = \sqrt{2p_2} \\ p_3 = \dfrac{P_3}{P_4} = |\Gamma - (-1 - \mathrm{j})|^2 \Rightarrow \\ \qquad |\Gamma - (-1 - \mathrm{j})| = \sqrt{2p_3} \end{cases} . \quad (4)$$

The three resulting equations are the equations of three circles whose centers are:

$$q_1 = 1,\ q_2 = -1 + j \text{ and } q_3 = -1 - j.$$

Figure 4 shows the graphical representation of these three circles.

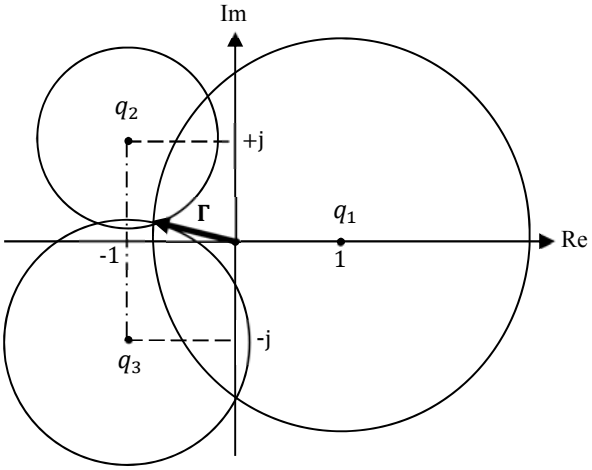

Fig. 4. Graphical representation of the reflection coefficient Γ.

The intersection point of these three circles will give us the value of the reflection coefficient Γ at the input of the device. The position of the points q_i depends on the architecture of the six-port junction and, ideally, the three points should be located at 120° from each other and equidistant from the center.

Finally, the measurement of the reflection coefficient Γ consists in determining the power levels at the four output ports and developing a suitable algorithm by considering one of the output ports as reference.

III. PRINCIPLE OF A MODIFIED SIX-PORT CIRCUIT

The modified six-port circuit is performed with two types of couplers: Wilkinson coupler acts as a power splitter [7, 8] and a 90° hybrid coupler produces two output signals phase shifted by 90°. We first represent in Fig. 5 below, the scheme of a Wilkinson coupler and its scattering matrix.

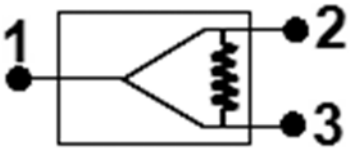

(a)

$$S = -\frac{\mathrm{j}}{\sqrt{2}}\begin{bmatrix} 0 & 1 & 1 \\ 1 & 0 & 1 \\ 1 & 1 & 0 \end{bmatrix}. \quad (5)$$

(b)

Fig. 5. (a) Wilkinson coupler; (b) corresponding scattering matrix.

Figure 6 shows the modified six-port circuit with its two inputs (a_5 & a_6) and four outputs. Assuming that the input signals have the same amplitude and that each port is matched, the wave equations to those inputs and outputs ports can be expressed as follows:

$$\begin{cases} a_5 = a\exp(j\theta_5) \\ a_6 = a\exp(j\theta_6) \\ b_1 = -j\dfrac{a}{2}\exp(j\theta_5).\{1 - \exp[j(\theta_6 - \theta_5)]\} \\ b_2 = \dfrac{a}{2}\exp(j\theta_5)\left\{1 - \exp\left[j\left(\theta_6 - \theta_5 - \dfrac{\pi}{2}\right)\right]\right\} \\ b_3 = \dfrac{a}{2}\exp(j\theta_5).\{1 - \exp[j(\theta_6 - \theta_5 - \pi]\} \\ b_4 = -j\dfrac{a}{2}\exp(j\theta_5)\left\{1 - \exp\left[j\left(\theta_6 - \theta_5 + \dfrac{\pi}{2}\right)\right]\right\} \end{cases} . \quad (6)$$

Given that the output power of a matched load is equal to $|b|^2$, we can notice that for each output there is a phase shift Δθ equal to (θ_6 - θ_5) between the 2 input signals corresponding to a zero power. By using the circuit as a QPSK demodulator, we can differentiate four modulation states by using output power measurements and detecting that which it is minimal with regard to the others [9].

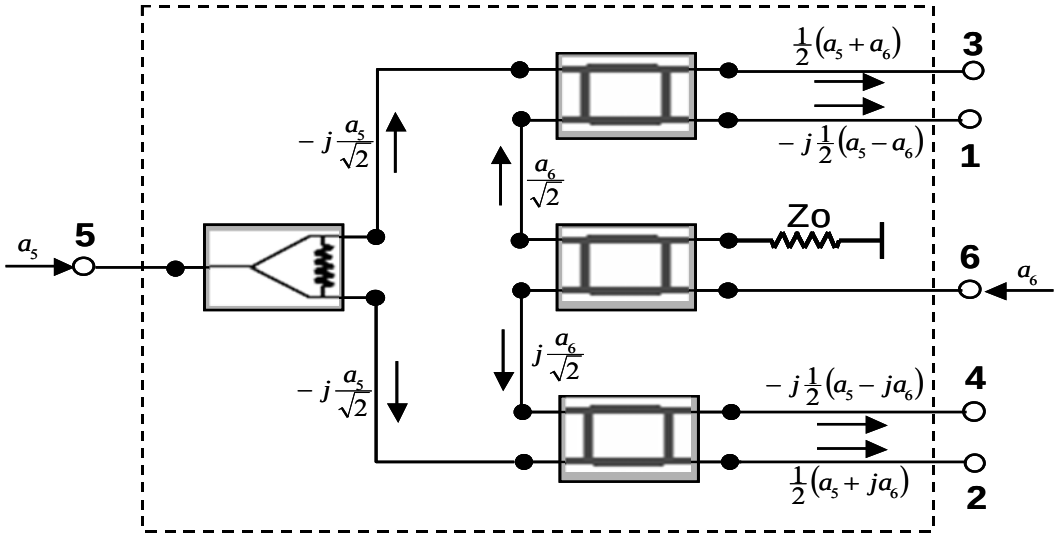

Fig. 6. Block diagram of the modified six-port.

IV. STUDY OF A NEW SIX-PORT STRUCTURE

Having as basic structure the diagram of the modified six-port junction represented in Fig. 6, we designed this structure by considering two different architectures for the hybrid couplers. The circuit is simulated at 26 GHz center frequency with Momentum 3D Planar EM Simulator of Advanced Design System software [10] by using microstrip lines. The parameters of the used substrate are: 0.254 mm for the thickness and 9.9 for the relative permittivity.

Figures 7 and 8 show two structures of the six-port circuit performed with square and round hybrid couplers, respectively.

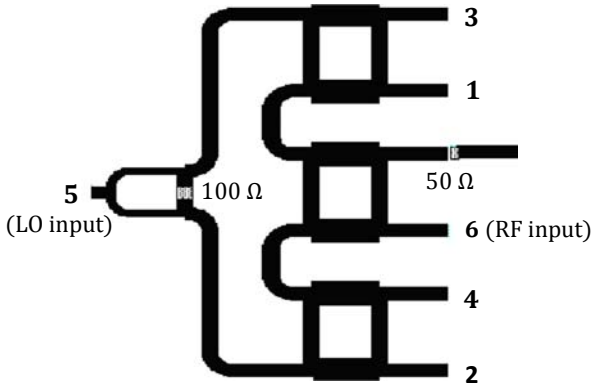

Fig. 7. Six-port performed with square hybrid couplers.

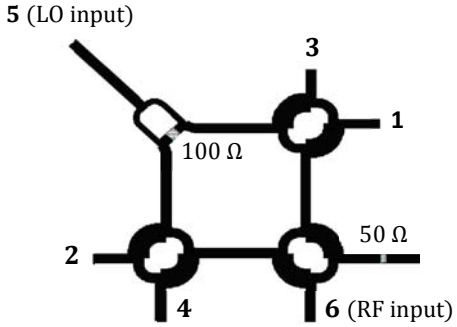

Fig. 8. Six-port performed with round hybrid couplers.

We present hereafter the simulation results of Scattering parameters (S-parameters) of both structures in a frequency band around 26 GHz.

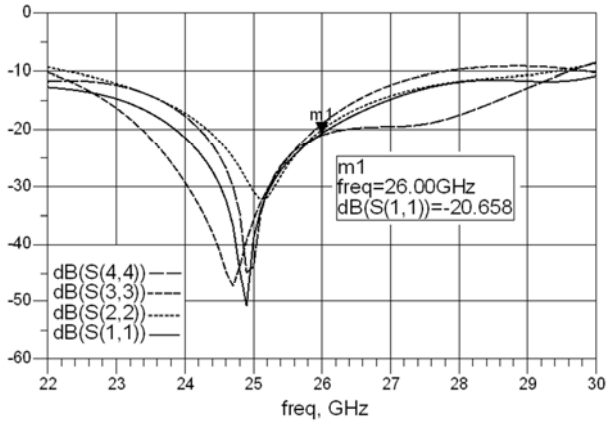

Fig. 9. Output reflection coefficients of the structure with square hybrid couplers.

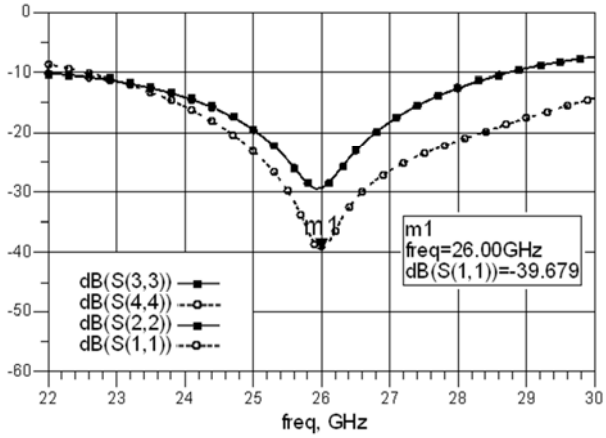

Fig. 10. Output reflection coefficients of the structure with round hybrid couplers.

Figures 9 and 10 show the matching values at their output ports in [22-30] GHz frequency band.

As can be seen, we get a better matching at f = 26 GHz for the structure based on round hybrid couplers with $S_{11} = S_{44} \approx$ -39 dB and $S_{22} = S_{33} \approx$ -30 dB. It follows that the round shapes of couplers used in this structure contributes to this good matching compared to that based on square hybrid couplers with $S_{ii} \approx$ -20 dB at 26 GHz for i = 1 to 4.

That is why we present in what follows results of the phase and the coupling obtained only from the structure with round hybrid couplers. Figures 11 and 12 show the transmission curves S_{5i} and S_{6i} with i = 1 to 4. All values obtained at f = 26 GHz are close to - 6 dB ($= -20\log\frac{1}{2}$).

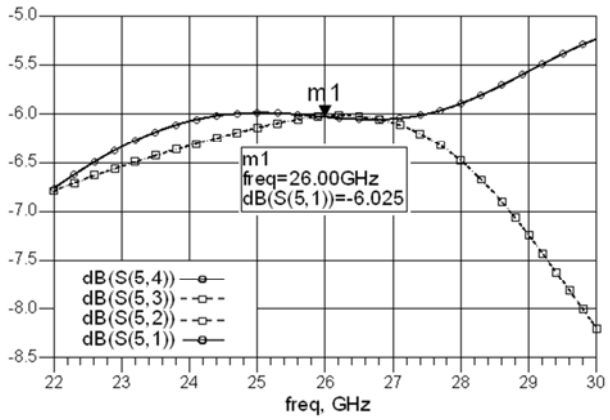

Fig. 11. Transmission coefficients between LO input port (N°5) and output ports.

The transmission phases between each two output ports are represented in Fig. 13 (a) and (b).

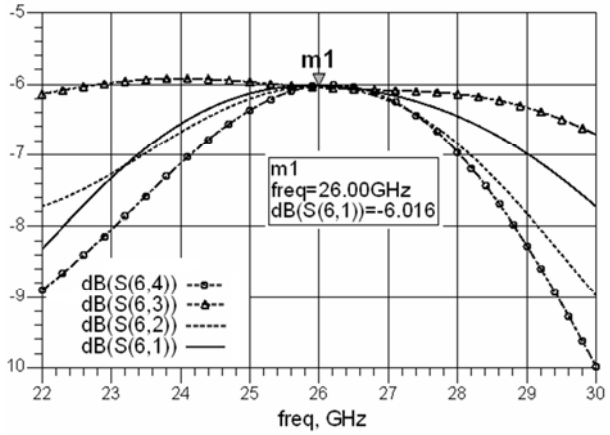

Fig. 12. Transmission coefficients between RF input port (N°6) and output ports.

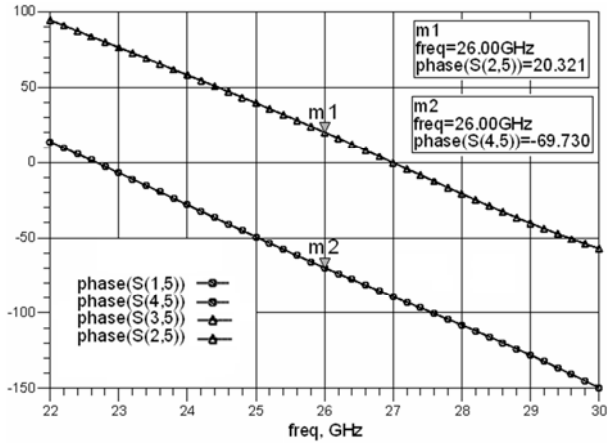

(a)

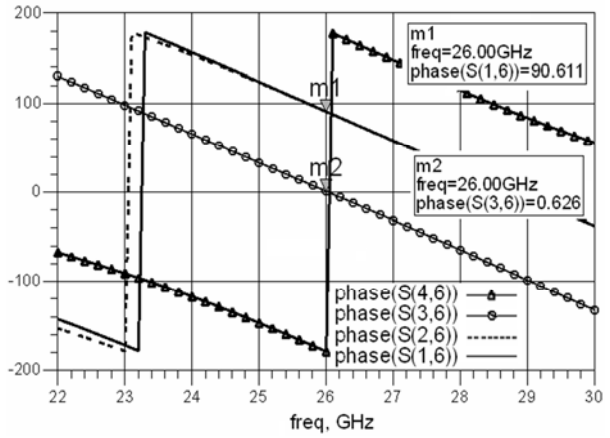

(b)

Fig. 13. Transmission phases: (a) S_{i5} , (b) S_{i6} with i = 1 to 4.

We can see that the phase difference is always around ± 90°.

All results obtained for the transmission coefficients and the transmission phases are consistent with the architecture of the modified six-port circuit represented in Fig. 6.

We finish this study par presenting the isolation curves as well for the two input ports as for the four output ports. Figure 14 shows that there is an excellent isolation between input ports 5 and 6 with about -36 dB at 26 GHz frequency.

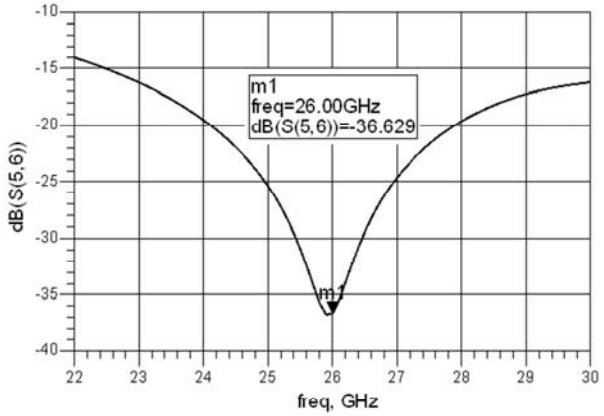

Fig. 14. Isolation (S_{56}) between input ports.

Figure 15 also shows that there is a good isolation between the output ports, all values being less than -33 dB at this frequency.

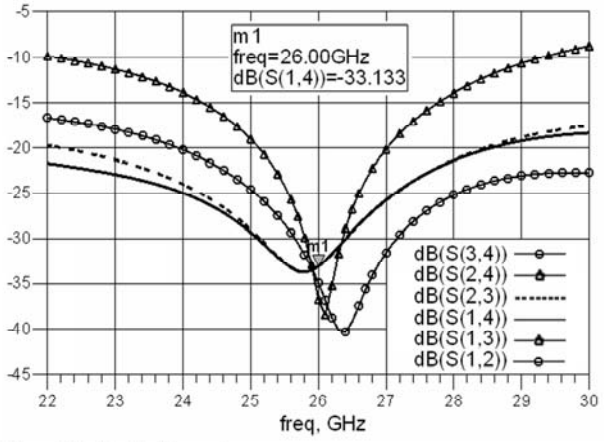

Fig. 15. Isolations between output ports.

V. ELECTROMAGNETIC SIMULATIONS OF THE SIX-PORT WITH A POWER DETECTION CIRCUIT

In order to take advantage of the qualities of the six-port circuit as a phase demodulator of a QPSK signal [11], we have made simulations based on some assumptions for the structure with the round hybrid couplers. To distinguish the four states of modulation, the output signals have to pass through a power detection circuit.

Figure 16 presents the diagram of the six-port circuit with a power detection circuit. Input ports 5 and 6 receive the reference signal from a local oscillator and the QPSK signal, respectively.

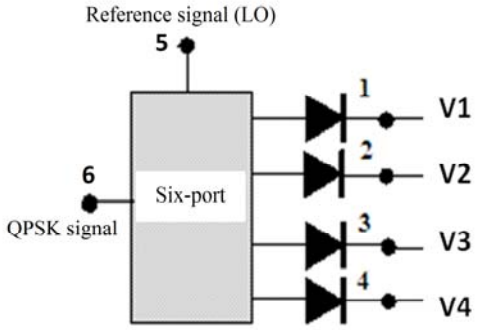

Fig. 16. The six-port with a power detection circuit.

DC voltage obtained at each output is proportional to the square of the amplitude of b_i [12]:

$$V_i = K_i \left| b_i \right|^2 . \tag{7}$$

The set of equations (8) shows that the power at each output depends on the phase difference between the input signals.

Assuming the detectors identical ($K_i = K$), we can write:

$$\begin{cases} V_1 = K\dfrac{|a|^2}{4}\left|1-\exp\left(j\Delta\theta\right)\right|^2 = K|a|^2\left|\sin\left(\dfrac{\Delta\theta}{2}\right)\right|^2 \\ V_2 = K\dfrac{|a|^2}{4}\left|1-\exp\left(j\left(\Delta\theta-\dfrac{\pi}{2}\right)\right)\right|^2 = K|a|^2\left|\sin\left(\dfrac{\Delta\theta-\dfrac{\pi}{2}}{2}\right)\right|^2 \\ V_3 = K\dfrac{|a|^2}{4}\left|1-\exp\left(j\left(\Delta\theta-\dfrac{\pi}{2}\right)\right)\right|^2 = K|a|^2\left|\sin\left(\dfrac{\Delta\theta-\pi}{2}\right)\right|^2 . \\ V_4 = K\dfrac{|a|^2}{4}\left|1-\exp\left(j\left(\Delta\theta-\dfrac{\pi}{2}\right)\right)\right|^2 = K|a|^2\left|\sin\left(\dfrac{\Delta\theta+\dfrac{\pi}{2}}{2}\right)\right|^2 \end{cases} \tag{8}$$

To obtain variations in amplitude of the output voltages relative to the phase shift between RF and reference signals, we vary the phase of the RF signal between 0° and 360° while maintaining constant the powers of the input signals, and the phase of the reference signal. Figure 17 shows the

variations of amplitudes V_1, V_2, V_3, and V_4 at ports 1, 2, 3, 4 depending on the phase shift between RF and LO inputs.

We can observe that every voltage has a single minimum or maximum value for a phase shift between reference and RF signals going from 0° to 360°. This phase shift can be determined using only the values of these voltages and relying on an appropriate algorithm.

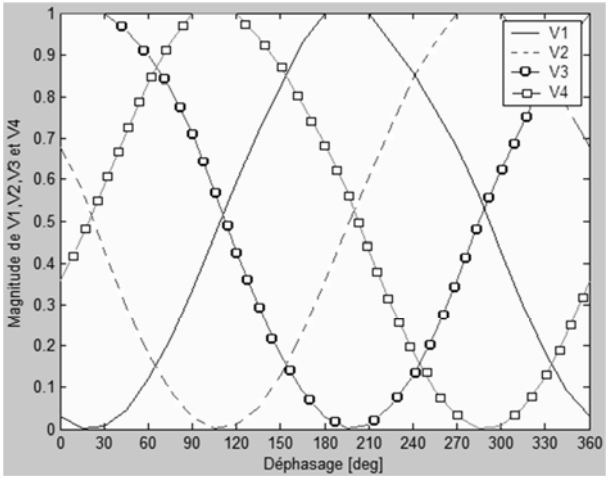

Fig. 17. Normalized output dc voltages versus the phase shift between RF and LO input signals.

The modified six-port circuit can then be regarded as a phase discriminator. In terms of phase shift between RF inputs, each function $V(\Delta\theta)$ is periodic with period 2π, and minimum values of the four voltages are separated by multiples of $\pi/2$. Subsequently, we can consider a method to obtain the constellation of the demodulated signal in the I/Q complex plane.

The phase θ_6 of the input signal contains the information while the phase θ_5 of the LO signal represents the reference. In the I/Q plane and using Eq. (9), we define a vector Γ representing a combination of the four dc output voltages [13].

$$\Gamma = \left[(V_3 - V_1) + j(V_4 - V_2)\right]\exp\left(j\frac{\pi}{4}\right). \qquad (9)$$

Figure 18 illustrates the four modulation states of a QPSK modulated signal.

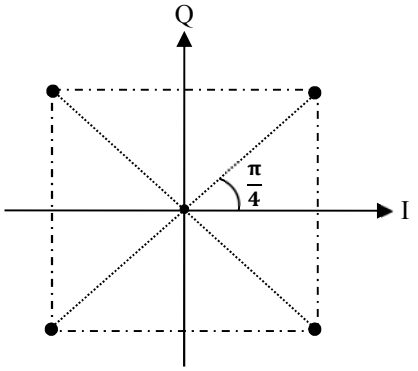

Fig. 18. QPSK modulation.

Assuming $\theta_6 = \frac{\pi}{4}$ with as reference $\theta_5 = \frac{\pi}{4}$, we obtain $\Delta\theta = 0$. Therefore, the output voltages can be expressed as follows:

$$V_1 = 0 \;\;\&\;\; V_2 = V_4 = \frac{1}{2}K|a|^2 \;\;\&\;\; V_3 = K|a|^2 \quad . (10)$$

So, the point obtained using Eq. (9) will be given by the vector $\Gamma = K|a|^2\exp\left(j\frac{\pi}{4}\right)$. This point is located in the center of the first quadrant of Fig. 18, which confirms that the signal is correctly demodulated.

Table 1 below presents the values V_1 to V_4 and Γ according to θ_6 and corresponding to the four modulation states.

Table 1: Theoretical demodulation results of a QPSK signal

θ_6	V_1	V_2	V_3	V_4	Γ
$\frac{\pi}{4}$	0	$\frac{1}{2}K\|a\|^2$	$K\|a\|^2$	$\frac{1}{2}K\|a\|^2$	$K\|a\|^2\exp\left(j\frac{\pi}{4}\right)$
$3\frac{\pi}{4}$	$\frac{1}{2}K\|a\|^2$	0	$\frac{1}{2}K\|a\|^2$	$K\|a\|^2$	$K\|a\|^2\exp\left(j\frac{3\pi}{4}\right)$
$5\frac{\pi}{4}$	$K\|a\|^2$	$\frac{1}{2}K\|a\|^2$	0	$\frac{1}{2}K\|a\|^2$	$K\|a\|^2\exp\left(j\frac{5\pi}{4}\right)$
$7\frac{\pi}{4}$	$\frac{1}{2}K\|a\|^2$	$K\|a\|^2$	$\frac{1}{2}K\|a\|^2$	0	$K\|a\|^2\exp\left(j\frac{7\pi}{4}\right)$

We can notice the excellent qualities of the modified six-port circuit as a phase demodulator. Thanks to this analytical development, we can confirm that with its new architecture, the six-port circuit can be suitably used as a phase demodulator of a QPSK modulated signal. Using the phase discriminator properties of the modified six-port circuit and an appropriate analog processing for the output signals, it becomes possible to demodulate other signals modulated in phase even though the circuit has been originally designed to demodulate a QPSK signal.

VI. CONCLUSION

The six-port junction was especially used for microwave instrumentation and measurements. The objective was to design a new microwave and millimeter wave direct conversion receiver based on a six-port frequency discriminator and dedicated to a high speed QPSK modulation. This junction was in the past designed and fabricated in monolithic hybrid microwave integrated circuit (MHMIC) and monolithic microwave integrated circuit (MMIC) with a certain complexity in manufacturing.

We propose in this paper a modified six-port circuit based on microstrip technology. It is distinguished by its simple and compact structure which allows an easy implementation of low cost and in addition provides a certain resistance to manufacturing imperfections. Note that there were no radiation problems in the functioning of this new structure which also has a high immunity to phase distortions and fluctuations in the power of the RF signal and adjacent channel.

Finally, we can assert that it is possible to realize a phase demodulator for an efficient QPSK modulated RF signal based on just a simple and compact structure.

ACKNOWLEDGMENT

The authors would like to thank Dr. J. Belhadj Tahar of Higher School of Communication of Tunis for his valuable contribution in this work. They would also like to acknowledge the constructive comments and suggestion provided by the reviewers. Their kind effort certainly contributed to the quality of this publication.

REFERENCES

[1] F. D. L. Peters, D. Hammou, S. O. Tatu, and T. A. Denidni, "Modified Millimeter-Wave Wilkinson Power Divider for Antenna Feeding Network," *Progress In Electromagnetics Research Letters*, vol. 17, pp. 11-18, 2010.

[2] N. Seman, M. E. Bialkowski, S. Z. Ibrahim, and A. A. Bakar, "Design of an Integrated Correlator for Application in Ultra Wideband Six-Port Transceivers," *IEEE Antennas and Propagation Society International Symp.*, pp. 1- 4, June 2009.

[3] M. Mohajer and A. Mohammadi, "A Novel Architecture for Six-Port Direct Conversion Receiver," *15th IEEE International Symposium on Personal, Indoor and Mobile Radio Communications*, vol. 4, pp. 2705-2709, Sept. 2004.

[4] V. Demir, D. Elsherbeni, D. Kajfez, and A. Z. Elsherbeni, "Efficient Wideband Power Divider for Planar Antenna Arrays," *Applied Computational Electromagnetics Society (ACES) Journal*, vol. 21, no. 3, pp. 318-324, Nov. 2006.

[5] A. Mohra, A. F. Sheta, and S. F. Mahmoud, "New Compact 3dB 0/180 Microstrip Coupler Configurations," *Applied Computational Electromagnetics Society (ACES) Journal*, vol. 19, no. 2, pp. 108-112, July 2004.

[6] G. F. Engen, "The Six-Port Reflectometer: An Alternative Network Analyzer," *IEEE Transactions on Microwave Theory and Techniques*, vol. 25, no. 12, pp. 1075-1080, Dec. 1977.

[7] S. Ibrahimpasic and M. Hasanovic, "Modeling and Simulation of Wilkinson Power Splitter in Suspended Stripline," *Applied Computational Electromagnetics Society (ACES) Journal*, vol. 25, no. 10, pp. 888-893, October 2010.

[8] A. S. Al-Zayed, Z. M. Hejazi, and A. S. Mohra, "A Microstrip Directional Coupler with Tight Coupling and Relatively Wideband Using Defected Ground Structure," *Applied Computational Electromagnetics Society Journal*, vol. 25, no. 10, pp. 877-887, October 2010.

[9] S. O. Tatu, K. Wu, and T. A. Dendini, "Direction of Arrival Estimation Method Based on Six-Port Technology," *IEE Proceedings - Microwaves Antennas and Propagation*, vol. 153, no. 3, pp. 263-269, June 2006.

[10] "Advanced Design System," 2005 [Online]. http://www.ece.uci.edu/eceware/ads_docs/

[11] I. Molina-Fernandez, J. G. Wanguemert-Perez, A. Ortega-Monux, R. G. Bosisio, and K. Wu, "Planar Lightwave Circuit Six-Port Technique for Optical Measurements and Characterizations," *Journal of Lightwave Technology*, vol. 23, no. 6, pp. 2148-2150, June 2005.

[12] D. Hammou, E. Moldovan, K. Wu, and S. O. Tatu, "60 GHz MHMIC Six-Port Model Analysis," *Microwave and Optical Technology Letters*, vol. 52, no. 9, Sep. 2010.

[13] G. Vinci, A. Koelpin, F. Barbon, and R. Weigel, "Six-Port-Based Direction-Of-Arrival Detection System," *Asia-Pacific Microwave Conference Proceedings (APMC)*, pp. 1817-1820, Dec. 2010.

Lotfi Osman received his Ph.D. degree in Automatic & Industrial Computing from the University of Lille 1, France, in 1987. He is currently Assistant Professor with the Department of Electronics, Physics and Propagation at the Higher School of Communication of Tunis, Sup'Com. In 2004, he joined the Research Unit "CSEHF" at the Faculty of Sciences of Tunis, Tunis El Manar University. His current research interests include antennas and modeling in microwave integrated circuits. He is also involved with experimental characterization and antenna measurement.

Imen Sfar was born in Tunis in 1978, she received in 2006 her master's degree in Electronics from the Faculty of Sciences of Tunis, Tunisia, where she's currently working toward her Ph.D. Her current research interests include antennas for wireless communication and analysis of microwave structures.

Ali Gharsallah Professor at the Faculty of Sciences of Tunis and Head of Research Unit "CSEHF" (code 05/UR/11-10) at the Department of Physics, Faculty of Sciences of Tunis, El Manar University. He received the engineering's degree in radio-electrical from the Higher School of Telecommunications of Tunis in 1986 and the Ph.D. degree in 1994 from the National Engineering School of Tunis. Since 1991, he was with the Department of Physics at the Faculty of Sciences of Tunis. His current research interests include antennas, multilayered structures and microwave integrated circuits.

Compact Tri-band Metamaterial Antenna for Wireless Applications

Sheeja K. L.[1], Prasanna Kumar Sahu [1], Santanu Kumar Behera[2] and Nabil Dakhli[3]

[1] Department of Electrical Engineering
National Institute of Technology, Rourkela, Odisha, India.
sheejakl@gmail.com, pksahu@nitrkl.ac.in

[2] Department of Electronics and Communication Engineering
National Institute of Technology, Rourkela, Odisha, India.
prof.s.k.behera@gmail.com

[3]Research Unit of Telecommunication Systems (6Tel) at Sup'Com, Tunisia.

Abstract ─ A novel compact triband coplanar waveguide fed metamaterial antenna is proposed. The left-handed (LH) inductance is provided by two parallel short ended spiral inductors. We achieved pentamodes of resonance consisting of negative modes, zeroth mode and positive modes. The resonance frequency at each of these modes are f_{-2}=1.01 GHz, f_{-1}=2.11GHz, f_0=2.48 GHz, f_{+1}= 3.04 GHz and f_{+2}=3.54GHz with triband functionality obtained at $f_{-2,}$ f_0 and f_{+2} resonances. Gain of the proposed structure at $f_{-2,}$ f_0 and f_{+2} resonances is found to be -3.4993dB, 1.559dB and 1.9515dB respectively. The proposed antenna is measured at Antenna Measurement Facility (AMF) and results were compared with the simulated results. A good agreement between the measured and the simulated results validates the proposed design. The antenna radiates omni-directional waves in the horizontal plane. The proposed antenna serves the criteria for modern multiband wireless applications with an additional feature of increased bandwidth at the zeroth mode. The proposed multiband antenna is suitable for wireless communication applications such as the Global System for Mobile Communications (GSM) 900 in 1.01GHz, Wireless Local Area Network (WLAN) in the 2.48 GHz band (2.459 - 2.4924)GHz of IEEE 802.11b/g ISM band and worldwide interoperability for microwave access (WiMax) standards in the 3.54GHz band (3.491-3.596)GHz of IEEE 802.11a. This proposed antenna is most suitable for precise multiband wireless communication systems which include the mobile and wireless local area network (WLAN) systems due to their large service area.

Index Terms ─ Composite Right/Left Handed Transmission Line, Metamaterials, Omni-directional antennas, Zeroth Order Resonant antenna.

I. INTRODUCTION

Compact antennas with omni-directional radiation patterns are useful for wireless applications. Various antennas such as dipole, monopole [1], cylindrical patch array [2] and planar back-to-back dipole antenna [3, 4] are widely employed for this purpose. However, these antennas are very complicated in structure and their large size needs to be miniaturized in order to meet the demands of portable devices. In recent years, metamaterials have drawn considerable attention for the design of compact antenna and other microwave devices [5-7]. A compact metamaterial antenna with omni-directional radiation patterns serves the above purpose. They are designed to be small in size with additional features to provide multifrequency and multifunctionality bands [8, 9]. However, the ZOR antennas reported in these papers suffered from

Submitted On: Dec. 26, 2011
Accepted On: May 19, 2012

low radiation efficiencies that ranged from 5-50%. In [10], an increased height ZOR antenna was presented with a size of 120 x 49mm. Though efficiency was increased to 25% but gain was only about -0.52 dBi at 7.79 GHz. The Composite Right/Left Handed Transmission Line (CRLH TL) metamaterials using zeroth order resonance (i.e.; inductive and capacitive loadings on a microstrip transmission line) are popular for their inherent multiband property which can be extensively exploited to meet various demands. Another advantage of this CRLH TL is that at zeroth order resonance infinite wavelength is supported. This is due to the CRLH TL's unique property to support a fundamental backward wave (anti parallel group and phase velocities) and zero propagation constant with zero (unbalanced CRLH TL) or finite group velocity (balanced CRLH TL) at a finite frequency [8]. This property is exploited in the miniaturization of antenna size because the frequency at zeroth order resonance is independent of the physical dimensions of the antenna. Also at zeroth mode we have uniform field distribution which maximizes directivity and minimizes dissipative losses. Popular structures that are used for the implementation of the CRLH TL are the microstrip technique based on the most popular Dan Sievenpiper's Mushroom structure [11]. Though it satisfies the LH property, it suffers from a tradeoff between the antenna's size reduction and its bandwidth. Lai et al [12] provided dual mode, dual band features; but bandwidth obtained was only about 0.75%. The peak gain and radiation efficiency of this antenna were 0.87 dBi and 70 % respectively. However small ZOR antennas employing a CRLH resonator made up of two or three cells suffer from a low radiation efficiency and poor gain in the zeroth-order resonant mode [13].

In this paper a compact metamaterial antenna consisting of two unit cells is proposed. In this proposed structure, a high gain of 1.9515dB and bandwidth of 2.964 % at 3.54 GHz along with an efficiency of 82.52 % is obtained. Further, at 2.48 GHz, gain of 1.559 dB and bandwidth of 1.36 % along with an efficiency of 55.31% is obtained. The proposed design exhibits triband, pentamode characteristics which can be used for multiband wireless precise applications [14].

II. CRLH Transmission Line and Shunt Mode Zeroth Order Resonance

A composite right/left handed transmission line structure is obtained by cascading N number of unit cells as shown in Fig. 1(a). The size p of each unit cell is much smaller than the guided wavelength ($p << \lambda_g$), so as to satisfy the effective homogeneity condition in which case the diffraction phenomena will dominate over the scattering phenomena. The dispersion diagram of the CRLH TL is shown in Fig. 1(b). It can be obtained by applying Bloch-Floquet theorem to the CRLH unit cell of Fig. 1(a).

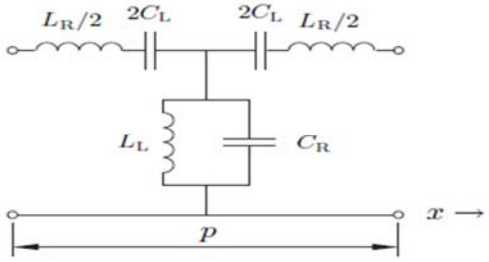

Fig. 1(a). Elemental model of CRLH TL unit cell.

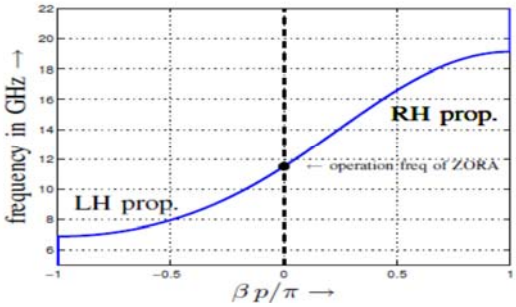

Fig. 1(b). The dispersion diagram for CRLH TL.

The CRLH TL supports a fundamental LH wave (phase advance) at lower frequencies and a RH wave (phase delay) at higher frequencies.

The dispersion relation is given as [15]:

$$\cos[(\beta - j\alpha)p] = 1 - \frac{(\omega^2 - \omega_{se}^2)(\omega^2 - \omega_{sh}^2)}{2\omega^2\omega_R^2}, \quad (1)$$

where,

$$\omega_{se}^2 = \frac{1}{L_R C_L}, \omega_{sh}^2 = \frac{1}{L_L C_R}, \omega_R^2 = \frac{1}{L_R C_R}.$$

Under balanced condition, $\omega_{se} = \omega_{sh} = \omega_0$ and one non-zero frequency point with β=0 is present. This point is referred to as the infinite

wavelength point and is determined from either series resonance or shunt resonance of the unit cell of length p, repeating N times, so a CRLH TL of length $L = N * p$ is realized. The CRLH TL is used as a resonator when it is open ended or short ended under the resonance condition,

$$\beta_n = \frac{n\pi}{L}, \qquad (n = 0,\pm1,\pm2,.....) \quad (2)$$

where β_n is propagation constant along the TL, L is the total length of the TL, and n is the resonance mode number or resonant index and can be a positive or negative integer and also zero. In case of conventional half wavelength resonant antennas, the propagation constant β^{RH} is always positive, and this leads to positive resonant indices (n=+1, +2 ...). But for LH TL structures β^{LH} are negative, and resonant indices will be negative (n=-1,-2 ...). When β_n=0, there is a non-zero frequency. This property is utilized to create a zeroth order resonator. From these conditions, the resonant modes can be $n = 0,\pm1,\pm2,.....$.

Inverting Equation (1) we have

$$\omega(\beta) = \sqrt{\left(\omega_0^2 + \omega_R^2 \sin^2\frac{p\beta}{2}\right)} + \omega_R \sin\frac{p\beta}{2}. \quad (3)$$

From the relation given in Equation (3) we can obtain the resonance frequency of the structure and consequently the dispersion diagram.

The inherent dispersion of CRLH structures allows multiband operation. A standard CRLH TL is inherently dual band, due to its four fundamental parameters (L_R, C_R, L_L, C_L) compared to just two parameters (L_R, C_R) in a conventional transmission line.

A CRLH TL based zeroth order resonating antenna is excited either by open circuiting (by a small coupling capacitance C_c) or by short circuiting (by a small shunt inductance) the CRLH structure. In the open circuit case, the resonance occurs at ω_{sh} and therefore the energy is stored only in the shunt (admittance) elements whereas in the short circuited case, the resonance occurs at ω_{se} and therefore the energy is stored only in the series (impedance) elements. But when the structure is balanced, these two frequencies are equal. Hence, the energy stored is determined by the type of termination i.e.; by the type by which the antenna is excited. In this paper, the antenna structure is balanced and is excited by open circuiting by a small coupling capacitance so that its energy will be stored in the shunt elements.

III. METHODOLOGY

The novel CRLH TL based ZOR antenna was implemented using CPW technique. The compact vialess ZOR antenna proposed by Jang et al [16] was designed to operate over a single band although it was simple and easy to fabricate. In this paper the proposed metamaterial antenna is designed to operate over multiband suitable for precise wireless applications especially point to point wireless communication. Coplanar waveguides are uniplanar transmission line structures where the ground plane and the signal trace are placed on the same side of the substrate. The advantage of such a structure is that to get enhanced bandwidth it is more flexible to change the shunt parameters (C_R, L_L) of a CRLH TL. It provides smaller shunt parasitic RH capacitance C_R if the distance between the CPW grounds from the radiating patch is increased and larger shunt LH inductance L_L if the lengths of the short ended spiral inductors are increased. But in case of microstrip technique as the signal trace is separated from the ground plane by a dielectric layer (i.e; by a substrate material), C_R tends to be large. This is because it depends on the capacitance of the host microstrip line to the ground plane. Also here the shunt inductance, L_L is small because the LH inductance provided by the vias is directly proportional to its height, which in turn is restricted by the substrate's height. So in case of microstrips bandwidth enhancement is just about 0.75 % with a low gain of 0.87 dBi [12].

IV. ANTENNA DESIGN

The geometrical model of the proposed compact triband, pentamode metamaterial antenna is shown in Fig. 2(a) and 2(b) with two unit cells. The fabricated prototype is shown in Fig. 2(c). It consists of a single layer substrate of size 29.2mm x 25.4mm x 1.6mm made up of Rogers RT/Duroid 5880 having dielectric constant $\varepsilon_r = 2.2$ and a thickness of 1.6mm. Each unit cell (6mmx7.8mm) consists of symmetrically placed spiral inductors on both sides of the unit cell. The electrical size of the unit cell is $0.1182\lambda_0$ x $0.0645\lambda_0$ x $0.0132\lambda_0$

at 2.48 GHz (n=0 mode). Some of the main features of these spiral inductors being that, firstly, it increases the shunt LH inductance L_L because the length of these spiral inductors is directly proportional to the shunt LH inductance which in turn leads to bandwidth enhancement [12] and secondly, with increase in the length of the inductive stubs, the resonant frequency of ZOR's decreases [13]. Additionally, CRLH TL's has an inherent property to provide multi frequency multi-band resonances. The unit cells or the radiating patch is separated by a small gap of 0.2 mm. This gap provides the series LH capacitance C_L while the magnetic flux produced by the current flow along the radiating patch provides the parasitic series RH inductance L_R. Each unit cell is parallel connected to the two short ended spiral inductors having 5 turns. These spiral inductors of width 0.4mm introduce the LH inductance L_L. The gap between the spiral inductor strips is also equal to 0.4 mm. As the whole CRLH TL structure is excited by open circuiting (with a small coupling capacitance), shunt resonance ω_{sh} initiates, with energy storing taking place in the shunt elements.

When the structure is balanced then the two resonant frequencies ω_{sh} and ω_{se} are identical. Bottom ground is placed to provide an impedance matching of about 42 ohms. Figures 3(a) and 3(e) show the simulated reflection coefficients and VSWR of the proposed antenna respectively. It is observed that a reflection coefficient of -20.2014 dB at the zeroth mode (2.48 GHz) is obtained. Figure 3(a) shows the comparison of the simulated and measured reflection coefficients of the proposed design. A very good agreement between the measured and the simulated results are obtained. The measured reflection coefficient is slightly shifted from that of the simulated one which can be attributed to minor errors in the fabrication of vias or due to improper etching. Figure 3(b) shows the radiation patterns at E-plane (x-z plane) and H-plane (y-z plane) for different operational frequencies. In all these different frequencies, a dumb-bell shaped E-radiation patterns and very good omni-directional H-radiation patterns are obtained. Figure 3(c) shows the 2D gain patterns of the proposed antenna for different operational frequencies. Figures 3(d) shows the 3D gain at each operational frequency. Highest gain of 1.9515 dB is achieved at 3.54 GHz. The simulated radiation efficiency (%) and gain (dB) according to the operating band are presented in Fig. 3(d). In this proposed antenna, a bandwidth of 1.36% and radiation efficiency of 55.31% are achieved at zeroth order resonance of 2.48 GHz with a gain of 1.559 dB. The radiation efficiency is enhanced to approximately 83% at 3.54 GHz but drops to 7% at 1.01 GHz due to a high rise of conductivity loss. Figs. 5(a, b) and 6(a, b) show the measured radiation patterns at 2.528 GHz and 3.684 GHz respectively. Since, radiation pattern measurements were undertaken with the test antenna mounted onto an aluminum plate fixture which was aligned to a reference wideband horn antenna so there is a slight variation in the simulated and measured radiation patterns. The antenna is tested at Antenna Measurement Facility (AMF), Space Application Centre, ISRO Ahmedabad. Real time flight model testing was carried out in an anechoic chamber shown in Fig. 4. Table1 shows the performance characteristics of the proposed antenna with substrate, RT Duroid (ε_r=2.2), no. of unit cells = 2 and no. of resonating modes/bands = 3. All simulations were carried out using Ansoft HFSS using Driven set up. No. of passes used is 6 and convergence ratio (Delta S): 0.02 is the maximum change in the magnitude of the S-parameters between two consecutive adaptive passes. The antenna is excited with wave port excitations. Measurements were undertaken with Agilent E8363B Network Analyzer.

A. Antenna Geometry

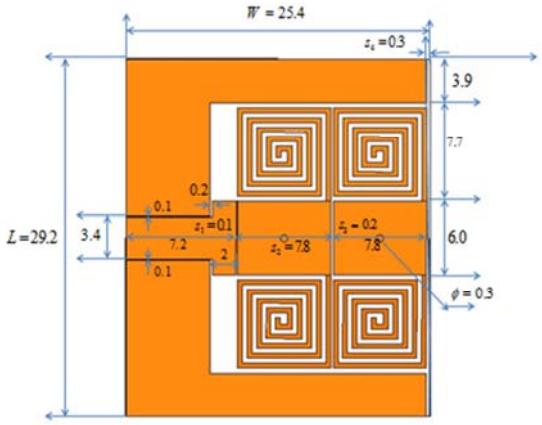

Fig. 2(a). Geometrical model of the proposed triband antenna (Top Patch with two unit cells).

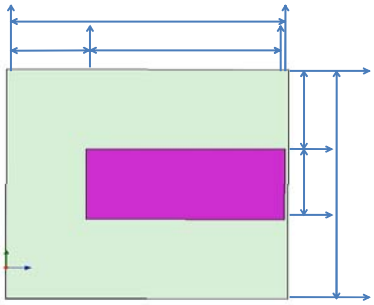

Fig. 2(b). Geometrical model of the proposed triband, pentamode antenna (with two unit cells).

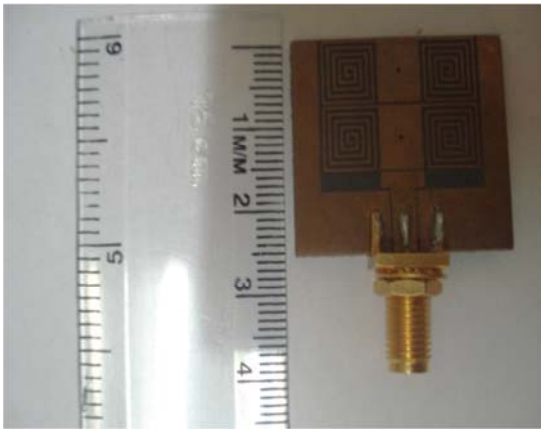

Fig. 2(c). Fabricated prototype of the proposed antenna.

V. SIMULATION RESULTS

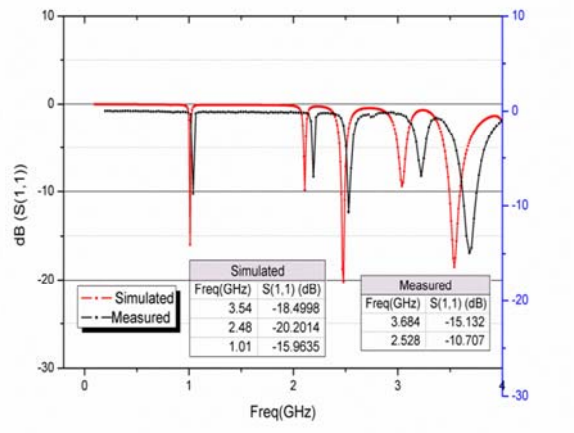

Fig. 3(a). Comparison of simulated and measured reflection coefficients of the proposed antenna.

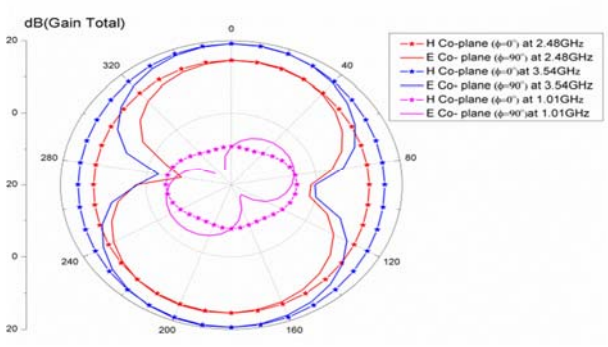

Fig. 3(b). Radiation Patterns $Eplane(\phi = 90^{\circ})$ and $Hplane$ $(\phi = 0^{\circ})$ at different operational frequencies.

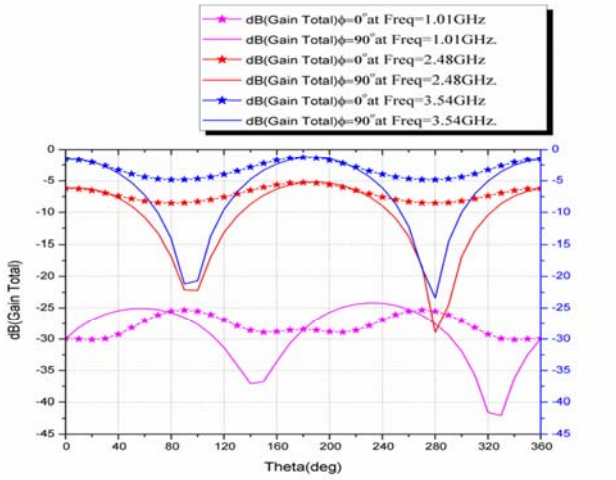

Fig. 3(c). Gain Patterns at different operational frequencies.

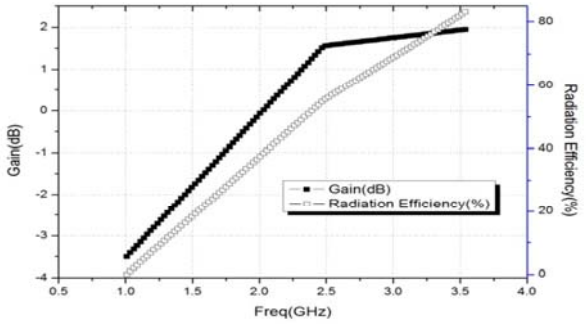

Fig. 3(d). Simulated radiation efficiency and gain for the proposed structure.

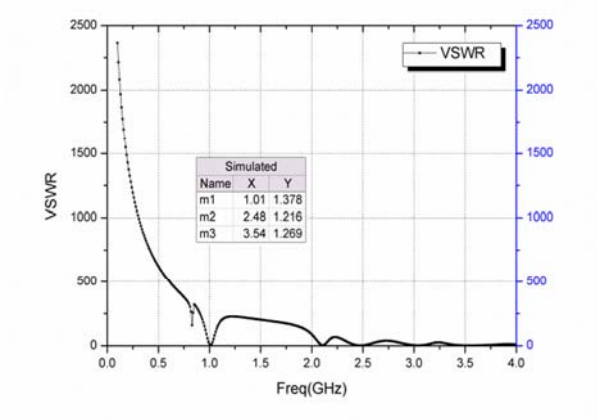

Fig. 3(e). V.S.W.R. for the proposed structure.

VI. ANTENNA/FEED MEASURED PERFORMANCE

A. INTRODUCTION: ANECHOIC CHAMBER

SPACE APPLICATIONS CENTRE (SAC), ISRO, Ahmedabad, has an Anechoic Chamber for characterizing feed system and electrically small antennas radiation pattern measurement at very low power levels in far field configuration. The Anechoic chamber is having size of 13m x 8m x 8m (L x W x H) respectively, quiet Zone of 1m³ and has been designed for the frequency range of 1.0 GHz to 40 GHz and currently it can cater the frequency range up to 60 GHz.

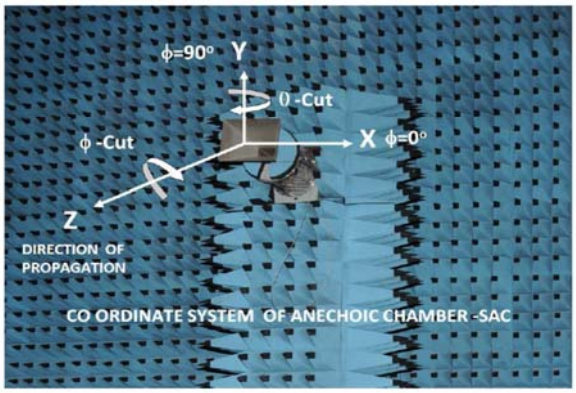

Fig. 4. - Photograph showing axis definition in the Anechoic Chamber. For clarity, a co-ordinate system has been superimposed on the picture.

B. MEASURED RADIATION CUTS:

The radiation pattern cuts H-plane and E-plane for given patch antennas are shown below.

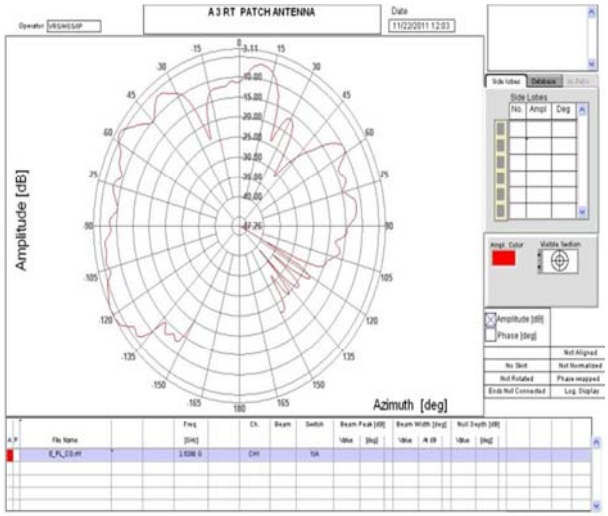

Fig. 5(a). Measured Radiation Pattern E co-plane at 2 .528 GHz.

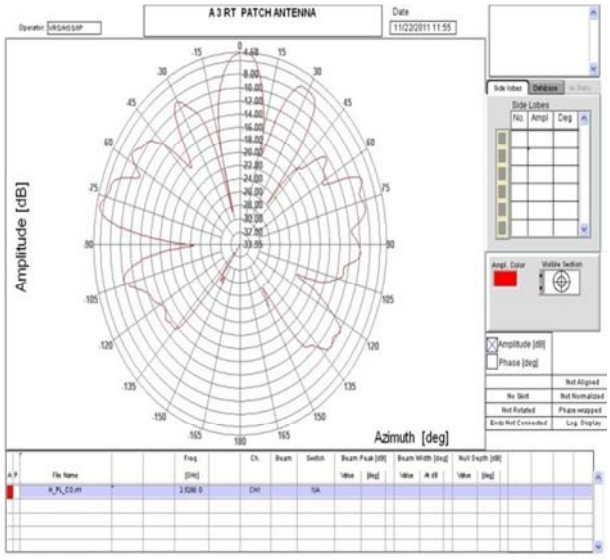

Fig. 5(b). Measured Radiation Pattern H co-plane at 2 .528 GHz.

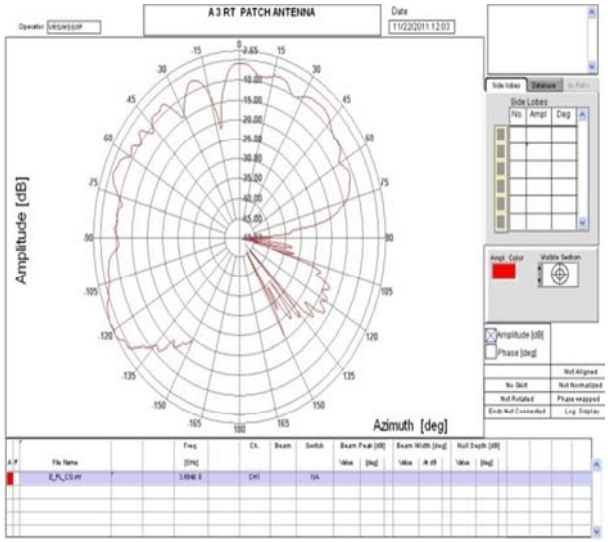

Fig. 6(a). Measured Radiation Pattern E co-plane at 3.684 GHz.

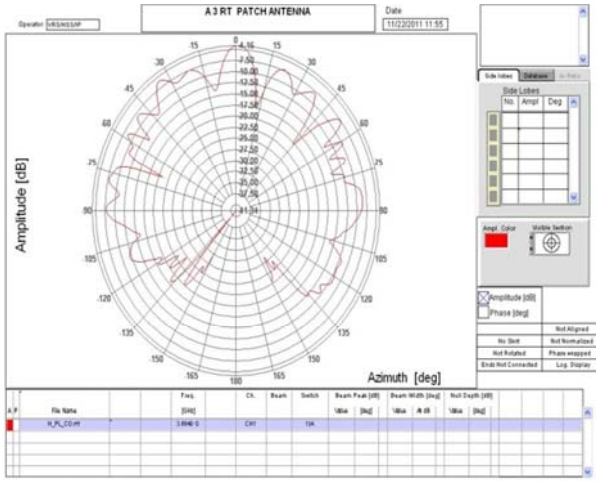

Fig. 6(b). Measured Radiation Pattern H co-plane at 3.684 GHz.

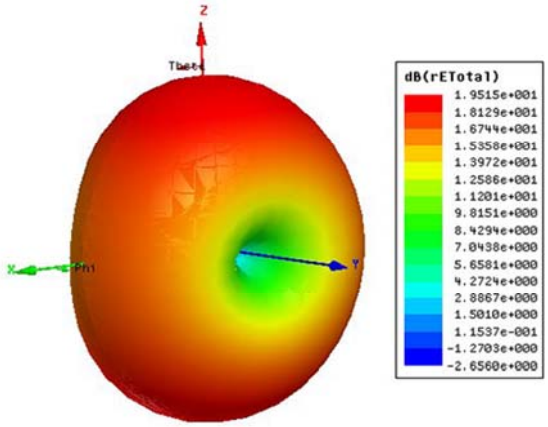

Fig. 7(a). Gain of the antenna at n=+2 mode (freq= 3.54GHz).

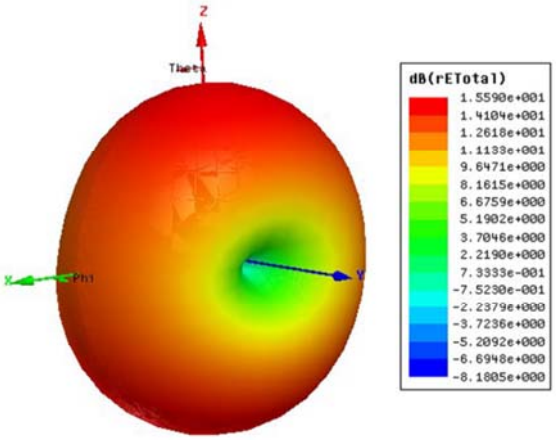

Fig. 7(b). Gain of the antenna at n=0 mode (freq= 2.48GHz).

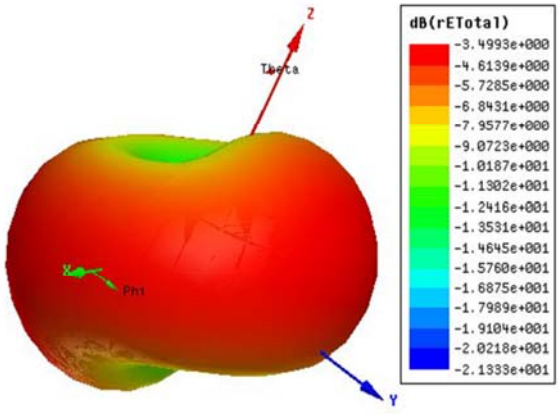

Fig. 7(c). Gain of the antenna at n= -2 mode (freq= 1.01 GHz).

Table 1: Performance Characteristics of the proposed metamaterial antenna.

Resonant Freq (GHz)	Return Loss (dB)	Gain (dB)	Band-width (%)	Radiation Efficiency
f_{+2}=3.54	-18.4998	1.9515		0.8252
f_{+1}=3.04	-9.4013	1.5256		0.51737
f_0=2.48	-20.2014	1.5590	1.36	0.5531
f_{-1}=2.11	-9.8419	6.2652		0.087649
f_{-2}=1.01	-15.9635	-3.4993		0.069301

VII. CONCLUSION

A compact, triband metamaterial antenna with novel spiral inductors is proposed. The LH shunt inductance contributed by the spiral inductors leads to bandwidth of about 1.36% with an impedance matching of 42Ω. A dumb-bell shaped E plane radiation pattern and omni-directional based H plane radiation pattern are obtained along with triband characteristics making it most suitable for point to point wireless applications.

ACKNOWLEDGMENT

The authors would like to thank Dr. Rajeev Jyoti, Group Director, Dr. H.C. Sanandiya, Head AMF and antenna system group members of Space Application Centre, ISRO, Ahmedabad for carrying out measurement facilities in their laboratory towards furtherance of this research work. Thanks are also due to Prof. D.R. Poddar, Jadavpur University, Kolkata, India for providing simulation facilities at his laboratory.

REFERENCES

[1] Y. Ge, K. Esselle and T. Bird, "Compact Triple-arm Multiband Monopole Antenna," in *Proc. IEEE Int. Workshop on: Antenna Technology Small Antennas and Novel Metamaterials,* pp. 172-175, Mar. 2006.

[2] N. Herscovici, Z. Sipus and P. S. Kildal, "The Cylindrical Omnidirectional Patch Antenna," *IEEE Trans. Antennas Propagat.*, vol. 49, no.12, pp.1746-1753, 2001.

[3] T. H. Lam, M. J. Milicic Jr and D. M. Pritchett, "Dipole Antenna having Co-axial Radiators and Feed," U. S. Patent 5 387 919, Feb. 7, 1995.

[4] T. E. Koscica and B. J. Liban, "Simplified Stacked Dipole Antenna," U. S. Patent 6 014 112, Jan. 11, 2000.

[5] D. Braaten, R. P. Scheeler, M. Reich, R. M. Nelson, C. Bauer-Reich, J. Glower, G. J. Owen, "Compact Metamaterial-Based UHF RFID Antennas: Deformed Omega and Split-Ring Resonator Structures," *Applied Computational Electromagnetics Society (ACES) Journal*, vol. 25, no. 6, pp. 530-542, June 2010.

[6] J. C. Liu, W. Shao, B. Z. Wang, "A Dual-Band Metamaterial Design using Double SRR Structures," *Applied Computational Electromagnetics Society (ACES) Journal*, vol. 26, no. 6, pp. 459-463, June 2011.

[7] M. Tang, S. Xiao, D. Wang, J. Xiong, K. Chen, B. Wang, "Negative Index of Reflection in Planar Metamaterial Composed of Single Split-Ring Resonators," *Applied Computational Electromagnetics Society (ACES) Journal*, vol. 26, no. 3, pp. 250-258, March 2011.

[8] C. Caloz and T. Itoh, "Electromagnetic Metamaterials, Transmission Line Theory and Microwave applications," Wiley and IEEE Press, Wiley and IEEE Press, Hoboken-Piscataway, New Jersey, 2005.

[9] A. Lai, C. Caloz, and T. Itoh, "Composite Right/Left-handed Transmission Line Metamaterials," *IEEE Microwave Mag.*, vol. 5, no. 3, pp. 34-50, Sep. 2004.

[10] D. Verba, M. Polivka, "Improvement of the Radiation Efficiency of the Metamaterial Zero-order Resonator Antenna", *Radio Engineering*, vol. 18, pp. 1-8, April 2009.

[11] D. Sievenpiper, L. Zhang, F. J. Broas, N. G. Alexopulos, and E. Yablonovitch, "High-impedance Electromagnetic Surfaces with a Forbidden Frequency Band," *IEEE Trans. Microwave Theory Tech.*, vol. 47, no. 11, pp. 2059-2074, Nov. 1999.

[12] A. Lai, K. M. K. H. Leong, and T. Itoh, "Infinite Wavelength Resonant Antennas with Monopolar Radiation Pattern based on Periodic Structures", I*EEE Trans. Antennas and Propagation*, vol. 55, no. 3, pp. 868-876, March 2007.

[13] J. Lee, K. M. K. H. Leong, and T. Itoh, "Compact Dual-band Antenna using an Anisotropic Metamaterial," *Proc. 36th Eur. Microw. Conf.*, Manchester, U. K., pp. 1044-1047, Sept. 2006.

[14] J. Lu, H. Chin, "Planar Compact U-Shaped Patch Antenna with High-Gain Operation for Wi-

Fi/WiMAX Application," *Applied Computational Electromagnetics Society (ACES) Journal*, vol. 26, no. 1, pp. 82-86, January 2011.

[15] Rennings, T. Liebig, C. Caloz, P. Waldow, "MIM CRLH Series Mode Zeroth Order Resonant Antenna (ZORA) Implemented in LTCC Technology," *Asia Pacific Microwave Conference 2007*, Bangkok, pp.191-194, Dec. 2007.

[16] Taehee Jang and Sungjoon Lim, "A Compact Zeroth Order Resonant Antenna on Vialess CPW Single Layer", *ETRI Journal*, vol. 32, no. 3, June 2010.

Sheeja K. L. received the M. Tech degree in Electronics Systems and Communication from National Institute of Technology, Rourkela, Odisha, India in 2009. She is currently pursuing her PhD degree from the same institute. Her research interest includes the design and analysis of resonant antennas using metamaterial transmission lines and synthesis of electrically small antennas.

Prasanna Kumar Sahu received the B.Sc.(Engg.) degree from UCE Burla, Sambalpur University in the year 1986, M Sc. (Engg.) from REC, Rourkela, Sambalpur University in the year 1991 and PhD. (Engg.) from Jadavpur University in the year 2007 respectively. He is presently working as an Associate Professor in the Department of Electrical Engineering, National Institute of Technology, Rourkela, India. His current research interest includes Nanoelectronics, Metamaterials and Dielectric Resonator Antennas. Dr. Sahu is a Member of IEEE (USA), Life Member of Institute of Engineers, India.

Santanu Kumar Behera received the BSc.(Engg) degree from UCE Burla, Sambalpur University in the year 1990, ME and PhD(Engg) from Jadavpur University in the year 2001 and 2008 respectively. He is presently working as an Associate Professor in the Department of Electronics and communication Engineering, National Institute of Technology Rourkela, India. His current research interests include Planar Antenna; Dielectric Resonator Antenna and Metamaterials. Dr. Behera is a Life Member of IETE (India), Computer Society of India, Society of EMC Engineers (India), ISTE (India) and Member of IEEE (USA).

Nabil Dakhli recieved the Master degree in electrical engineering from Tunis University of Science, Tunisia, in 2005, and is currently working toward the Ph.D. degree at the High Institute of Telecommunication Engineering SUP'COM, Ariana, Tunisia. His research interests antennas, periodic structures, and metamaterials.

2012 INSTITUTIONAL MEMBERS

DTIC-OCP LIBRARY
8725 John J. Kingman Rd, Ste 0944
Fort Belvoir, VA 22060-6218

AUSTRALIAN DEFENCE LIBRARY
Northcott Drive
Canberra, A.C.T. 2600 Australia

BEIJING BOOK CO, INC
701 E Linden Avenue
Linden, NJ 07036-2495

DARTMOUTH COLLEGE
6025 Baker/Berry Library
Hanover, NH 03755-3560

DSTO EDINBURGH
AU/33851-AP, PO Box 830470
Birmingham, AL 35283

SIMEON J. EARL – BAE SYSTEMS
W432A, Warton Aerodome
Preston, Lancs., UK PR4 1AX

ENGINEERING INFORMATION, INC
PO Box 543
Amsterdam, Netherlands 1000 Am

ETSE TELECOMUNICACION
Biblioteca, Campus Lagoas
Vigo, 36200 Spain

GA INSTITUTE OF TECHNOLOGY
EBS-Lib Mail code 0900
74 Cherry Street
Atlanta, GA 30332

TIMOTHY HOLZHEIMER
Raytheon
PO Box 1044
Rockwall, TX 75087

HRL LABS, RESEARCH LIBRARY
3011 Malibu Canyon
Malibu, CA 90265

IEE INSPEC
Michael Faraday House
6 Hills Way
Stevenage, Herts UK SG1 2AY

INSTITUTE FOR SCIENTIFIC INFO.
Publication Processing Dept.
3501 Market St.
Philadelphia, PA 19104-3302

LIBRARY – DRDC OTTAWA
3701 Carling Avenue
Ottawa, Ontario, Canada K1A OZ4

LIBRARY of CONGRESS
Reg. Of Copyrights
Attn: 407 Deposits
Washington DC, 20559

LINDA HALL LIBRARY
5109 Cherry Street
Kansas City, MO 64110-2498

MISSOURI S&T
400 W 14th Street
Rolla, MO 56409

MIT LINCOLN LABORATORY
Periodicals Library
244 Wood Street
Lexington, MA 02420

NATIONAL CHI NAN UNIVERSITY
Lily Journal & Book Co, Ltd
20920 Glenbrook Drive
Walnut, CA 91789-3809

JOHN NORGARD
UCCS
20340 Pine Shadow Drive
Colorado Springs, CO 80908

OSAMA MOHAMMED
Florida International University
10555 W Flagler Street
Miami, FL 33174

NAVAL POSTGRADUATE SCHOOL
Attn:J. Rozdal/411 Dyer Rd./ Rm 111
Monterey, CA 93943-5101

NDL KAGAKU
C/0 KWE-ACCESS
PO Box 300613 (JFK A/P)
Jamaica, NY 11430-0613

OVIEDO LIBRARY
PO BOX 830679
Birmingham, AL 35283

DAVID PAULSEN
E3Compliance
1523 North Joe Wilson Road
Cedr Hill, TX 75104-1437

PENN STATE UNIVERSITY
126 Paterno Library
University Park, PA 16802-1808

DAVID J. PINION
1122 E Pike Street #1217
SEATTLE, WA 98122

KATHERINE SIAKAVARA
Gymnasiou 8
Thessaloniki, Greece 55236

SWETS INFORMATION SERVICES
160 Ninth Avenue, Suite A
Runnemede, NJ 08078

YUTAKA TANGE
Maizuru Natl College of Technology
234 Shiroya
Maizuru, Kyoto, Japan 625-8511

TIB & UNIV. BIB. HANNOVER
DE/5100/G1/0001
Welfengarten 1B
Hannover, Germany 30167

UEKAE
PO Box 830470
Birmingham, AL 35283

UNIV OF CENTRAL FLORIDA
4000 Central Florida Boulevard
Orlando, FL 32816-8005

UNIVERSITY OF COLORADO
1720 Pleasant Street, 184 UCB
Boulder, CO 80309-0184

UNIVERSITY OF KANSAS – WATSON
1425 Jayhawk Blvd 210S
Lawrence, KS 66045-7594

UNIVERSITY OF MISSISSIPPI
JD Williams Library
University, MS 38677-1848

UNIVERSITY LIBRARY/HKUST
Clear Water Bay Road
Kowloon, Honk Kong

CHUAN CHENG WANG
8F, No. 31, Lane 546
MingCheng 2nd Road, Zuoying Dist
Kaoshiung City, Taiwan 813

THOMAS WEILAND
TU Darmstadt
Schlossgartenstrasse 8
Darmstadt, Hessen, Germany 64289

STEVEN WEISS
US Army Research Lab
2800 Powder Mill Road
Adelphi, MD 20783

YOSHIHIDE YAMADA
NATIONAL DEFENSE ACADEMY
1-10-20 Hashirimizu
Yokosuka, Kanagawa,
Japan 239-8686

APPLIED COMPUTATIONAL ELECTROMAGNETICS SOCIETY JOURNAL
http://aces.ee.olemiss.edu

INFORMATION FOR AUTHORS

PUBLICATION CRITERIA

Each paper is required to manifest some relation to applied computational electromagnetics. **Papers may address general issues in applied computational electromagnetics, or they may focus on specific applications, techniques, codes, or computational issues.** While the following list is not exhaustive, each paper will generally relate to at least one of these areas:

1. **Code validation.** This is done using internal checks or experimental, analytical or other computational data. Measured data of potential utility to code validation efforts will also be considered for publication.

2. **Code performance analysis.** This usually involves identification of numerical accuracy or other limitations, solution convergence, numerical and physical modeling error, and parameter tradeoffs. However, it is also permissible to address issues such as ease-of-use, set-up time, run time, special outputs, or other special features.

3. **Computational studies of basic physics.** This involves using a code, algorithm, or computational technique to simulate reality in such a way that better, or new physical insight or understanding, is achieved.

4. **New computational techniques** or new applications for existing computational techniques or codes.

5. **"Tricks of the trade"** in selecting and applying codes and techniques.

6. **New codes, algorithms, code enhancement, and code fixes.** This category is self-explanatory, but includes significant changes to existing codes, such as applicability extensions, algorithm optimization, problem correction, limitation removal, or other performance improvement. **Note: Code (or algorithm) capability descriptions are not acceptable, unless they contain sufficient technical material to justify consideration.**

7. **Code input/output issues.** This normally involves innovations in input (such as input geometry standardization, automatic mesh generation, or computer-aided design) or in output (whether it be tabular, graphical, statistical, Fourier-transformed, or otherwise signal-processed). Material dealing with input/output database management, output interpretation, or other input/output issues will also be considered for publication.

8. **Computer hardware issues.** This is the category for analysis of hardware capabilities and limitations of various types of electromagnetics computational requirements. Vector and parallel computational techniques and implementation are of particular interest.

Applications of interest include, but are not limited to, antennas (and their electromagnetic environments), networks, static fields, radar cross section, inverse scattering, shielding, radiation hazards, biological effects, biomedical applications, electromagnetic pulse (EMP), electromagnetic interference (EMI), electromagnetic compatibility (EMC), power transmission, charge transport, dielectric, magnetic and nonlinear materials, microwave components, MEMS, RFID, and MMIC technologies, remote sensing and geometrical and physical optics, radar and communications systems, sensors, fiber optics, plasmas, particle accelerators, generators and motors, electromagnetic wave propagation, non-destructive evaluation, eddy currents, and inverse scattering.

Techniques of interest include but not limited to frequency-domain and time-domain techniques, integral equation and differential equation techniques, diffraction theories, physical and geometrical optics, method of moments, finite differences and finite element techniques, transmission line method, modal expansions, perturbation methods, and hybrid methods.

Where possible and appropriate, authors are required to provide statements of quantitative accuracy for measured and/or computed data. This issue is discussed in "Accuracy & Publication: Requiring, quantitative accuracy statements to accompany data," by E. K. Miller, *ACES Newsletter*, Vol. 9, No. 3, pp. 23-29, 1994, ISBN 1056-9170.

SUBMITTAL PROCEDURE

All submissions should be uploaded to ACES server through ACES web site (http://aces.ee.olemiss.edu) by using the upload button, journal section. Only pdf files are accepted for submission. The file size should not be larger than 5MB, otherwise permission from the Editor-in-Chief should be obtained first. Automated acknowledgment of the electronic submission, after the upload process is successfully completed, will be sent to the corresponding author only. It is the responsibility of the corresponding author to keep the remaining authors, if applicable, informed. Email submission is not accepted and will not be processed.

EDITORIAL REVIEW

In order to ensure an appropriate level of quality control, papers are peer reviewed. They are reviewed both for technical correctness and for adherence to the listed guidelines regarding information content and format.

PAPER FORMAT

Only camera-ready electronic files are accepted for publication. The term **"camera-ready" means that the material is neat, legible, reproducible, and in accordance with the final version format listed below.**

The following requirements are in effect for the final version of an ACES Journal paper:

1. The paper title should not be placed on a separate page.

The title, author(s), abstract, and (space permitting) beginning of the paper itself should all be on the first page. The title, author(s), and author affiliations should be centered (center-justified) on the first page. The title should be of font size 16 and bolded, the author names should be of font size 12 and bolded, and the author affiliation should be of font size 12 (regular font, neither italic nor bolded).

2. An abstract is required. The abstract should be a brief summary of the work described in the paper. It should state the computer codes, computational techniques, and applications discussed in the paper (as applicable) and should otherwise be usable by technical abstracting and indexing services. The word "Abstract" has to be placed at the left margin of the paper, and should be bolded and italic. It also should be followed by a hyphen (—) with the main text of the abstract starting on the same line.

3. All section titles have to be centered and all the title letters should be written in caps. The section titles need to be numbered using roman numbering (I. II. ….)

4. Either British English or American English spellings may be used, provided that each word is spelled consistently throughout the paper.

5. Internal consistency of references format should be maintained. As a guideline for authors, we recommend that references be given using numerical numbering in the body of the paper (with numerical listing of all references at the end of the paper). The first letter of the authors' first name should be listed followed by a period, which in turn, followed by the authors' complete last name. Use a coma (,) to separate between the authors' names. Titles of papers or articles should be in quotation marks (" "), followed by the title of journal, which should be in italic font. The journal volume (vol.), issue number (no.), page numbering (pp.), month and year of publication should come after the journal title in the sequence listed here.

6. Internal consistency shall also be maintained for other elements of style, such as equation numbering. Equation numbers should be placed in parentheses at the right column margin. All symbols in any equation have to be defined before the equation appears or right immediately following the equation.

7. The use of SI units is strongly encouraged. English units may be used as secondary units (in parentheses).

8. Figures and tables should be formatted appropriately (centered within the column, side-by-side, etc.) on the page such that the presented data appears close to and after it is being referenced in the text. When including figures and tables, all care should be taken so that they will appear appropriately when printed in black and white. For better visibility of paper on computer screen, it is good to make color figures with different line styles for figures with multiple curves. Colors should also be tested to insure their ability to be distinguished after black and white printing. Avoid the use of large symbols with curves in a figure. It is always better to use different line styles such as solid, dotted, dashed, etc.

9. A figure caption should be located directly beneath the corresponding figure, and should be fully justified.

10. The intent and meaning of all text must be clear. For authors who are not masters of the English language, the ACES Editorial Staff will provide assistance with grammar (subject to clarity of intent and meaning). However, this may delay the scheduled publication date.

11. Unused space should be minimized. Sections and subsections should not normally begin on a new page.

ACES reserves the right to edit any uploaded material, however, this is not generally done. It is the author(s) responsibility to provide acceptable camera-ready files in pdf and MSWord formats. Incompatible or incomplete files will not be processed for publication, and authors will be requested to re-upload a revised acceptable version.

COPYRIGHTS AND RELEASES

Each primary author must execute the online copyright form and obtain a release from his/her organization vesting the copyright with ACES. Both the author(s) and affiliated organization(s) are allowed to use the copyrighted material freely for their own private purposes.

Permission is granted to quote short passages and reproduce figures and tables from and ACES Journal issue provided the source is cited. Copies of ACES Journal articles may be made in accordance with usage permitted by Sections 107 or 108 of the U.S. Copyright Law. This consent does not extend to other kinds of copying, such as for general distribution, for advertising or promotional purposes, for creating new collective works, or for resale. The reproduction of multiple copies and the use of articles or extracts for commercial purposes require the consent of the author and specific permission from ACES. Institutional members are allowed to copy any ACES Journal issue for their internal distribution only.

PUBLICATION CHARGES

All authors are allowed for 8 printed pages per paper without charge. Mandatory page charges of $75 a page apply to all pages in excess of 8 printed pages. Authors are entitled to one, free of charge, copy of the printed journal issue in which their paper was published. Additional reprints are available for $ 50. Requests for additional re-prints should be submitted to the managing editor or ACES Secretary.

Corresponding author is required to complete the online form for the over page charge payment right after the initial acceptance of the paper is conveyed to the corresponding author by email.

ACES Journal is abstracted in INSPEC, in Engineering Index, DTIC, Science Citation Index Expanded, the Research Alert, and to Current Contents/Engineering, Computing & Technology.